TÉCNICO
UNIVERSIDADE
DE LISBOA

UNIVERSIDADE DE LISBOA
INSTITUTO SUPERIOR TÉCNICO

Static Optimization and Dynamic Modeling of Microalgae Production in Photobioreactors

Tiago Miguel Gamito Taborda

Supervisor: Doctor Francisco Manuel da Silva Lemos

Co-Supervisors: Doctor José Carlos Magalhães Pires

Doctor Sara Martins Badenes

Thesis approved in public session to obtain the PhD Degree in
Refining, Petrochemical, and Chemical Engineering

Jury final classification:
Pass with Distinction

2026

UNIVERSIDADE DE LISBOA
INSTITUTO SUPERIOR TÉCNICO

Static Optimization and Dynamic Modeling of Microalgae Production in Photobioreactors

Tiago Miguel Gamito Taborda

Supervisor: Doctor Francisco Manuel da Silva Lemos

Co-Supervisors: Doctor José Carlos Magalhães Pires

Doctor Sara Martins Badenes

Thesis approved in public session to obtain the PhD Degree in

Refining, Petrochemical, and Chemical Engineering

Jury final classification:

Pass with Distinction

Jury

Chairperson: Doctor Henrique Aníbal Santos de Matos, Instituto Superior Técnico, Universidade de Lisboa

Members of Committee:

Doctor José António Couto Teixeira, Universidade do Minho

Doctor João Paulo Serejo Goulão Crespo, Faculdade de Ciências e Tecnologia, Universidade Nova de Lisboa

Doctor Duarte Miguel de França Teixeira dos Prazeres, Instituto Superior Técnico, Universidade de Lisboa

Doctor Henrique Aníbal Santos de Matos, Instituto Superior Técnico, Universidade de Lisboa

Doctor Alberto José Delgado dos Reis, Laboratório Nacional de Energia e Geologia (LNEG)

Doctor Sara Martins Badenes, Centro de Inovação em Microalgas, A4F - Algae for Future

Funding Institutions

FCT: Fundação para a Ciência e Tecnologia

CERENA Centro de Recursos Naturais e Ambiente
LEPABE Laboratory for Process Engineering, Environment, Biotechnology, and Energy
AliCE Associated Laboratory for Innovation in Chemical Engineering

2026

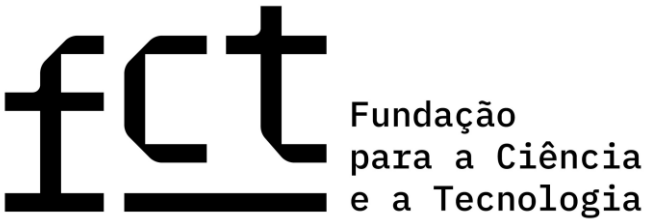

This work was financially supported by Fundação para a Ciência e a Tecnologia with the Ph.D. fellowship SFRH/BD/151226/2021, by ALiCE (project LA/P/0045/2020), by CERENA (project UIDB/04028/2025 and UIDP/04028/2025), and LEPABE (projects UIDB/00511/2020 -and UIDP/00511/2020), funded by national funds through FCT/MCTES (PIDDAC)

Abstract

Microalgae and other photosynthetic microorganisms are increasingly recognized for their industrial potential, particularly in carbon capture, biofuel production, and high-added-value bioproducts. Their cultivation in closed outdoor photobioreactors presents opportunities for scalable production but also introduces complex challenges in modeling and control. This Ph.D. thesis addresses key gaps in modeling microalgae growth under real-world conditions, combining experimental data analysis with methodological innovation in three chapters.

First, a comprehensive review of state-of-the-art modeling strategies is presented, with a focus on closed outdoor photobioreactors. This analysis categorizes and evaluates models that describe the influence of environmental factors such as light, temperature, nutrients, and carbon sources on microalgae growth. Particular emphasis is placed on light intensity modeling, with 14 distinct models drawn from 32 papers examined in depth to elucidate their assumptions and parameter significance.

Building on this foundation, the second study proposes and evaluates a set of empirical growth models for *Nannochloropsis* sp. cultivated in outdoor tubular reactors. Four model types were tested—Monod-like, Haldane-like, Exponential, and Monod with a Droop-based model for nutrients—using data from ten assays. The Haldane-like model demonstrated the best performance, achieving a root mean squared error (RMSE) of 0.296 kg m^{-3}, when compared to 0.309, 0.302, and 0.413 kg m^{-3} for the Monod, Exponential, and Droop models, respectively. This study underscores the importance of tailoring model structure to reactor scale and species-specific dynamics and establishes a framework for future model development.

Finally, a novel model for predicting the distribution of solar irradiation inside tubular photobioreactors is introduced. Capable of simulating light profiles for any geographic location and orientation, this model enhances the prediction of spatial growth rates within the reactor and supports design and operational decisions. Validation using a custom-built light-sensing system confirmed the model's accuracy, achieving high Pearson correlation coefficients (96.6% and 86.0% for two different runs) with measured data, and outperforming existing light attenuation models.

Together, these contributions advance the modeling and optimization of outdoor photobioreactors, providing tools and insights essential for cultivation under variable environmental conditions.

Keywords: closed photobioreactors; microalgae; model comparison; pilot-scale reactors; reactor optimization

Resumo

As microalgas e outros microrganismos fotossintéticos são cada vez mais reconhecidos pelo seu potencial industrial, nomeadamente na captura de carbono, produção de biocombustíveis e bioprodutos de elevado valor acrescentado. A sua cultura em fotobiorreatores exteriores fechados apresenta oportunidades para uma produção em grande escala, mas também introduz desafios complexos ao nível da modelação e controlo. Esta tese de doutoramento aborda lacunas importantes na modelação do crescimento de microalgas em condições reais, combinando a análise de dados experimentais com inovação metodológica ao longo de três capítulos.

No primeiro capítulo, é apresentada uma revisão abrangente das estratégias de modelação mais avançadas, com foco em fotobiorreatores exteriores fechados. Esta análise categoriza e avalia modelos que descrevem a influência de fatores ambientais como luz, temperatura, nutrientes e fontes de carbono no crescimento das microalgas. Dá-se especial destaque à modelação da intensidade luminosa, com 14 modelos distintos, extraídos de 32 artigos, analisados em profundidade para esclarecer as suas premissas e a importância dos seus parâmetros.

Com base nesta análise, o segundo capítulo propõe e avalia um conjunto de modelos empíricos de crescimento para a espécie *Nannochloropsis sp.*, cultivada em fotobiorreatores tubulares exteriores. Quatro modelos foram testados—Monod, Haldane, Exponencial, e Monod com um modelo baseado no trabalho de Droop para os nutrientes—utilizando dados de dez ensaios. O modelo de Haldane apresentou o melhor desempenho, com um erro quadrático médio (RMSE) de 0,296 kg m^{-3}, comparado com 0,309, 0,302 e 0,413 kg^{1} m^{-3} para os modelos de Monod, Exponencial e Droop, respetivamente. Este estudo destaca a importância de adaptar a estrutura do modelo ao reator e à dinâmica específica da espécie, estabelecendo um quadro para o desenvolvimento futuro de modelos.

Por fim, é introduzido um modelo inovador para a previsão da distribuição da radiação solar no interior de fotobiorreatores tubulares. Capaz de simular perfis de luz para qualquer localização geográfica e orientação do reator, este modelo melhora a previsão das taxas de crescimento espacial no interior do reator e apoia decisões de

conceção e operação. A validação, realizada com um sistema customizado de deteção de luz, confirmou a precisão do modelo, com elevados coeficientes de correlação de Pearson (96,6% e 86,0% em dois ensaios distintos) em comparação com os dados medidos, superando os modelos existentes de atenuação da luz.

Em conjunto, estas contribuições representam avanços na modelação e optimização de fotobiorreatores exteriores, fornecendo ferramentas e conhecimentos essenciais para a cultura sob condições ambientais variáveis.

Palavras-chave: fotobiorreatores fechados; microalgas; comparação de modelos; reatores à escala piloto; optimização de reatores

Acknowledgements

To A4F and all its collaborators, I extend my gratitude for proposing this PhD topic, for their support in providing the necessary data used in this work, and for helping with the experimental work carried out.

To my PhD supervisors, who were always tireless when discussing and giving feedback on this work and extremely understanding during the worst periods of my chronic health condition.

To my father, who helped set up the light detection sensors, and was always available to brainstorm solutions to my work whenever I got stuck.

To the rest of my family, my mother, my grandpa, my brother, and my sister-in-law, who supported me throughout this journey despite my lackluster attempts at explaining my work.

To my late grandma, who passed away during the course of this thesis, and was always concerned about my health throughout.

To Nagaru Tanigawa, for have written my favorite story and changing my outlook on life in the process.

Contents

List of Figures

List of Tables

Notation

B	ratio of diffuse horizontal radiation over global horizontal radiation	
E_a	mass absorption coefficient	$m^2\ kg^{-1}$
I_0	incident radiation	$W\ m^{-2}$
I_{av}	average irradiation over an entire reactor cross-section	$W\ m^{-2}$
I_{av}	average irradiation over an entire reactor cross-section	$W\ m^{-2}$
I_{cell}	radiation effectively captured by an individual cell	$W\ m^{-2}$
I_{opt}	irradiance that maximizes growth rate in a light-dependent growth equation with inhibition	$W\ m^{-2}$
I_z	local irradiation on a point inside the reactor after attenuation over the path length z	$W\ m^{-2}$
K_I	inhibition constant for a light-dependent growth equation with inhibition	$W\ m^{-2}$
K_S	half-saturation constant for a Monod-like equation (rectangular hyperbolic) applied to light	$W\ m^{-2}$
K_{sub}	half-saturation constant for a Monod equation applied to substrates	$kg\ m^{-3}$
K_t	clear sky index, ratio between the global horizontal irradiation and the extraterrestrial radiation (radiation in the absence of atmosphere)	adi.
PAR	photosynthetic active radiation with a wavelength of 400–700nm	
P_{ang}	angle of the polar coordinates of a point P inside the reactor cross-section	degrees or rad
P_{rad}	radius of the polar coordinates of a point P inside the reactor cross-section	m
R_0	fraction of incident radiation reflected by the reactor's surface as calculated using Fresnel's law	
R_c	reactor radius	m
RMSE	root mean squared error	$kg\ m^{-3}$
X	biomass concentration	$kg\ m^{-3}$

z	optical path length of the direct solar rays between the reactor's surface and a point inside the reactor	m
$\mathbf{z_{diff}}$	optical path length of the diffuse solar rays between the reactor's surface and a point inside the reactor. Does not correspond to a physical distance	m
α	Lambert-Beer-like constant, product of X and E_a	m^{-1}
β	penetration angle of the solar rays on the reactor tube	degrees or rad
β'	refraction angle of the solar rays after application of Snell's law	degrees or rad
δ	solar declination	degrees or rad
ζ	constant considering all reactor geometric factors affecting diffuse light	adi.
η	latitude	degrees or rad
θ	solar zenith	degrees or rad
λ	longitude	degrees or rad
$\mathbf{\mu_{global}}$	global growth rate after integration of μ_{local} over every point of the reactor cross-section	h^{-1}
$\mathbf{\mu_{local}}$	local growth rate, considering local irradiation	h^{-1}
$\mathbf{\mu_{max}}$	maximum growth rate	h^{-1}
ϕ	solar azimuth	degrees or rad

1 Introduction

1.1 Motivation

"Photosynthetic microalgae" is not a strict taxonomic term, but rather a loosely-defined and convenient term for a broad group of organisms that contain chlorophyll α, carry out oxygenic photosynthesis, and are not specialized land plants [1]. They can live in a variety of environments depending on the species: from freshwater to marine or even hyper-saline water, in a wide range of pH (from very acidic to very alkaline), and in a wide range of temperature values, including extreme temperatures. Microalgae are an interesting and promising source of several organic products, for example, livestock feed, high-quality vegetal oil (which can be used for biofuel production), as a potential source for food products, including nutraceuticals, cosmetic applications, and high-valued bioactive metabolites, which are usually unique to some particular species, such as pharmaceuticals, antibacterial, antifungal and anticancer compounds [2].

Microalgae have several advantages over other sources for these specific products or applications. They grow fast, reaching high areal productivity when compared to land-based plants. Microalgae also do not require arable land, meaning they do not compete with conventional crops [3]. They require less freshwater than typical crops and, in particular cases, can even be grown on wastewater. However, microalgae cultivations still require large quantities of water, especially in open systems; however, there have been recent advances in the recycling of cultivation wastewater [4], thus drastically reducing the freshwater footprint [5].

As photosynthetic species, microalgae also capture CO_2 and can be used for CO_2 abatement from polluting industries (such as cement production [6] and flue gases from the burning of fossil fuels [7] after an appropriate pre-treatment). Finally, they can grow in a wide range of conditions, depending on the particular species that is chosen [8].

Over the past few decades, microalgae production has been subject to intense research and numerous large-scale investments. These sometimes involve the potential production of biofuels, but mainly they are focused on niche products such as nutraceuticals and pharmaceuticals [2], since these are expected to be the most lucrative implementation of microalgae. However, the technical feasibility, economics, and environmental benefits of large-scale algal cultivation for lower-valued products, such as biofuels, are still subject to much research [9].

The modeling of microalgae cultivations is a complex discipline, involving the interdependence of base biological models, engineering considerations of reactor design, mathematics, optics, chemistry, and, especially when it comes to outdoor cultivations, the understanding of astronomy and meteorology. As a result of this interdependence, the ability to forecast the outcome of large-scale outdoor microalgae cultivations is a difficult process. This work is an attempt at simplifying this process to offer reliable methods for optimizing and monitoring operating photobioreactors.

1.2 Objectives and Outline

This Ph.D. thesis is divided into five chapters.

- **Chapter 1** contains this introduction, which explores the application of microalgae and the challenges of modeling microalgae photobioreactors;
- **Chapter 2** compiles the current state-of-the-art modeling approaches to outdoor microalgae photobioreactors, as well as organizing and categorizing the disparate models existing in the literature, exploring their mathematical similarities, to allow for a better understanding of the models used. The work in this chapter has been accepted for publication as *Modeling closed outdoor cultivation of photoautotrophic microalgae growth rate: a critical review* in Journal of Applied Phycology (2025);
- **Chapter 3** proposes a methodology for utilizing data from previous pilot-scale cultivations to predict the outcome of future cultivations, using pre-existing semi-empirical models in the literature. The work in this chapter was published as a scientific article with the title *Comparing Growth Models Dependent on Irradiation and Nutrient Consumption on Closed Outdoor Cultivations of Nannochloropsis sp.* in Bioengineering (2025);
- **Chapter 4** presents a simple, universal model for the light distribution on a tubular reactor that can be applied to any location on Earth and to any reactor orientation, the output of which is compared with experimental measurements taken with light sensors on operating reactors;
- Finally, in the **Conclusions**, the main results of the thesis are discussed, highlighting the potential applications of the methodologies presented.

2 State of the Art

2.1 Challenges of modeling an outdoor culture

Modeling outdoor microalgae cultivation presents several challenges not found when modeling indoor systems, even when considering a similar reactor geometry. Outdoor cultivation is made to capture the free and universal resource of sunlight (although many are supplemented with artificial lights) and is usually made on large, production-level scales, while indoor cultivations can resort to varying artificial light sources, such as LEDs and halogen lights. Furthermore, since the reactors are exposed to the outdoor environment, the day-night cycle can lead to significant variations in temperature inside the reactor, whereas temperature indoors can more easily be controlled. These differences can be very significant due to several factors, which are detailed in the following sub-sections.

2.1.1 Daily and Seasonal Variations

2.1.1.1 Sunlight Availability

The factor most likely to cause significant discrepancies between an indoor system and an outdoor system is the intrinsic variation of the intensity of the available sunlight due to environmental factors, such as daily and seasonal variations in intensity due to the Earth's rotation and variation in the local weather.

When compared to artificial light sources, the use of the sun as a lighting source presents several modeling challenges because neither its incidence angle nor its intensity is constant, as both vary throughout the day and the year and are also dependent on the geographical location of the reactor. Sunlight is also intermittent, which causes different photoperiods to occur depending on the location and time of year, especially in locations far from the Equator. It is well established that microalgae's metabolism significantly changes during dark periods [10, 11]. Thus, different cycles of day and night can cause the microalgae's growth rate, composition, and metabolites to differ depending on when and where the cultivation is performed.

More significantly, the local weather, like clouds or fog, also greatly affects the intensity of sunlight that reaches the reactor, which implies that, for a forecast of productivity to be successful, there is the need to incorporate accurate weather data from the reactor's immediate vicinity in the model, not only during the development and validation but also the use of weather models to predict how a certain reactor might evolve during its period of operation. Ideally, this data can be

acquired locally using a weather station close to the site of operation of the reactor, but alternatively, publicly available weather data can be used.

Fortunately, the study of the sun and sunlight has been of major importance to several areas of science throughout the centuries, leading to many rigorous mathematical models that can be used to predict the position of the sun in the sky over the day and throughout the year, and consequently, the angle of incidence of sunlight. Slegers et al. produced an extensive appendix describing how weather data can be used to transform solar irradiance into direct light hitting a flat panel reactor by calculating the solar incidence angle [12]. Furthermore, accurate weather data is obtained *in situ* by the entities operating experimental facilities and large-scale cultivations, allowing the weather effect to be considered when modeling sunlight. Finally, in case light data is not collected *in situ* or is otherwise unavailable, entities such as the Photovoltaic Geographical Information System [13] can provide approximations of the amount of sunlight impacting any location on Earth in the past, which can be used to make models to approximate the amount of sunlight received in that location in the future.

Holdmann et al. showed that for Stuttgart, Germany, when using a reactor with a planar configuration, it is more advantageous to cultivate microalgae in the summer because there is a lower photon flux density distributed over more hours of sunlight when compared with the spring/fall, where the photon flux density peaks at higher values, which causes photoinhibition [14].

2.1.1.2 Variation of Temperature, Dissolved Gases, and pH

The day-night cycle not only affects the light availability inside the reactor but also brings about variations in air temperature, with air temperatures usually soaring during the middle of the day and being significantly lower at night.

Two competing effects affect the heat exchange between closed reactors and the environment. On one hand, closed reactors are more shielded from heat losses at night than open reactors due to heat transfer having to occur indirectly via the reactor walls or air exchange. On the other hand, they have a higher volume-to-surface-area ratio, resulting in more heat losses to the environment.

During the night, the high heat capacity of the water composing most of the reactor's medium allows it to retain more heat overnight than air, and thus the temperature decrease inside the reactor medium is expected to be lower than the decrease in air temperature. However, except in

extreme scenarios like the medium freezing, culture death is not expected as most microalgae's lower lethal temperature is quite far from its optimal growth temperature [15].

A potentially more significant consequence of this temperature drop is the change in the solubility of gases in the medium. Gases such as carbon dioxide (CO_2) and oxygen (O_2) are more soluble the lower the temperature of the water; CO_2's solubility in sea water varies from approximately 2000 mg/L at 10°C to 1100 mg/L at 30°C [16], while O_2 varies between approximately 9 mg/L to 6 mg/L in the same temperature range [17]. Since photosynthesis does not occur overnight, the O_2 level inside the reactor should drop if gas exchanges continue to occur. However, since CO_2 is produced by microalgae as they respirate overnight, its level should increase, especially if an external source of CO_2 continues to inject the gas into the medium. An increased level of CO_2 lowers the pH of the culture as carbonic acid is formed, which can lead to cell death at values outside the ideal range for the species.

On the other hand, the increase in temperature during the day could potentially be more problematic since, in general, microalgae's optimal growth temperature is closer to the maximum growth temperature than to the minimum [15]. This phenomenon can be mitigated by using external heat exchange systems, which are a common feature in many closed reactor configurations.

Table 1 contains the pH and temperature for the maximal growth rate for select commercially relevant microalgae species.

Table 1: Ideal pH and temperature ranges for selected commercially relevant microalgae species.

Species	Ideal pH range	Ideal Temperature range	Reference
Chlorella vulgaris	7-7.5	25-30°C	[18]
Isochrysis galbana	6.8	30°C	[19]
Nannochloropsis salina	8	20°C	[20]
Spirulina platensis	9	30°C	[21]
Dunaliella salina	7.5	28°C	[22]

2.1.2 Reactor Location

Choosing the reactor location can be a challenging task due to various competing factors. These include the land (e.g. slope, ownership, and local geology, etc.), water availability, CO_2 (e.g. from power plants, industrial plants, cement plants, petroleum processing, etc.), nutrients (e.g. from wastewater, agricultural or animal-processing runoff, etc.), and, naturally, the climate (e.g. sunshine hours, temperature, and occurrence of local extreme phenomena) [23]. The climate directly affects two important modeling factors, temperature and irradiation, which are difficult or impossible to control for economically; as such, they are considered to be the most important

factors in deciding a geographical location for a reactor [24]. To help with choosing an ideal reactor location, González-Hernández et al. [24] developed a tool to simulate the biomass production capacity of photobioreactors for different microalgae species, considering only the local climate; although this tool simulates only open reactors, the same methodology could be extended to closed photobioreactors as well.

Another important factor that has to be accounted for when modeling outdoor cultivations is the effect the environment surrounding the reactor has on the solar irradiance reaching the cells. One can consider the sunlight reaching a specific surface, such as a bioreactor, to be composed of different parcels: direct, which is that light coming directly from the sun; diffuse, which is that light that is scattered through the atmosphere; and reflected, which is the light reflected off the ground, buildings, etc. Pyranometers (instruments that measure irradiance) can measure global horizontal irradiance, which is the sum of these three parcels. The remaining parcels can be estimated using several geometric considerations [12].

Although direct sunlight is the major factor source of energy, it can also lead to photoinhibition (as explained in Section 2.2.1.1); in contrast, diffuse and reflected sunlight consist of lower-energy photons with a homogenous distribution, which minimizes this effect. They are also an important source of light energy for the culture, and can contribute to over 55% of productivity in vertical flat-panel reactors [2]. Horizontal systems, meanwhile, have a much more significant exposure to direct sunlight, and a smaller contribution from backscattered diffuse irradiation [2]. As such, these parcels cannot be disregarded when choosing the reactor location, elevation, and modeling approach.

2.1.3 Reactor Design

The reactor type, geometry, and construction also affect the way sunlight enters the broth contained inside, with the angle of the reactor in relation to the sun being of particular importance. There are two main types of closed photobioreactors: flat panel and tubular. Due to their different geometries, their modeling can vary significantly.

2.1.3.1 Flat Panel Reactors

Flat-panel reactors consist of a narrow panel made of two transparent material sheets, separated by just a few centimeters, where the broth is located; this configuration allows for optimal use of solar radiation since high area-to-volume ratios can be achieved [25]. The reactor may be disposable, for example, if it is entirely made of plastic, or reusable, for example, in cases

where the transparent material is glass mounted on a metal frame. Both types are shown in Figure 1.

Figure 1: Glass (left) and plastic (right) flat panel photobioreactors. Courtesy of A4F.

Carbon dioxide is commonly injected through the bottom of the reactor using a sparger, which creates gas bubbles that promote both mixing of the culture and gas exchange. The oxygen-rich bubbles are removed through a purge at the top of the reactor. Due to their simple geometry, the light distribution inside the reactor is considered to be uniform [26], and it can be accurately described using just one dimension [12].

2.1.3.2 Tubular Reactors

Tubular reactors consist of long, interconnected tubes where the broth constantly circulates through the action of an airlift or a mechanical pump [27]. At the end of the loop, the broth is deaerated in a separate vessel [25] to remove the oxygen produced by photosynthesis, which is toxic to the cells in high concentrations. This is also where the broth is aerated with carbon dioxide, either through direct air injection, pure CO_2 injection, or a mixture of both.

Tubular reactors can be subdivided based on the configuration of the tubes, as shown in Figure 2.

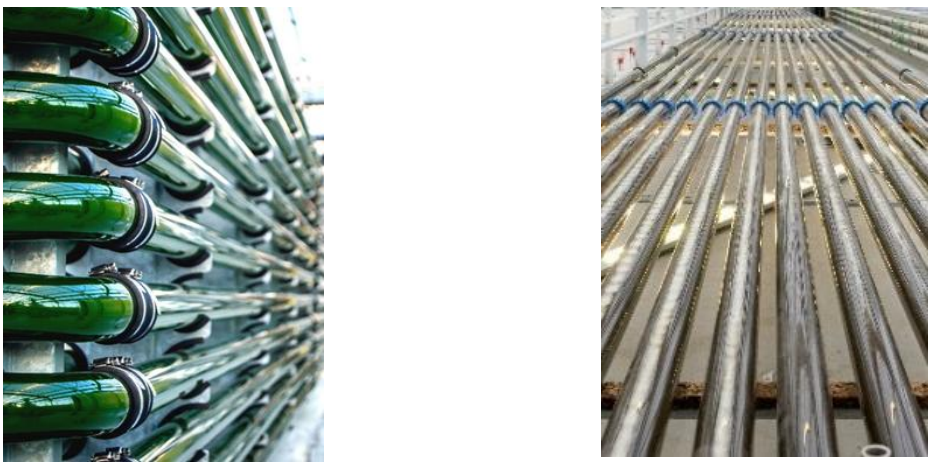

Figure 2: Serpentine / MHT-PBR (left) and manifold / UHT-PBR (right) tubular reactors. Courtesy of A4F.

Serpentine or multilayered horizontal tubular reactors (MHT-PBRs) consist of straight tubes connected by U-bends to form a flat loop (the photostage) that may be arranged in multiple layers [25], either horizontally or vertically. In manifold reactors (or unilayer horizontal tubular reactors, UHT-PBR), a series of parallel tubes is connected at the ends by two manifolds, one for the distribution of the broth and the other for the collection [25]. Manifold reactors have advantages over serpentine reactors, namely the reduction of head losses, lower oxygen concentrations [25], and lower energy consumption since about 15% of the energy consumed in serpentine reactors is lost in moving the broth through the U-bends [2].

Due to their more complex geometry, modeling the light distribution inside tubular reactors is much more challenging and requires the use of at least two dimensions.

2.1.4 Spectrum from Sunlight and LEDs

The modeling of any outdoor photobioreactor requires some measure of the amount of incident light hitting the reactor, coming from the sun, that is, the solar irradiance. However, the sun as a light source is fundamentally different from artificial light sources, which might lead to discrepancies between indoor and outdoor cultivations using different types of light.

Photosynthetic organisms can adapt their metabolism when exposed to narrow wavelengths of light. When there is no need for a particular wavelength to induce a particular metabolite, most indoor cultivations are grown under white LED lights; however, these do not have a uniform distribution of wavelengths but, instead, usually have two separate peaks around 450 and 550 nm [28, 29]. On the other hand, sunlight is not uniform either (see Figure 3). Therefore, it is to be expected that growth under indoor / lab conditions (which are the most common in the literature) will not be representative of growth in outdoor conditions and that some microalgae will grow better in one scenario compared to the other.

To better understand the influence of different wavelengths on microalgae growth, the terminology and quantities used will be clarified in this section.

In all modeling equations involving microalgae, the light energy emitted by the light source (be it the sun or artificial light) is usually denoted as I_0. However, there are two different but complementary ways to describe I_0:

- As the total number of photons passing through a certain area (photon flux density, or *PFD*, $mol_{photons}\ m^{-2}\ s^{-1}$). Instead of moles, older papers may also use an obsolete unit called the Einstein [2].
- As the energy imparted by those photons (radiance, $W\ m^{-2}$).

Radiance can be obtained by integrating another related quantity, the spectral flux density (*SFD*), over a certain wavelength range. *SFD* is a measure of the energy transferred by electromagnetic radiation per unit wavelength through a certain area; the unit is called the Janksy, or $W\ m^{-2}\ nm^{-1}$.

In the case of microalgae cultivation, I_0 is usually defined over a range called PAR (Photosynthetic Active Radiation), which ranges from 400 to 700 nm. I_0 can thus be defined as the photon flux density of the PAR and can be calculated with Equation (1.

$$I_0 = PFD_{PAR} = \int_{400}^{700} PFD_\lambda d\lambda \tag{1}$$

where PFD_{PAR} is the photon flux density in the PAR region of the spectrum, and PFD_λ is the photon flux density for each infinitesimal wavelength range.

Using the second definition, I_0 can also be the radiance in the PAR range, that is, the total amount of energy transmitted. The SFD_λ, or the amount of energy transmitted by a single wavelength, can be calculated from the PFD_λ using the Planck relation [30].

$$SFD_\lambda = PFD_\lambda \times h \cdot v \cdot N_A = PFD_\lambda \times \frac{h \cdot c \cdot N_A}{\lambda} \tag{2}$$

with h being the Planck constant (6.62607015×10^{-34} J·s), SFD_λ the spectral flux density of a given source of light, N_A the Avogadro's constant ($6.02214076\times10^{23}\ mol^{-1}$), v the photon frequency, c the speed of light (299,792,458 m s^{-1}) and λ the wavelength (m).

The radiance is thus the integral of all SFD_λ over the band of interest (in this case, PAR).

$$\begin{gathered} I_0 = SFD_{PAR} = \int_{400}^{700} SFD_\lambda d\lambda \\ I_0 = \int_{400}^{700} \frac{h \cdot c \cdot N_A}{\lambda} \times PFD_\lambda d\lambda = h \cdot c \cdot N_A \int_{400}^{700} \frac{PFD_\lambda}{\lambda} d\lambda \end{gathered} \tag{3}$$

The photon and spectral flux density of sunlight within the PAR is illustrated in Figure 3.

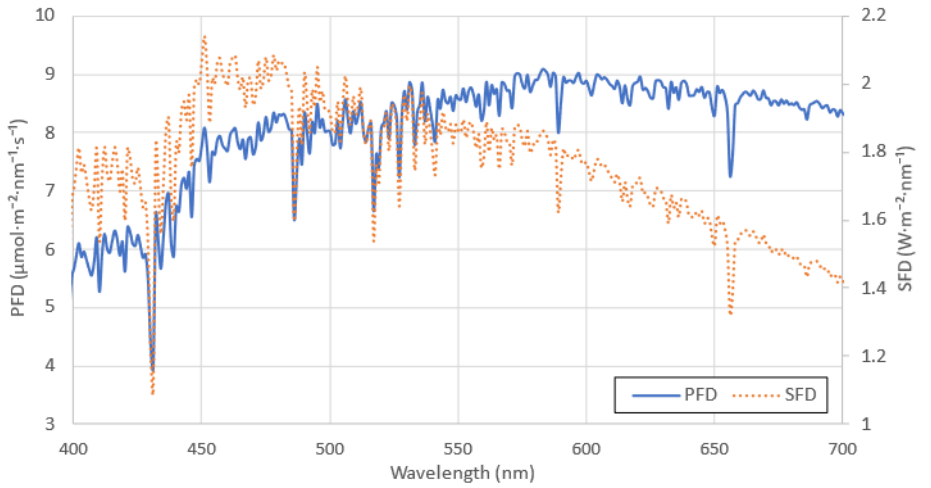

Figure 3: Solar spectrum within the PAR range, in units of photon flux density. Adapted from [31].

The difference between these two quantities is essentially the difference in energies transmitted by each wavelength of light: longer wavelengths transmit less energy, as per the Planck relation. Which of these quantities should be used in microalgae modeling depends on whether distinguishing different wavelengths is important or not. Radiance is potentially more useful when the important factor for the modeling is the total energy absorbed by the culture. On the other hand, *PFD* is more useful when the effects of each individual wavelength are considered, since it counts how many photons of a certain wavelength hit the reactor and not their energy.

The conversion between one quantity and the other depends on the source of light used as different wavelengths of light have different energies, as per the Plank relation. Pessi et al. used a value of 2.02 J/μmol for sunlight [32], taken from an earlier work [33].

Some older texts also use units of illuminance, either lux (lumen m^{-2}) or foot-candle (lumen ft^{-2}), in their models. Illuminance is a measurement of the perceived power of light as detected by the human eye, and is calibrated using a luminosity efficiency function (V_λ), which is standardized by ISO standard ISO/CIE FDIS 11664-1.

The conversion between these units and PFD or SFD is more complex because it depends on the spectrum of the original light source used and requires additional integration. Formally, this is expressed in Equation (4.

$$\varphi_v = 683.002 \int_{400}^{700} V_\lambda SFD_\lambda d\lambda \qquad (4)$$

where φ_v is the luminous flux over a given area (lumen m^{-2}).

The use of Illuminance is discouraged since it is a unit calibrated to the human eye and does not necessarily reflect how microalgae utilize light in their metabolism. A table of conversion

factors from photometric (lux), radiometric (W m^{-2}) and photometric (µmol m^{-2} s^{-1}) can be found in the work of Thimijan and Heins [34].

2.2 Microalgae growth in photobioreactors

Photoautotrophic microalgae growth is similar to that of all other microorganisms. They have the same basic nutritional needs: carbon, nitrogen, phosphorus, and various micronutrients (often species-specific). However, what distinguishes photosynthetic microalgae from other microorganisms is their ability to incorporate carbon from CO_2 dissolved in the water, using energy from light, through the process called photosynthesis.

2.2.1 Photosynthesis

Photosynthesis can be described by the following general equation:

$$Photons + CO_2 + H_2O \rightarrow CH_2O + O_2 + Heat \quad (5)$$

This process converts energy from light into chemical energy (in the form of ATP and NADPH, and also liberating heat), which is then utilized by the cells to synthesize organic carbon (represented by CH_2O) from inorganic carbon in the form of CO_2. The reaction is divided into two steps: the light reactions, which occur in the membranes of the thylakoids, structures inside the cell's chloroplast; and the dark reactions, also known as the Calvin cycle, which take place in the stroma of the chloroplast. A diagram of these reactions is shown in Figure 4.

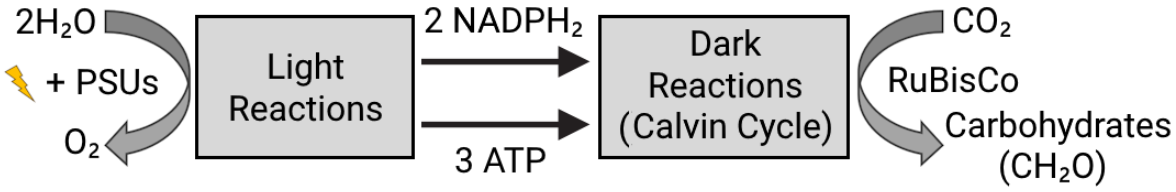

Figure 4: Major products of the light and dark reactions of photosynthesis (adapted from [2]). The process of photosynthesis is divided into two stages, the light reactions and dark reactions (also known as the Calvin cycle). The light reactions, occurring in the PSUs, result in the production of $NADPH_2$, ATP and O_2. The dark reactions, which occur in the stroma, represent the reduction of carbon dioxide and the synthesis of carbohydrates using the $NADPH_2$ and ATP produced in the light reactions.

The membranes of the thylakoids contain photosynthetic pigments (mainly chlorophyll, but also other accessory pigments like carotenoids) and proteins coupled to a reaction center, forming the photosynthetic units (PSUs). These are sensitive to electromagnetic radiation within the PAR range, from 400 to 700 nm, roughly corresponding to the visible light spectrum. When one photon of light is absorbed by one molecule of chlorophyll, it causes it to lose one electron. This electron is then transmitted to a transport chain that ultimately leads to the reduction of NADP to NADPH.

Additionally, this chain also causes a proton gradient within the thylakoid membrane, which is taken up by ATP synthase to produce ATP. The original chlorophyll molecule regains its lost electron from the photolysis of a water molecule, which ultimately leads to the release of O_2 [27].

In the light-independent reactions, the enzyme RuBisCo captures CO_2 from the atmosphere and combines it with a five-carbon sugar to produce two molecules of a three-carbon sugar intermediate. Part of these molecules is combined with the recently produced NADPH and ATP to regenerate the original five-carbon sugar, thus continuing the cycle, while the rest enter the cell's central metabolic pathway and will be used to produce glucose and, ultimately, all other organic compounds of the cell [27].

2.2.1.1 Photosynthesis-Irradiance Curves

Light-response or photosynthesis-irradiance (PI) curves represent the fundamental relationship between irradiance and photosynthesis rate, often separated into three different light zones: a limitation zone, a saturation zone, and an inhibition zone. These regimes are shown in Figure 5.

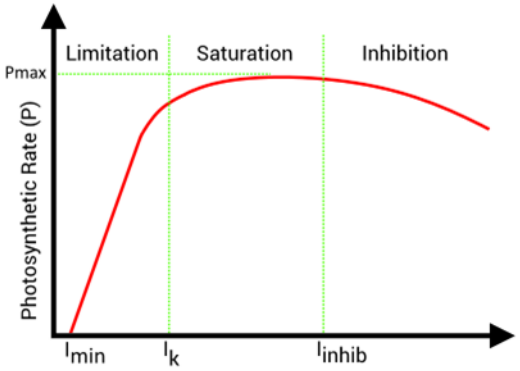

Figure 5: A schematic of a typical PI curve showing the three light regimes experienced by microalgal cells: limitation, saturation, and inhibition. Adapted from [35] and [36].

Before the limitation zone, there is a I_{min} threshold before which no growth occurs due to, for example, back-reactions independent of the energy input rate; this value can be as high as 20 nmol m^{-2} s^{-1} [37]. In the limitation zone, the photosynthetic rate is proportional to the light intensity since it is limited by the rate at which photons can be captured in the light-dependent phase of photosynthesis. In the saturation zone, beyond the saturation threshold I_k, the cells become "light-saturated" since the photosynthetic rate is now being limited by the rate of light-independent reactions that occur after the light-dependent reactions [38].

In the inhibition zone, beyond the threshold I_{inhib}, the rate of photosynthesis starts to decrease due to the deactivation of key proteins in the photosynthetic units of the thylakoids [39] and

saturation of the electron transport chain, or even due to irreversible photooxidation of pigments [40]. The values for which photoinhibition occurs varies greatly between species and if the cells are adapted to lower irradiation values. As a general rule, values above 300 µmol m^{-2} s^{-1} lead to photoinhibition in microalgae [40], which is much less than the 2000 µmol m^{-2} s^{-1} of direct sunlight. The photoinhibition effect is still observed in dense, turbulent culture because the top layers are exposed to near-full sunlight, although the effect can minimized by denser cultures with more intense mixing [2]. Special photobioreactor designs can be used, but the increased efficiency often does not compensate for the higher energy requirements [2].

PI curves do not consider transient effects, such as light-acclimatization, where the inhibition threshold is changed due to cells acclimatizing to the current light level by, for example, changing their pigment content [38].

The photosynthetic rate (P) is the rate at which the photosynthetic units (PSUs) of the cell can capture photons. This is difficult to measure in practice, so other easily measurable quantities of the system can be used as surrogates instead, since they are considered proportional to the photosynthetic rate and result in similar curves [41, 42]. Oxygen dissolved in the culture is directly correlated to the photosynthetic rate since oxygen is produced by photosynthesis. Carbon dioxide dissolved in the culture is indirectly correlated to the photosynthetic rate since it is consumed by photosynthesis, but it also depends on the pH level, which can be changed by other external factors. Finally, the specific growth rate can also indirectly correlate to the photosynthetic rate if light is the only limiting factor in growth.

2.2.1.2 Effect of Wavelength

As mentioned previously, only a very small section of the electromagnetic spectrum (PAR radiation) is used for photosynthesis. Since sunlight is distributed between all wavelengths within the PAR range (see Section 2.1.4 Spectrum from Sunlight and LEDs), most species in the wild are exposed to radiation of all wavelengths. However, there are certain species whose metabolism changes depending on which wavelengths of light they are exposed to. Many of the resulting metabolites are pigments, thus leading to the hypothesis that they are being accumulated as an adaptation of the cells to the new environment (photo-adaptation), either to better utilize the energy source they are being exposed to or as protection against the most harmful types of radiation (photo-protection).

Induction of certain metabolites can be achieved by using LED lights of specific wavelengths [43]. In outdoor cultivations, supplementary LED lights can be used in addition to sunlight to induce

the desired metabolic state. There is also the possibility of using selective filters to block out certain wavelengths and allow others to come into contact with the cells.

Coward et al. optimized the growth of *Porphyridium purpureum* (a type of red alga) utilizing red, green, and blue LED lights, obtaining higher cell concentrations using green and RGB light (6.5 g L^{-1} after 10 days compared to 1.5 and 1 g L^{-1} for red and blue light, respectively) [44]. However, the highest yields of valuable products, such as eicosapentaenoic acid, were obtained by combining all three monochromatic LEDs (43% DCW compared to between 23 and 29 % using monochromatic light).

Teo et al. grew *Tetraselmis sp.* and *Nannochloropsis sp.* under red, blue, white, and red-blue LEDs, obtaining better results under blue light compared to white light in terms of specific growth rates (1.47 and 1.64 day^{-1} under blue light compared to 1.44 and 1.59 under white light, respectively) and lipid production (around 103 a.u and 980 a.u under blue light compared to 92 a.u. and 290 a.u., respectively) [45].

Amaro et al. explored the use of a combination of red and blue LED lights on *Scenedesmus obliquus,* a producer of antioxidant compounds, and found that blue light led to higher productivity and higher fatty acid contents when compared to other LED colors (0.27 day^{-1} vs. 0.12 day^{-1}), but that red light led to a higher concentration of antioxidant compounds and carotenoids when compared to the control (3 mg d_{DCW}^{-1} with red LEDs compared to 1.5 with blue LEDs). Near-infrared radiation also altered the profile of antioxidant production [46].

Vadiveloo, et al. used colored acetate filters to condition a strain of *Nannochloropsis sp.* to grow under different wavelengths. The authors concluded that blue light filters allowed for higher biomass productivity, calibrated by the amount of energy given, when compared to unfiltered white light (7.22 vs. 6.5 mg $L^{-1}d^{-1}W^{-1}m^2$), while the microalgae had reduced productivity under red and blue-green light (6.31 and 2.86 mg $L^{-1}d^{-1}W^{-1}m^2$), and no growth under green light. The authors proposed that light filters could be used to increase biomass productivity while reutilizing the remaining light spectrum for photovoltaic energy production, increasing efficiency [47].

Raeisossadati et al. used red light solar concentrators (LSCs) to convert the PAR spectrum into red light peaking at 650nm and grew a strain of *Scenedesmus sp.* in a paddle wheel reactor. The authors reported an increase of 18.5% in the biomass productivity to 9.4 g m^{-2} d^{-1}, which would allow a significant reduction of operating costs if the cultivation area were reduced accordingly [48].

2.2.2 Culture Self-Shading, Light/Dark Cycles & Flashing-Light Effect

Self-shading is a phenomenon where cells in shallower parts of the culture (closer to the light source) absorb most of the light, effectively leaving the deeper parts of the culture in permanent shadow, which can even lead to cell death. Since the objective of small-scale cultures is usually to either maintain a certain species in reserve, optimize growth conditions or otherwise obtain data about a certain species, cell densities are often kept low, so the self-shading phenomenon can be considered negligible.

In more concentrated cultures (usually the case for outdoor cultivations), self-shading can be avoided by increasing the mixing of the culture, either by mechanical mixing or by aeration, which also increases operation costs. This culture mixing causes what are called light/dark cycles, where the cells continuously move from the illuminated area (where the light-dependent reactions of photosynthesis can occur) and the shaded area (where only the dark-dependent reactions can occur) [2]. This cellular movement is more or less random and depends on the reactor configuration, the turbulence inside the reactor, etc. However, a thinner reactor does not necessarily improve growth rates. Saccardo et al. showed that reactors that are too thin cause the cells to be constantly exposed to sunlight, thus causing light inhibition and loss of productivity [49].

Due to the nature of the reactions occurring in the PSUs, there is an interval of about 100 ms between the capture of a photon and the production of NADPH and ATP, during which the PSU is in an excited state and cannot absorb additional photons. Therefore, photons hitting the same PSU during this period are “wasted” and unable to be converted into cellular energy [9]. Thus, cells exposed to 100 ms cycles of light and dark periods waste less light energy than cells exposed to continuous light [50, 51]. This increase in overall photosynthetic efficiency is called the “flashing-light effect”. It is particularly relevant in very dense cell cultures where cells deeper in the culture are effectively “in the dark” due to light absorption by the culture closer to the light source. Thus, a reactor configuration that causes the cells to cycle between the light and dark regions of the broth at around a 100 ms period is more efficient than a reactor with a different cycle [9]. Experimentally, Grobbelaar et al. demonstrated that higher light/dark frequencies were perceived by microalgae as high light conditions whilst allowing time for dark reactions to occur, thus increasing photosynthetic efficiency [52, 53].

2.2.3 Other Factors Influencing the Growth of Microalgae

Although irradiation is considered the main factor influencing growth in photosynthetic microalgae from a modeling perspective, many other internal and external factors influence

growth. These other factors must be taken into consideration when growing microalgae since they are not only necessary for growth but can also turn into the limiting factor. Four factors will be explored, in order of their importance: nutrients, temperature, pH and carbon uptake, and finally, endogenous respiration.

2.2.3.1 Nutrients

For photosynthetic organisms like autotrophic microalgae, some essential nutrients are needed, mainly a source of nitrogen and phosphate; some specific microalgae species require additional nutrients, like sulfates or trace micronutrients [27] like iron, magnesium, and zinc, among other metals, and silicon for diatoms. Usually, these nutrients are provided as chemical salts dissolved in an aqueous solution [27].

Nutrient yield coefficient varies greatly between microalgae species. Resman et al. [54] reported a yield of 28 $g_{biomass}/g_N$ for a mixed culture of S*cenedesmus dimorphus* and *Scenedesmus quadricauda* in a raceway pond. Ermis et al. [55] reported 10.7 $g_{biomass}/g_N$ and 98 $g_{biomass}/g_P$ for culture of wild-type microalgae.

The required nutrients can be provided in three different regimes: batch, where the nutrients are supplied at a high dose at the beginning of the cultivation; ”drip-feed”, where nutrients are occasionally replenished during the cultivation; and continuous, where nutrients are continuously provided [27].

2.2.3.2 Temperature

Excluding irradiation, the only factor not directly controlled or potentially not economically viable to control in an industrial setting is temperature, as nutrients, pH, carbon concentration, and oxygen can all be changed by controlling nutrient inflow or aerating the culture [24]. The adequate temperature for a specific microalgae culture is directly related to its cellular, morphological and physiological responses. Higher temperatures enhance cellular metabolism, including carbon fixation and absorption, and influence the solubility of nutrients and gases. However, extremely high temperatures can lead to the denaturation of proteins and thus inhibit many cellular mechanisms. Conversely, low temperatures slow down metabolism, potentially leading to cell death. Therefore, it is important to maintain an optimal temperature for microalgal growth. This optimal temperature depends on the species; mesophilic species, the most used in large-scale microalgae cultivations, have optimal growth around 18 to 30 ºC [56]. Cryophilic and thermophilic species can have optimal temperatures outside this range and require special cultivation measures.

A common way to increase and control the temperature of the reactor, especially in colder climates, is using greenhouses. However, Pessi et al. demonstrated that, under different scenarios, the usage of a greenhouse is only advantageous to prevent culture contamination (in raceway ponds) and to increase productivity in colder regions susceptible to photoinhibition due to longer periods exposed to sunlight [32].

2.2.3.3 pH and Carbon

For each microalgae species and strain, there is an optimal pH where the growth rate is maximized. Furthermore, pH is also an indirect measure of the total inorganic carbon, since CO_2, the ultimate source of carbon in microalgae cultures, readily dissolves in water, forming carbonate and bicarbonate ions, which lower the pH and buffers the solution. For these reasons, pH is a parameter that is closely monitored during microalgae cultivation.

Inorganic carbon in the form of carbon dioxide is often dissolved in the culture at higher concentrations than the equilibrium in normal atmospheric conditions [27] which, in turn, lowers the pH. At the same time, for pH levels typical for microalgae growth, between 6.5 and 10, bicarbonate is the most common form of carbon, which most microalgae species are able to utilize [57]; incorporation of carbon by the cells removes these ions from the culture, increasing the pH. Therefore, the pH of the culture, and indirectly its carbon needs, are kept at optimum values via CO_2 injection.

For most studies, carbon is usually considered to be in excess, and therefore, its limiting effect is neglected for large-scale cultivations. However, poor mixing, high culture densities or lack of carbon dioxide injection may lead to growth limitations [58]. Therefore, increasing the amount of carbon dioxide in the system may lead to an increase in productivity under these conditions.

2.2.3.4 Oxygen Concentration

Algal cultures are exposed to high concentrations of O_2 resulting from their own photosynthetic activity. This increase results in inhibition of photosynthesis mainly due to O_2 also binding to Rubisco, which reduces its catalytic activity on CO_2, ultimately resulting in lower productivity [59]. This inhibition is further compounded by high irradiances and temperature and is species-specific. Excess oxygen is usually removed in close photobioreactors through air exchange.

Kazbar et al. [60] reported a loss of productivity at O_2 concentrations above 31 mg L^{-1} in *Chlorella vulgaris* cultures. Gao et al. [61] tested the productivity of *Monoraphidium minutum* and

Scenedesmus obliquus in raceway reactors, reporting a loss of 37 and 26% of productivity around 30 mg L^{-1}, agreeing with the previous findings.

Due to productivity loss due to oxygen accumulation, the length of closed photobioreactors cannot be infinite, and is generally kept below 80 meters if the flow rate is between 0.3 and 0.5 m s^{-1} [59].

2.2.3.5 Endogenous Respiration

Like all other eukaryotic organisms, microalgae also respirate, using oxygen and glucose to produce energy in the mitochondria, the powerhouse of the cell. Endogenous respiration consumes chemical energy obtained from photosynthesis during the day and energy stored in organic material at night [9], due to the lack of available energy sources other than energy reserves. This leads to a reduction in the total mass of the culture during the night, which can be considered using certain models. The endogenous respiration factor is mainly applicable to outdoor cultivation, which, in most cases, uses only solar radiation as a light source.

2.3 Modeling of Microalgae Cultures

The base assumption for most photobioreactors is that light (and thus the carbon usage rate) is the limiting factor for growth. This is valid for photobioreactors where the objective is only to produce biomass without the need to induce the production of a specific metabolite. However, this is not strictly the case for many photobioreactors. Thus, a comprehensive model should consider the possibility of different limiting nutrients and other factors. Nevertheless, how incident light I_0 is transformed into biomass is central to any photobioreactor model. Apart from the photosynthesis model, several other factors can potentially affect the growth of microalgae, in particular temperature, nutrients, and endogenous respiration, which will also be explored in this review.

2.3.1 Photosynthesis Model

The photosynthesis model relates the light that effectively reaches the cells with the growth rate of the microalgae, essentially treating light as a substrate. Growth models can be expressed in various forms, such as carbon dioxide consumption, oxygen production, or specific growth rate of the microalgae; these relationships all result in similar PI curves. It can reasonably be said that the photosynthesis model is the centerpiece of any modeling effort since it is by far the most complex part and the one most prone to variation.

Béchet et al. [62], in their extensive review of the various approaches to this problem over the years, grouped the studied models into three types: I, II, and III. This will be the same approach used

in this review. An important element of the description of photosynthesis in a homogenous culture is the effect of the attenuation of light through the medium. Most state-of-the-art articles detailing the modeling of photobioreactors consider this effect directly in the photosynthesis model for simplification. In their discussion, Béchet et al. [9] integrate the effects of light gradients as part of the various growth models they present; however, as the authors themselves point out, it is, in essence, advantageous to separate the various processes involved, which is how this paper will approach the issue.

2.3.1.1 Light Attenuation Inside a Reactor

More advance models (those of Type II and III, or those requiring the average irradiation, as explained in the latter sections) require knowing the light distribution inside a reactor. A light distribution equation accounts for the effects of cell density on the light that is transmitted through the medium, and how it is absorbed, scattered, or dispersed by the culture.

The Radiative Transfer Equation (RTE) is an accurate equation to predict light attenuation along a medium. However, since solving this equation is computationally intensive, there are many approximations to the direct use of the RTE. The most famous is the Beer-Lambert law (Equation (6), which is derived for a homogeneous medium with no scattering and at local thermodynamic equilibrium [63]:

$$I(z) = I_0 \, exp(-E_a X z) \tag{6}$$

with z (m) as the direction of light propagation (assuming the light propagates in only one direction), X (g L^{-1}) as the particle concentration, and E_a (L g^{-1} m^{-1}) as the mass attenuation (or absorption) coefficient. However, the Beer-Lambert law is often a crude approximation that is not valid for very concentrated media, which is usually the case for microalgae reactors.

A more exact approximation of the RTE is the two-flux approximation (Equation (7) [64]. In this approximation, the light is assumed to travel in a single direction, z, and the scattered radiation is confined to just the forward (F^+) and backward (F^-) directions [65].

$$I(z) = F^+(z) + F^-(z)$$

$$\frac{dF_z^+}{dz} = -E_a X F^+ + \frac{1}{2} E_s X (F^- - F^+) \tag{7}$$

$$\frac{dF_z^-}{dz} = -E_a X F^- + \frac{1}{2} E_s X (F^- - F^+)$$

with E_S (L g^{-1} m^{-1}) as the mass scattering coefficient. The boundary conditions depend on the reactor configuration. For example, for a reactor with optical thickness L (m) that is being

illuminated only on one side by a homogenous incident radiant energy flux F_0 (z=0) and is covered by absorbent black paper at the opposite side (z=L) [64]:

$$z = 0,\ F_z^+ = F_0$$
$$z = L, F_z^- = 0 \tag{8}$$

A simplified version of the two-flux model was used by Cornet and Dussap [66]:

$$I(z) = I_0\, exp\left(-\frac{1+\alpha}{2\alpha}E_a X z\right);\ \alpha = \sqrt{\frac{E_a}{E_a + 2bE_s}};\ E_a, E_s, b\ const. \tag{9}$$

with b as the backscattering coefficient.

A hyperbolic version of the Beer-Lambert law was proposed by Yun and Park [67]:

$$I(z) = I_0\, exp\left(-\frac{k_1 X}{k_2 + X}z\right) \tag{10}$$

with k_1 (m^{-1}) and k_2 ($g\ L^{-1}$) as model constants.

Katsuda et al. proposed a different hyperbolic model [68]:

$$I(z) = \frac{I_0}{(k_L z + 1)^{n_1}(k_X X z + 1)^{n_2}} \tag{11}$$

with k_L (m^{-1}), k_X ($L\ g^{-1}m^{-1}$), n_1, and n_2 as model constants.

2.3.1.1.1 Calculation of the Average Light Intensity

The average light intensity (I_{av}) inside a given reactor can be determined by integrating the chosen light distribution equation over the entire depth of the reactor. However, many authors have derived several approximations for different reactor geometries.

For a flat panel reactor, Bernard et al. derived Equation (12 using Beer-Lambert's law [41]:

$$I_{av} = \frac{I_0}{\xi z}(1 - exp(-\xi z)) \tag{12}$$

with ξ as the light attenuation parameter, which can depend on E_a, X, among others.

Expanding upon Equation (6, Viruela et al. proposed Equation (13 for a membrane photobioreactor with a geometry similar to a flat-panel photobioreactor, considering k_w as the water extinction coefficient [69].

$$I_{av} = \frac{I_0 \cdot (1 - exp\,(-(k_w + E_a \cdot C_{b\cdot}) \cdot d))}{(k_w + E_a \cdot C_{b\cdot}) \cdot d} \tag{13}$$

Fernandéz et al. proposed Equation (14 for the average light intensity inside a tubular reactor, similar to the equations derived for planar reactors [70]:

$$I_{av} = \frac{I_0 \cdot \tau}{E_a X z}(1 - exp(-E_a C_X.z)) \quad (14)$$

with τ being the distribution factor, the fraction (between 0 and 1) of solar irradiation available to the reactor. This equation assumes the Beer-Lambert law as the light distribution equation.

Fernandéz et al. deduced an equation for the average irradiation inside a tubular reactor as shown in Equation (15 [71].

$$I_{av} = \frac{1}{\pi \cdot R^2}\left(\int_0^R \int_0^{2\pi} I_{direct} r \cdot dr d\varphi + \frac{1}{2\pi}\int_0^r \int_0^{\varphi} \int_0^{\epsilon} I_{disperse} r \cdot dr d\varphi\right) \quad (15)$$

2.3.1.2 Models Based on Incident Light Intensity (Type I-A)

A Type I model is based on the assumptions that there is homogenous light distribution inside the reactor due to reactor mixing, that is, that the irradiance every cell experiences (I_{cell}) is the same for all cells in the culture. Type I models can be further subdivided into two types, named I-A and I-B.

Type I-A models assume that the light that reaches each cell is equal to the light reaching the external walls of the system (I_0). This is expressed in Equation (16.

$$\mathrm{I_{cell}} = \mathrm{I_0} \quad (16)$$

This approximation leads to relatively simple models that do not involve the reactor geometry.

In Type I-B models, it is assumed that the light reaching all cells is not equal to the incident radiation, but involves the average light inside the reactor I_{av} (W m^{-2} or $mol_{photons}$ m^{-2} s^{-1}) [67]. On average, cells are assumed to receive equal amounts of light [58]. This is expressed in Equation (17.

$$\mathrm{I_{cell}} = \mathrm{f(I_{av}, I_0)} \quad (17)$$

As discussed in Section 2.3.1.1, the calculation of I_{av} requires knowing the light attenuation inside a reactor. The simplest Type I-B models use exclusively $I_{av,}$ replacing I_0 in the same growth equations used for Type I-A. This approach is the most reported in the literature. Furthermore, some Type I-B models integrate both I_{av} and I_0 in the same equation. These models are discussed in Section 2.3.1.3.

A summary of selected growth models of this type proposed by different authors can be found in Table 2. This table includes both references to models using incident irradiation and average irradiation. There are a variety of models with different parameterizations; however, mathematically, many of these models can be grouped into the same families. A diagram with a

collection of different models found in the literature and how they relate to each other can be found in Figure 6.

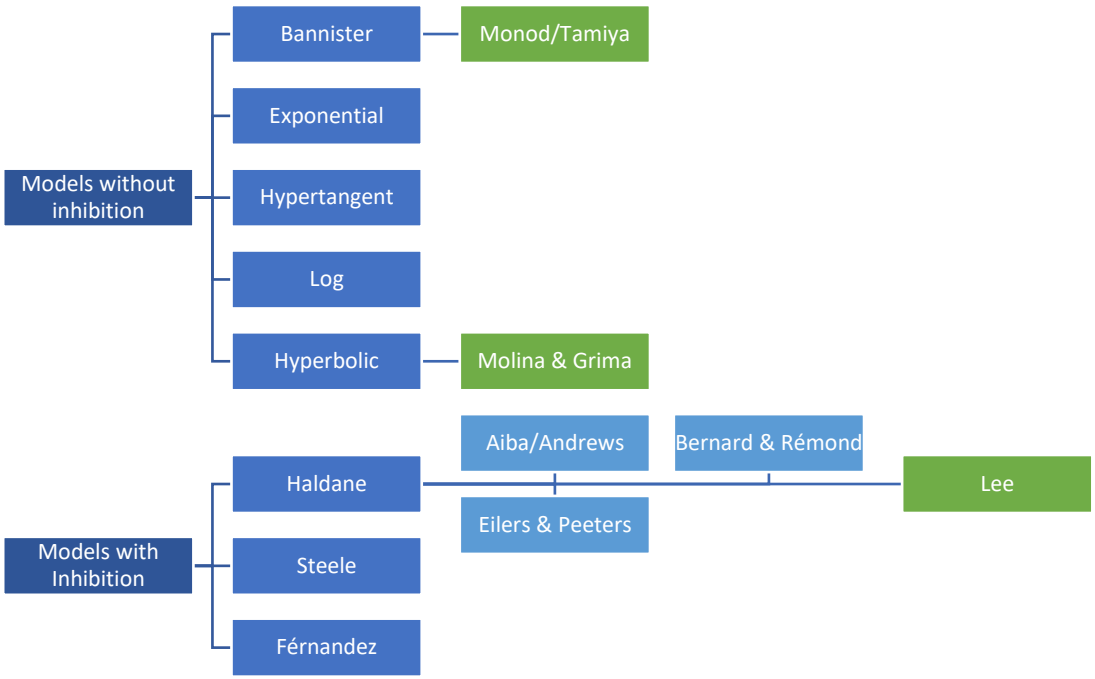

Figure 6: Diagram of the relation between different models found in the literature. Models in a light shade of blue are reparameterizations of the parent model. Models in green are edge cases of the parent model.

Table 2: Assorted collection of photosynthesis models from the literature. μ_{max} can represent the growth rate in terms of biomass or photosynthesis rate. Values are presented in their original units, except for Einstein, an obsolete unit which is redundant with the mol in this context. The nomenclature of the equation parameters was changed to that used in the original papers to unify the nomenclature. This table includes both references to models using incident irradiation and average irradiation (collectively referred to *I* in the table), as the mathematical formulas are the same.

Model	Source	Formula	Parameters	System Size	System and Photoperiod	Species
Models without inhibition						
Monod	[72]	$\mu = \mu_{max}\frac{I}{K_S + I}$ (18)	Unavailable	500 mL 40 L	Indoor (projector lamp) and Outdoor	*Chlorella ellipsoidea*
	[73]		μ_{max} = 0.1617 h^{-1} K_S = 17.04 W m^{-2}	13.5 L	Indoor (white fluorescent)	*Spirulina platensis*
	[74]		μ_{max} = 1.4 day^{-1} K_S = 215 µmol m^{-2} s^{-1}	Not mentioned	Theoretical	*Chlamydomonas reinhardii*
	[75]		μ_{max} = 0.1090 h^{-1} K_S = 763.7 µmol m^{-2} s^{-1}	5 L	Indoor (fluorescent lamps)	*Isochrysis galbana*
Monod with respiration	[76]	$\mu = \mu_{max}\frac{I}{K_S + I} - R_X$ (19)	μ_{max} = 1.95 mg_{O2} g^{-1} h^{-1} K_S = 10.8 mol m^{-2} day^{-1} R_X = 0.03 d-1	40 mL	Indoor	*Pavloca lutheri*
	[77]		μ_{max} = 43.5 mg_{O2} g^{-1} h^{-1} K_S = 177.2 µmol m^{-2} s^{-1} R_X = 3.66 mg_{O2} g^{-1} h^{-1} (for simulated daylight, 0.215 g L^{-1})	3.58 mL	Indoor (simulated daylight, red light, green light)	*Haematococus pluvialis*
Bannister	[78]	$\mu = \mu_{max}\frac{I}{(I^m + K_S^m)^{1/m}}$ (20)	m = 2	Not mentioned	Indoor	*Chlorella sp.*
	[79]		m = ∞	Theoretical		
	[80]		Various	Not mentioned	Indoor	*Chrorella pyrenoidosa*
	[73]		μ_{max} = 0.2976 h^{-1} K_S = 15.01 W m^{-2} m = 0.4970	13.5 L	Indoor (white fluorescent)	*Spirulina platensis*
Hyperbolic	[81]	$\mu = \mu_{max}\frac{I^n}{I^n + K_S^n}$ (21)	μ_{max} = 0.0426 h^{-1} K_S = 10.92 W m^{-2} n = 5.13	1 L	Indoor (fluorescent lamps)	*Isochrysis galbana*
	[82]		μ_{max} = 1.2 day^{-1} K_S = 181 µmol m^{-2} s^{-1}	18 L	Indoor (fluorescent, simulated daylight)	*Nannochloropsis salina*

Model	Source	Formula	Parameters	System Size	System and Photoperiod	Species
			n = 1.75			
	[83]		μ_{max} = 2.2E-03 mol $_{O2}$ kg^{-1} s^{-1} K_S = 69 µmol m^{-2} s^{-1} m = 0.87	3 m^3	Outdoor (raceway)	*Scenedesmus almeriensis*
Hyperbolic with respiration	[75]	$\mu = \mu_{max} \frac{I^n}{I^n + K_S^n} - R_X$ (22)	μ_{max} = 0.046 h^{-1} K_S = 195.6 µmol m^{-2} s^{-1} n = 2.11 R_X = 0.00385 h^{-1} (not adjusted)	5 L	Indoor (fluorescent lamps)	*Isochrysis galbana*
Log with respiration	[84]	$\mu = A \cdot \log_{10}(I) + B \cdot \log_{10}(X) - \lambda$ 23	A = ln(10)×0.1325 h^{-1} B = - ln(10)×0.0053 h^{-1} λ = - ln(10)×0.356 h^{-1}	Not mentioned	Indoor (projector lamp)	*Chlorella sp.*
Exponential/Poisson	[75]	$\mu = \mu_{max}\left(1 - \exp\left(-\frac{I}{\lambda}\right)\right)$ 24	μ_{max} = 0.064 h^{-1} λ = 456.8 µmol m^{-2} h^{-1} (other experiments available)	5 L	Indoor (fluorescent lamps)	*Isochrysis galbana*
	[85]		μ_{max} = 0.77 day^{-1} λ = 7.14 µmol m^{-2} day^{-1}	1.2 L	Indoor (varies)	*Tetraselmis chui*
Hypertangent	[86]	$\mu = \mu_{max} \tanh(\alpha I)$ (25)	μ_{max} = 36 mol$_{O2}$ mol$_{Chl}^{-1}$ h^{-1} α = 4.6 µmol^{-1} m^2 s	Not mentioned	Indoor (cool-white fluorescent light)	*Gymnodium microadriaticum*

Models with inhibition						
Costache et al.	[83]	$\mu = K_A \frac{I^n}{I^n + K_S \exp(mI)}$ (26)	$K_A = 2.06 \cdot 10^{-5}$ kg_{O2} kg^{-1} s^{-1} $K_S = 174$ µmol m^{-2} s^{-1} $m = 0.0021$ m^2 s µmol^{-1} $n = 1.045$	36 m^3	Outdoor (tubular)	*Scenedesmus almeriensis*
	[87]		$K_A = 4.6 \cdot 10^{-5}$ kg_{O2} kg^{-1} s^{-1} $K_S = 174$ µmol m^{-2} s^{-1} $m = 0.0022$ m^2 s µmol^{-1} $n = 1.19$			
Bernard and Rémond	[96]	$\mu = \mu_{max} \frac{I}{I + \frac{\mu_{max}}{\alpha}\left(\frac{I}{I_{opt}} - 1\right)^2}$ (27)	*Chlorella*: $\mu_{max} = 2.00$ day^{-1} $\alpha = 0.05$ day^{-1} $I_{opt} = 275$ µmol m^{-2} h^{-1} *Nannochloropsis:* $\mu_{max} = 1.85$ day^{-1} $\alpha = 0.12$ day^{-1} $I_{opt} = 2.03 \times 10^8$ µmol m^{-2} h^{-1}	50mL [97]	Indoor	*Nannochloropsis oceanica* *Chlorella pyrnoidosa*
	[32]		$\mu_{max} = 3.5$ day^{-1} $\alpha = 0.024$ day^{-1} $I_{opt} = 571$ µmol m^{-2} h^{-1}	417 L (raceway pond)	Outdoor and Greenhouse	*Tetraselmis suecica*
Eilers & Peeters	[94]	$\mu = \mu_{max}(1+\beta)\frac{2x_I}{x_I^2 + 2\beta x_I + 1}$ $x_I = \frac{I}{I_{opt}}$ (28)	$\mu_{max} = 2.696$ mg_C mg_{Chl}^{-1} h^{-1} $\beta = 0.364$ $I_{opt} = 29.896$ W m^{-2} (converted values)	Theoretical		
	[95]		Parameters not determined	Not mentioned	Indoor (halogen lamps)	*Chlorella vulgaris* *Fragilaria crotonesis* *Straurastrum pingue* *Synechocystis minima*

Haldane / Aiba	[88]	$\mu = K_A \frac{I}{K_S + I + \frac{I^2}{K_I}}$ (29)	K_A = 0.54 $mmol_{O2}$ mg_{Chl}^{-1} h^{-1} K_S= 0.75 µmol m^{-2} h^{-1} K_I= 12 µmol m^{-2} h^{-1} (at 25°C; other temperatures available)	300 mL	Indoor	Various species
	[73]		K_A = 5.4849 h^{-1} K_S = 959.2 W m^{-2} K_I = 0.5817 W m^{-2}	13.5 L	Indoor (white fluorescent)	*Spirulina platensis*
	[75]		K_A = 0.1088 h^{-1} K_S = 195.1 W m^{-2} K_I = ∞	5 L	Indoor (fluorescent lamps)	*Isochrysis galbana*
	[89]		K_A = 0.2274 h^{-1} K_S = 81.38 µmol m^{-2} h^{-1} K_I = 2500 µmol m^{-2} h^{-1}	1.1 L [90]	Indoor	*Chlamydomonas reinhardii*
	[91]		K_A = 3670 mg_{O2} mgX^{-1} h^{-1} K_S = 1963 µmol m^{-2} h^{-1} K_I = 261 µmol m^{-2} h^{-1} (parameters recalculated from a graph)	0.8 L (indoor) 3 m^3 (outdoor)	Indoor (white lamps, simulated solar cycle) and Outdoor	*Isochrysis galbana*
	[92]		K_A = N/A K_S = 60 µmol m^{-2} h^{-1} K_I = 130 µmol m^{-2} h^{-1}	Not mentioned	Indoor	*Nannochloris eucaryotum*
	[93]		K_A = 4.92 day^{-1} K_S = 1.56 µmol m^{-2} h^{-1} K_I = 15.42 µmol m^{-2} h^{-1}	3 L	Indoor (tungsten lamps)	*Chlorella vulgaris*
Lee	[73]	$\mu = \frac{I}{K_I + K_2 I^2}$ (30)	K_1 = 177.9 J m^2 h K_2 = 0.1083 J m^2 s^2	13.5 L	Indoor (white fluorescent)	*Spirulina platensis*

Steele's Inhibition	[98]	$\mu = \mu_{max} \frac{I}{I_{opt}} \exp\left(1 - \frac{I}{I_{opt}}\right)$ (31)	Not Given	Sea	Outdoor	*Sea phytoplanktons*
	[95]		μ_{max} = 1.3 day^{-1} I_{opt} = 140 µmol m^{-2} h^{-1} (for Chlorella)	Not mentioned	Indoor (halogen lamps)	*Chlorella vulgaris* *Fragilaria crotonesis* *Straurastrum pingue* *Synechocystis minima*
	[75]		μ_{max} = 0.0521 h^{-1} I_{opt} = 1020.3 µmol m^{-2} h^{-1} (other experiments available)	5 L	Indoor (fluorescent lamps)	*Isochrysis galbana*
	[99]		Not Given	50 L	Indoor	*Porphyridium purpureum*
	[69]		μ_{max} = 1.8 day^{-1} I_{opt} = 230 µmol m^{-2} h^{-1}	550 L and 220 L	Outdoor	Eukaryotic Microalgae

Because of their simplicity, it has been shown [100] that Type I models do not take into account the flashing-light effect, thus leading to equations whose parameters depend on the species cultivated, cell concentration, incident light intensity, and system size [9].

In the next section, the different relevant families of models will be discussed. For the sake of standardization, many parameters' names were changed from what is commonly found in the literature.

2.3.1.2.1 Monod-Bannister Model Family

As a first approach, a growth model similar to that used by Monod [101] for heterotrophic organisms (Equation (32) can be assumed using light as the substrate:

$$\mu(I) = \mu_{max} \frac{I}{K_S + I} \tag{32}$$

with μ being the specific growth rate (s^{-1}), μ_{max} the maximum specific growth rate (s^{-1}), I the light intensity (W m^{-2} or $mol_{photons}$ m^{-2} s^{-1}), and K_S the light half-saturation constant (W m^{-2} or $mol_{photons}$ m^{-2} s^{-1}) [58].

This model is also often referred to as the rectangular hyperbolic model (due to its shape) or as the Tamiya model, in reference to its use by Tamiya et al. [72]. This model, however, does not consider the effects of photoinhibition, as described in Figure 5.

Some authors also add a term to the Monod equation, R_x, to take into account the effect of endogenous respiration [76, 77].

In 1979, Bannister [80] expanded upon various similar models in the literature, including the work of Blackman [79], producing a more generalized model shown in Equation 33:

$$\mu(I) = \mu_{max} \frac{I}{(I^m + K_S^m)^{1/m}} \tag{33}$$

where m is the shape factor (dimensionless). Many authors then expanded upon this model, later utilizing non-integer values for m.

2.3.1.2.2 Haldane Model Family

This family of models is based on the equation proposed by Haldane for the kinetics of enzyme-catalyzed reactions that exhibit substrate inhibition [102], which independently inspired two other authors [42, 103] to utilize it for the effect of light on growth (for this reason, this model is also often referred to as the Aiba or Andrews model):

$$\mu(I) = K_A \frac{I}{K_S + I + \frac{I^2}{K_I}} \tag{34}$$

with K_A being a constant (s^{-1}) and K_I being the inhibitory constant ($W\,m^{-2}$ or $mol_{photons}\,m^{-2}\,s^{-1}$). The disadvantage of this equation is that the maximum growth rate is not directly obtainable from the equation's parameters, despite the literature often referring to K_A *as* μ_{max}.

In 1978, Eilers and Peeters independently arrived at another form of Equation (34 using PSU theory [104]:

$$\mu(I) = \frac{I}{c + bI + aI^2} \tag{35}$$

where *a* ($m^2\ s\ W^{-1}$ or $m^2\ s^2\ mol_{photons}^{-1}$), *b* (s) and *c* ($W\ s\ m^{-2}$ or $mol_{photons}\ m^{-2}$) are empirical constants.

In the same 1978 paper, the authors rearranged the three parameters to express the optimum irradiance and the maximum growth rate, arriving at Equation 36, which can be called an "explicit" form of Equation (34:

$$\mu(I) = \mu_{max}(1+\beta)\frac{2x_I}{x_I^2 + 2\beta x_I + 1} \qquad \mathrm{x_I} = \frac{\mathrm{I}}{\mathrm{I_{opt}}} \tag{36}$$

with μ_{max} being the maximum growth rate (s^{-1}), β being a shape factor (dimensionless), and I_{opt} being the optimum irradiance, that is, the irradiation for which the growth rate is maximized ($W\,m^{-2}$ or $mol_{photons}\,m^{-2}\,s^{-1}$).

In 2012, Bernard and Rémond produced another explicit reparameterization of Haldane's model for their modeling [96]:

$$\mu = \mu_{\max}\frac{\mathrm{I}}{\mathrm{I} + \frac{\mu_{\max}}{\alpha}\left(\frac{\mathrm{I}}{\mathrm{I_{opt}}} - 1\right)^2} \tag{37}$$

with α being a shape factor ($m^2\ W^{-1}\ s^{-1}$).

Equations 36 and 37 are functionally equivalent; however, Equation 37 is easier to model since α must always be a positive number, whereas β can also be a number between -1 and 0.

The conversion between the parameters of all variations of the Haldane model is found in Table 3.

Table 3: Conversion between different parameterizations of the Haldane model.

Convert to→	Haldane ((34)	Eilers and	Eilers and	Bernard & Rémond

↧Convert from		Peeters 1 ((35)	Peeters 2 (36)	(37)
Haldane ((34)	–	$c = \frac{K_S}{K_A}$ $b = \frac{1}{K_A}$ $a = \frac{1}{K_A K_I}$	$\mu_{max} = \frac{K_A}{1 + 2\sqrt{K_S/K_I}}$ $\beta = \frac{1}{2\sqrt{K_S/K_I}}$ $I_{opt} = \sqrt{K_S K_I}$	$\mu_{max} = \frac{K_A}{1 + 2\sqrt{K_S/K_I}}$ $\alpha = \frac{K_A}{K_S}$ $I_{opt} = \sqrt{K_S K_I}$
Eilers and Peeters 1 ((35)	$K_A = \frac{1}{b}$ $K_S = \frac{c}{b}$ $K_I = \frac{b}{a}$	–	$\mu_{max} = \frac{1}{b + 2\sqrt{ac}}$ $\beta = \frac{b}{2\sqrt{ac}}$ $I_{opt} = \sqrt{c/a}$	$\mu_{max} = \frac{1}{b + 2\sqrt{ac}}$ $\alpha = \frac{1}{c}$ $I_{opt} = \sqrt{c/a}$
Eilers and Peeters 2 (36)	$K_A = \mu_{max}\left(\frac{\beta + 1}{\beta}\right)$ $K_S = \frac{I_{opt}}{2\beta}$ $K_I = 2\beta I_{opt}$	$c = \frac{I_{opt}}{2d}$ $b = \frac{\beta}{d}$ $a = \frac{1}{2 I_{opt} d}$ $d = \mu_{max}(1 + \beta)$	–	$\mu_{max} = \mu_{max}$ $\alpha = \frac{(\beta + 1) \cdot 2\mu_{max}}{I_{opt}}$ $I_{opt} = I_{opt}$
Bernard & Rémond (37)	$K_A = I_{opt}\alpha\delta$ $K_S = I_{opt}\delta$ $K_I = \frac{I_{opt}}{\delta}$ $\delta = \frac{\mu_{max}}{\alpha I_{opt} - 2\mu_{max}}$	$c = \frac{1}{\alpha}$ $b = \frac{1}{\mu_{max}} + \frac{2}{\alpha I_{opt}}$ $a = \frac{1}{\alpha I_{opt}^2}$	$\mu_{max} = \mu_{max}$ $\beta = \frac{\alpha I_{opt}}{2\mu_{max}} - 1$ $I_{opt} = I_{opt}$	–

In 1986, Lee et al. simplified the Haldane model, reducing it to just two variables [73], shown in Equation (38.

$$\mu = \frac{I}{K_1 + K_2 I^2} \tag{38}$$

with K_1 (J m^2 or mol$_{photons}$ m^{-2}) and K_2 (m^2 J^{-1} s^2 or m^2 s^2 mol$_{photons}^{-1}$) being constants. By deriving this equation, μ_{max} (the maximum point of the function) and I_{opt} (the value of irradiance for which the growth rate is maximized) can be obtained. These values are shown in Equations (39 and (40, respectively.

$$I_{opt} = \sqrt{K_2/K_1} \tag{39}$$

$$\mu_{max} = \frac{\sqrt{K_1/K_2}}{2K_1} \tag{40}$$

Mathematically, Haldane's model can be simplified to Lee's model (by keeping μ_{max} and I_{opt} the same between both models) when the value of the constant β from Eilers and Peeters' model is 0, and when the value of α from Bernard and Rémond's model is $2\mu_{max}/I_{opt}$. This can be helpful when modeling data because it allows the elimination of one variable in these specific scenarios.

As an alternative to Lee's model, an explicit version is found in Equation (41.

$$\mu(I) = \mu_{max} \frac{2 I_{opt} I}{{I_{opt}}^2 + I^2} \quad (41)$$

2.3.1.2.3 Other Models

The following are models that do not fit in any of the previously defined families.

The exponential model (also called the Poisson model, Equation (42) was first proposed by van Oorschot in 1955.

$$\mu(I) = \mu_{max} \left(1 - exp\left(-\frac{I}{\lambda}\right)\right) \quad (42)$$

where λ (also called I_{max} in some publications, W m^{-2} or $mol_{photons}$ m^{-2} s^{-1}, which is a misleading name since this value does not correspond to a maximum of the function) is the value of *I* for which $\mu = 1 - {}^{1}/_{e}\,\mu_{max} \approx 0.6321\mu_{max}$.

The hyperbolic model (Equation (43) was proposed by Moser in 1985 for batch fermentation kinetics [105] and applied to microalgae by Grima et al. [81].

$$\mu(I) = \mu_{max} \frac{I^n}{I^n + K_S^n} \quad (43)$$

where *n* is a constant (dimensionless). This model was further modified by Costache et al. (Equation (44) by changing the inhibition term to be dependent on the exponential of the light intensity [87].

$$\mu(I) = K_A \frac{I^n}{I^n + K_S\, exp(mI)} \quad (44)$$

where *m* is a constant ($mol_{photons}^{-1}$ m^2 s or W^{-1} m^2).

The log model (Equation (45) was proposed by Rabe and Benoit based on correlations of the author's own experiments [84].

$$\mu(I) = A \cdot log_{10}(I) + B \cdot log_{10}(X) - \lambda \quad (45)$$

where *A* and *B* are empiric model constants (h^{-1}).

The hyperbolic tangent model (Equation (46) was proposed by Chalker based on empirical data [86].

$$\mu(I) = \mu_{max}\, tanh(\alpha I) \quad (46)$$

where α is a constant (μmol^{-1} m^2 s or W^{-1} m^2)

Steele's Inhibition (Equation (47) is a model proposed by the eponymous author [98].

$$\mu(I) = \mu_{max} \frac{I}{I_{opt}} exp\left(1 - \frac{I}{I_{opt}}\right) \quad (47)$$

2.3.1.2.4 Model Comparison

Figure 7 contains a comparison between seven of the model families mentioned in this section: Monod, Bannister, Haldane (in the Eliers & Peeters's parametrization), Lee (which is the same as the Eliers & Peeters model with β=0), Exponential, Hyperbolic tangent, and Steele's Inhibition.

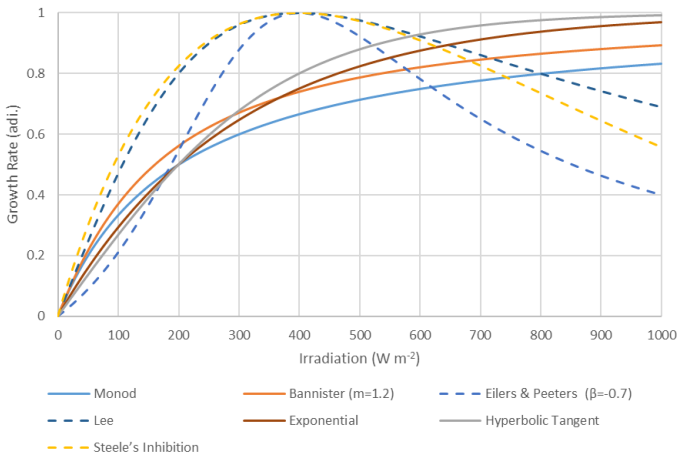

Figure 7: Comparison between seven different growth models. Solid lines represent models without inhibition, while dashed lines represent models with inhibition. The constants used were K_S = 100; m=1.2; β=-0.7; I_{opt}=400; λ=-K_S/ln(0.5)=144.3 and α=arctanh(1/2)/K_S=0.0055, which forces the Exponential and Hyperbolic Tangent models to have the same growth rate (0.5) as the Monod model for I=K_S. The value of μ_{max} is always equal to 1.

Of the models without attenuation, the Hyperbolic Tangent model grows the fastest, followed by the Exponential model, and finally the Monod model. The shape of the Bannister model's curve can be altered by changing the value of m. The Lee and Steele's Inhibition models grow essentially the same for values smaller than I_{opt}, but for higher values, the Lee model decays slower. The Haldane model's shape factor can be altered to change the curve's shape; for values smaller than β=0, the curve "pinches" around the value of I_{opt}: for values higher than 0, the curve bulges, growing faster and decaying slower.

2.3.1.3 Models Based on Average Light Intensity (Type I-B)

In a subtype of Type I models, which will be referred to as Type I-B, it is assumed that in a turbulent, well-mixed culture, all cells are exposed to a certain amount of average incident light I_{av} (W m^{-2} or $mol_{photons}$ m^{-2} s^{-1}) [67], which is itself a function of the incident light at the surface of the reactor. On average, cells are assumed to receive equal amounts of light [58].

$$I_{cell} = I_{av} = f(I_0) \tag{48}$$

This average light intensity can either replace the incident light intensity in models as shown in Table 2, or be used in a model in conjunction with I_0, for example, the following model by Molina Grima et al. [75].

$$\mu = \mu_{max} \frac{{I_{av}}^{n_{app}}}{{I_{av}}^{n_{app}} + K_{app}^{n_{app}}} \tag{49}$$

$$n_{app} = \frac{n_2}{I_0}$$

$$K_{app} = I_K + \left(\frac{I_0}{K_I}\right)^{n_1}$$

with K_{app} being the apparent light half-saturation constant (W m^{-2} or $mol_{photons}$ m^{-2} s^{-1}), n_{app} the apparent shape factor, K_I the light half-saturation constant (W m^{-2} or $mol_{photons}$ m^{-2} s^{-1}) and I_K (W m^{-2} or $mol_{photons}$ m^{-2} s^{-1}), n_1, (dimensionless) and n_2 (W m^{-2} or $mol_{photons}$ m^{-2} s^{-1}) being model constants. The rationale behind this equation is that photoinhibition is caused only by the light at the reactor surface, and it is not likely to happen deep in the culture, where light intensity is much lower.

Any model more complex than those of Type I-A, which includes the calculation of the average light intensity (I_{av}), requires knowing the light attenuation inside a reactor. That can be determined using a light distribution equation, which will be discussed in the next section.

Krischen et al. constructed a sophisticated model that does not consider the attenuation of light inside a reactor using the Lambert-Beer law, but instead determines the attenuation depending only on the biomass and a global constant that could be determined for each reactor configuration; this model also considers the effect of photoinhibition and photo-limitation The authors reported good agreement with their data, although their experiments were limited to the laboratory scale [106].

2.3.1.4 Models Based on Local Light Levels (Type II)

Type II models consider that the light levels within the reactor are different in different parts of the broth, thus making use of functions that relate the light reaching cells (I_{cell}) at a specific position with the distance *z* (m) of the cell to the surface of the system.

$$I_{cell}(z) = I_0 f(z) \qquad (50)$$

Unlike Type I-B models, which calculate the average light intensity and use that value in general growth equations, Type II models calculate the local growth rate over every differential volume of the reactor. The overall specific growth rate is calculated by integrating the local growth rate over the entire reactor.

Type II models are typical used in open pond systems, since the longer light paths and lower turbulence promotes the creation of light gradients [107], whereas in closed photobioreactors, due to their higher mixing rates, Type I-B models are often accurate enough [108]. Apart from their extra complexity, another downside of Type II models is that they still do not consider the flashing-light effect on the cells themselves, thus may result in overestimating the effects of light inhibition [9].

The critical factor in the utilization of Type II models is the determination of the path length inside a reactor. The calculations are relatively simple for vertical flat-panel reactors, as shown by Slegers et al. [12], but are more complex for tubular reactors due to their geometry. Fernández et al. [108] proposed a model to determine the path length inside a tubular reactor. The authors constructed a model specifically for the case of reactor tubes emersed in a pool of water and integrated the effect of refraction of the solar rays passing through different mediums (from air to water) using Snell's Law. The authors utilized several geometric considerations to calculate the angle of incidence of the solar rays, deriving an equation dependent on the solar position, the point inside the reactor, and the angle of incidence. However, an approximation of this angle can only be determined by iteration of an equation, which makes it unwieldy and laborious to calculate for all points inside the reactor. Furthermore, the authors did not specify the orientation of the reactor, which makes this model not appliable to any reactor.

2.3.1.5 Models Based on the Cellular "Light Story" (Type III)

Type III models consider that the rate of photosynthesis depends on the "light story" of the cell, that is, the locations inside the reactor that the individual cells pass through.

The light story of the cells depends on the fluid dynamics inside the reactor. The two basic approaches to model this dynamic are by judgment, essentially "guessing" how the flow inside the reactor occurs and dividing the reactor into areas with different flow types or by calculating the flow inside the reactor using computational fluid dynamics (CFD). CFD is a more fundamental approach, but some judgment is still required in selecting its internal turbulence models [9].

After the light story of the cells is determined, the rate of photosynthesis (and thus the specific growth rate) is then calculated using a dynamic biological model. Most approaches focus on the photosynthetic units (PSUs), modeling them using a three-population model as presented by Elliers and Peeters [104]. A representation of the three population models is described in Figure 8.

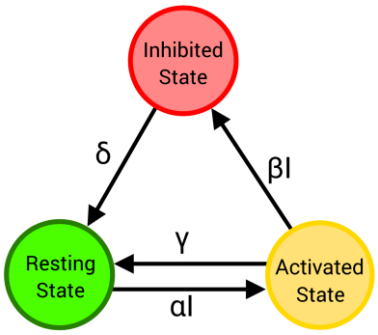

Figure 8: Diagram of the three-population model showing the resting, excited, and inhibited states of PSUs. *α* through *δ* represents the rate of change from one state to another. *I* represents the incident light on the PSU. The rate of photosynthesis is usually assumed to be proportional to *αI*. Based on the diagram in [9]; constants from [104].

This model assumes that the PSUs can be in one of three states: rested, activated and inhibited. Photosynthesis is modeled as a two-step process where PSUs must absorb enough energy in their rested state (at a rate equal to αI) until the activated PSUs produce ATP and NADPH, then return to the resting state (at a rate γ). The activated PSUs can also transition to the inhibited state if hit by too many photons (at a rate equal to βI), unable to process further photons until damaged key proteins are recovered (at a rate δ).

Mathematically, this can be written as the following set of equations [104]:

$$\begin{cases} P_{activated} + P_{rested} + P_{inhibited} = 1 \\ \frac{d_{P_{rested}}}{dt} = -\alpha I P_{rested} + \gamma P_{activated} + \delta P_{inhibited} \\ \frac{d_{P_{activated}}}{dt} = \alpha I P_{rested} - (\beta I + \gamma) P_{activated} \\ \frac{d_{P_{inhibited}}}{dt} = \beta I P_{activated} - \delta P_{inhibited} \end{cases} \quad (51)$$

Elliers and Peeters demonstrated that a steady-state simplification of this model results in the same expression as Equation (29.

Camacho Rubio et al. [39] developed a dynamic, mechanistic model of photosynthesis that integrates the main light-dependent physiological responses, such as photoadaptation, photoinhibition, and the flashing-light effect, into one unified mathematical framework. This model was subsequently updated by García-Camacho, et al. [109] to include the effects of PSUs. It was designed to overcome the limitations of previous empirical and semi-mechanistic photosynthesis, which could not accurately describe photosynthetic responses under fluctuating light conditions typical of photobioreactors or natural environments. The model quantitatively fits published experimental data for *Chlorella pyrenoidosa*, *Phaeodactylum tricornutum*, and others under steady light, flashing light, and diurnal light variations. The authors report that such dynamic models may be more adequate in scenarios where there are unsteady light conditions, such as those found in outdoor cultivations [70].

Laifa et al. used Elliers and Peeters' approach to model a tubular reactor exposed to direct sunlight, constructing a model of the attenuation of light inside the reactor (considering absorption and scattering by the cells and reflection and refraction by the reactor walls) dependent on the sun's location, including the calculation of the path length inside the reactor, then applying CFD and Monte Carlo simulations to determine the random movement of the cell particles inside the reactor to construct their "light story" [110]. This approach revealed that the biomass concentration has little effect on the actual overall growth rate of the reactor and that it is entirely dependent on the reactor turbulence, that is, the capacity of the reactor to move cells between the light and dark zones of the reactor.

Solimeno et al. also used the PSU approach in their mechanistic model, assuming the rate of photosynthesis is proportional to αI, as well as a factor depending on the concentration of oxygen in the medium. The authors reported good agreement with the experimental data [111].

2.3.2 Other Factors Affecting Microalgae Growth

Since microalgae are living organisms, their growth depends on more than just light. The considered factors are temperature, nutrients, pH and carbon, and endogenous respiration.

Extending the nomenclature used by Béchet et al. for the effects of temperature [9], these various factors can be integrated together in two different ways. Coupled models try to account for the potential interdependence between photosynthesis and these other factors, meaning one factor may affect the parameters of other factors. Uncoupled models simply assume that each factor has its own equation and its own parameters that do not depend on other factors; all the different equations for each factor are then combined into one single equation for the entire growth rate using some method (as described later in the next section).

In this section, uncoupled models will be presented, with coupled models being presented in Section 2.3.3.

2.3.2.1 Combining uncoupled models

Uncoupled models assume there are distinct equations for each factor. These are then combined into a single equation using some method, and finally, a global maximum growth rate μ_{max} is assigned to the entire equation. This is expressed in Equation (52.

$$\mu = \mu_{max} \cdot f(\mu_1, \mu_2, \mu_3, \cdots) \tag{52}$$

where μ_1, μ_2, ..., represent the equations for individual factors μ_1, μ_2, and so on.

Haefner proposed four methods to combine these parameters [112].

Leibig's law of the minimum (also known as the threshold method) assumes that growth is always limited by the most limiting parameter, that is:

$$\mu = \mu_{max}\, min(\mu_1, \mu_2, \mu_3, \cdots) \tag{53}$$

Multiplication assumes that all parameters affect the growth at the same time and that multiple limitations deteriorate the growth even further:

$$\mu = \mu_{max} \cdot \prod_{i=1}^{N_f} \mu_i = \mu_{max} \cdot \mu_1 \cdot \mu_1 \cdot \mu_3 \cdot \cdots \tag{54}$$

with N_f being the number of factors being considered.

The third method assumes the average of the functions:

$$\mu = \mu_{max} \frac{\sum_{i=1}^{N_f} \mu_i}{N_f} = \mu_{max} \frac{\mu_1 + \mu_2 + \mu_3 + \cdots}{N_f} \quad (55)$$

The fourth method is referred to as mean resistance:

$$\mu = \frac{\mu_{max}}{\sum_{i=1}^{N_f} \frac{1}{\mu_i}} = \frac{\mu_{max}}{\frac{1}{\mu_1} + \frac{1}{\mu_2} + \frac{1}{\mu_3} + \cdots} \quad (56)$$

The vast majority of models in the literature use the multiplicative method, followed by the threshold method [113].

2.3.2.2 Temperature

The temperature of the culture is a major factor affecting the growth of microalgae since it affects both the rate of enzymatic reactions as well as the solubility of gases like O_2 and CO_2 [27, 32]. In outdoor microalgae cultures, temperature is usually controlled by cooling the culture with a cooling serpentine or passive cooling with water evaporation. However, it ultimately depends on the outside temperature, which, of course, depends on the local climate of the location of the reactor.

Pessi et al. [32] provided an auto-regressive model to predict the temperature of the water in a raceway reactor based on the external air temperature, both outside (Equation (58) and inside a greenhouse (Equation (57).

$$T_{w_{in}} = aT_{ext}(t-3) + bT_{ext}(t) + cI_o(t-1) + dT_{w_{in}}(t-1) + T_0 \quad (57)$$

$$T_{w_{out}} = aT_{ext}(t-4) + bT_{ext}(t) + cI_o(t) + dT_{w_{out}}(t-1) \quad (58)$$

with $T_{w\text{-}in}$ and $T_{w\text{-}out}$ being the temperature inside and outside the greenhouse (degrees Celsius); T_{ext} being the ambient air temperature (degrees Celsius); T_0 being a temperature constant (degrees Celsius); *a, b, c* and *d* being multiplication factors; and *t* being the time (in hours). These equations were made for raceway reactors, but they could be applicable to closed reactors with a recalibration of the factors.

The temperature model is usually based on similar models for bacterial growth. In the following equations, the term dependent on the temperature is μ_T.

The most widely used and successful temperature model is the cardinal temperatures model with inflection (CTMI). This was first published by Rosso et al. [114], who modified a previously published model [115]. This model uses the concept of cardinal temperatures, that is, the maximum, minimum, and optimal temperatures for growth explicitly expressed in the model, as shown in Equation (59.

$$\mu_T = \begin{cases} \mu_{max} \dfrac{(T - T_{max})(T - T_{min})^2}{(T_{opt} - T_{min})(a(T) - b(T))}, & T \leq T_{min} \vee \ T \geq T_{max} \\ 0, & T_{min} > T > T_{max} \end{cases} \quad (59)$$

$$a(T) = (T_{opt} - T_{min})(T - T_{opt}), b(T) = (T - T_{opt})(T_{opt} + T_{opt} - 2T)$$

where T_{max}, $T_{opt,}$ and T_{min} (°C) are the maximum, optimal, and minimum cardinal temperatures for growth for that specific organism, respectively. Growth only occurs between T_{min} and T_{max} (the function has a positive value) and is maximized for T_{opt}.

Another model proposed by Rosso et al., [114] is known as the Hinshelwood model, modeled after the Arrhenius function, used to predict the impact of temperature on chemical reactions.

$$\mu_T = A_1 \exp\left(-\frac{B_1}{T}\right) - A_2 \exp\left(-\frac{B_2}{T}\right) \quad (60)$$

Where B_1 and B_2 (°C) are model constants (that can be viewed as the activation energies divided by the gas constant found in the original Arrhenius function), T is the temperature (°C), and A_1 and A_2 (s^{-1}) are pre-exponential factors. In this equation, the first term can be interpreted as the production rate and the second term as the consumption rate of microorganisms due to high temperatures [58]. However, in this equation, as the temperature is decreased, the growth rate never reaches zero except at absolute zero, making it unrealistic at low temperatures [58].

Ratkowsky et al. [116] proposed an empirical equation relating the square root of the growth rate to temperature.

$$\sqrt{\mu_T} = b(T - T_{min}) \quad (61)$$

where T_{min} (°C) is the temperature below which no growth occurs, and b (°C $s^{-0.5}$) is a model constant. This equation, however, didn't predict the negative effect that high temperatures have on the growth rate, so the same authors later suggested a refinement of the model to take this effect into account [117].

$$\sqrt{\mu_T} = b(T - T_{min})(1 - \exp(c \times (T - T_{max}))) \quad (62)$$

where T_{max} (°C) is the maximum temperature limit for growth and c ($°C^{-1}$) is a model constant.

Roels modeled the rate of deactivation of enzymes in photosynthetic organisms [118] as:

$$\mu_T = \frac{\exp\left(-\frac{E_a}{kT}\right)}{1 + K \times \exp\left(-\frac{E'_a}{kT}\right)} \quad (63)$$

where E_a and E'_a (J) are the activation energies for photosynthesis and enzyme denaturation, respectively, k is the Boltzmann constant (J K^{-1}), and K is a dimensionless constant.

2.3.2.3 Nutrients

The limitation of different nutrients can significantly affect microalgae growth, specifically if it is an intended effect to cause the induction of a specific metabolite. Models to account for the effects of nutrients on the growth of photoautotrophic microalgae are similar to those used to explain heterotrophic growth. A summary of some of these models can be found in Table 4. The growth rate term dependent on nutrients is hereby referred to as μ_N.

Table 4: Assorted collection of nutrient models from the literature.

Model	Source	Formula	System Size	System	Species
Monod	[119]	$\mu_N = \frac{S}{K_{sub} + S}$ (64)	Unknown (Lake)	Outdoor	Diatoms *Chrysophycea sp.* *Cyanobacteria sp.*
	[120]		100 mL	Indoor (55–60 $\mu mol_{photons}\ m^{-2}\ s^{-1}$, 14:10 light/dark ratio)	*Scnesdesmus sp.*
	[121]		21 L [122]	Indoor	*Spirulina platensis*
	[123]		2.2 L	Indoor (cool lamps, 17.5 klx)	*Dunaliella tertiolecta*
	[124]		100 mL	Indoor (2500 lx, 12 h:12 of light/dark ratio)	*Micrpcystis tricornutum*
Monod with inhibition (Andrews' model)	[103]	$\mu_N = \frac{S}{K_{sub} + S + \frac{S^2}{K_I}}$ (65)	Theoretical		-
	[125]		700 mL	Indoor	*Chlamydomonas reinhardtii*
	[126]		250 mL	Indoor	*Chlorella kessleri*
Fré et al.	[123]	$\mu_N = \left(\frac{S}{K_S + S}\right)\left(\frac{K_X}{X + K_X}\right)$ (66)	2.2 L	Indoor (cool lamps, 17.5 klx)	*Dunaliella tertiolecta*
Droop/ Cell quota model	[127]	$\mu_N = \left(1 - \frac{Q_{min}}{Q}\right)$ (67)	1 L	Indoor (fluorescent Lights, 85 $\mu mol_{photons}\ m^{-2}\ s^{-1}$)	*Monochrysis lutheri*
	[128]		1 L	Indoor	*Pseudochlorococcum sp.*
	[123]		2.2 L	Indoor (cool lamps, 17.5 klx)	*Dunaliella tertiolecta*
Geider	[129]	$\mu_N = \left(\frac{Q - Q_{min}}{Q_{max} - Q_{min}}\right)$ (68)	Various	Indoor	*Thalassiosira psedonana* *Pavlova lutheri* *Skeletonema costatum* *Isochrysis galbana*
Caperon and Mayer	[130]	$\mu_N = \left(\frac{Q - Q_{min}}{K_C + Q - Q_{min}}\right)$ (69)	5 L	Indoor (fluorescent lamps)	*Coccochloris stagnina* *Cyclotella nana.* *Dunaliella tertiolecta*
Bougaran et al.	[131]	$\mu_N = \frac{1 - \frac{Q_{min}}{Q}}{1 - \frac{Q_{min}}{Q_{max}}}$ (70)	2 L	Indoor (continuous light, 130 $\mu mol_{photons}\ m^{-2}\ s^{-1}$	*Selenastrum minutum* *Isochrysis affinis galbana*

2.3.2.4 pH and carbon

In modelling the effect of pH and carbon on the growth rate of the culture, their effects are often considered together since carbon dioxide is used to lower the pH of the culture. Thus, only the modelling of one of them is considered. A common approach is to use the same models for nutrients applied to carbon. In this chapter, the growth rate dependent on the carbon concentration is denoted as μ_C.

Goldman et al. used the Monod model (Equation (64) to relate the specific growth rate of a culture of *Scenedesmus quadricauda* and *Selenastrum capricornutum* to the total inorganic carbon in the culture, which is the sum of carbonic acid, bicarbonate, carbonate and aqueous carbon dioxide [132].

Lee and Zhang also used aqueous carbon dioxide in a Monod model for the growth of *Chlorella sp*. when the concentration of carbon dioxide was measured below 50 mg/L [133]. The authors used the Monod model with inhibition (Equation (65) at higher concentrations to include the inhibitory effect caused by low pH.

Filali et al. considered all types of inorganic carbon in their model (Equation (71), which can be calculated using equilibrium constants and the pH of the culture [134]:

$$\mu_C = \mu_{max} \frac{[TIC]}{X \cdot K_{CL} + [TIC]} \tag{71}$$

where *TIC* is the molar concentration of the total inorganic carbon, *X* is the biomass concentration, and K_{CL} is the carbon saturation constant (mol/$g_{biomass}$). The amount of carbon dioxide in the culture can be calculated using mass transfer equations.

Another approach is to use the pH directly as a variable in the model. Bailey and Ollis proposed a model for the effect of pH on the reaction rate of enzymes [135], which was later used by other authors [136, 137] for the growth of bacteria:

$$\mu_C = \frac{1}{1 + \frac{[H^+]}{K_H} + \frac{K_{OH}}{[H^+]}} \tag{72}$$

where K_H and K_{OH} are model parameters are $[H^+]$ is the concentration of hydrogen ions, which can be calculated from pH.

Jayaraman and Rhinehart included pH as a parameter in their model and assumed that only carbon dioxide affects pH changes; therefore, the authors described the effect of carbon as a function of pH [138]:

$$\mu_C = \frac{1}{1 + exp\ (\lambda \cdot (pH - pH_{opt}))} \quad (73)$$

where pH_{opt} is the pH at which the growth is maximized, and λ is a model constant.

Costache et al. used a model based on an Arrhenius-like equation to describe the effect of pH on the photosynthesis rate of *Scendesmus almeriensis* [87]:

$$P = P_{max}\left(B_1\ exp\left(-\frac{C_1}{pH}\right) - B_2\ exp\left(-\frac{C_2}{pH}\right)\right) \quad (74)$$

where B_1, B_2, C_1 and C_2 are model constants and P and P_{max} are the photosynthesis rate and its maximum value, respectively.

2.3.2.5 Oxygen concentration

Oxygen accumulation in the medium is a well-understood major issue in microalgae growth, due to its effect in limiting photosynthesis rates, but few attempts have been made to quantify this effect [58].

Miyachi et al. proposed a second-order equation for the degree of inhibition H caused by oxygen concentration [139].

$$H = 1 - \frac{P}{P_{max}} = \frac{[O_2]^2}{[K_O]^2 - [O_2]^2} \quad (75)$$

where K_O is model constant (Pa), P is photosynthesis rate (h^{-1}), P_{max} (h^{-1}) is photosynthesis rate at the absence of oxygen, and $[O_2]$ is oxygen partial pressure in the gas phase (Pa).

Fernández et al., used a first order equation [70] to relate oxygen concentration to photosynthesis rate.

$$P = P_{max}\left(\frac{K_O}{K_O + [O_2]}\right) \quad (76)$$

Costache et al. related the photosynthesis rate to the rate of oxygen generation [87]:

$$P = P_{max}\left(1 - \left(\frac{[O_2]}{K_{O_2}}\right)^m\right) \quad (77)$$

where K_O and m (adi.) are model constants.

Concas et al. used a linear function to describe the inhibitory effect of oxygen [92]

$$\mu = \mu_{max}\left(1 - \frac{[O_2]}{[O_2]_{max}}\right) \quad (78)$$

where $[O_2]_{max}$ is oxygen concentration at which growth becomes zero.

2.3.2.6 Endogenous respiration

Endogenous respiration occurs both during the day and night, but during the day, it can be assumed to be directly correlated with the rate of growth due to photosynthesis, and as such, is already integrated into the growth model [9].

However, endogenous respiration during the night can be a much more important factor since, unlike with heterotrophic growth, light (which directly impacts the absorption of carbon) is not readily available at night during outdoor cultivation. As such, loss of biomass can occur during the night unless an artificial light source is used constantly.

The rate of endogenous respiration during both day and night R_N (g s^{-1} m^{-3}) can be modeled with first-order kinetics.

$$R_N = -\alpha X \tag{79}$$

with α (s^{-1}) as a constant and X as the biomass concentration. However, this equation does not consider the effect of temperature difference during the night. One possibility is to use an Arrhenius-like equation, as proposed by Alikhani et al. for methanol-fed denitrifying bacteria [140]:

$$R_N = -R_N\left(T_{ref}\right)\theta^{(T-T_{ref})}X \tag{80}$$

where $R_N(T_{ref})$ is the endogenous respiration rate at the reference temperature T_{ref}, and θ a constant. The authors expected a number around 1.1 for the value of θ.

Both approaches consider endogenous respiration as a constant parameter that can be seen as “negative growth”. Therefore, it is not subject to the proposed methods for combining other factors as expressed in Section 2.3.2.1, being merely added to the end of the growth equation, as expressed in Equation (81.

$$\mu = \mu_{max} \cdot f(\mu_1, \mu_2, \mu_3, \cdots) + R_N \tag{81}$$

2.3.3 Coupled Models

The following are some coupled models found in the literature, with interrelated effects of various parameters (like irradiation, temperature, oxygen, etc.).

A model proposed by Demound et al. (Equation (82) modifies Equation (28 so that all parameters are dependent on the temperature [141].

$$\mu = 2\mu_{max}(T)\left(1 + 2\beta_i(T)\right)\frac{i}{i + 2\beta_i(T) + i^2}, i = \frac{I}{I_{opt}(T)} \tag{82}$$

where μ_{max} (s^{-1}) is the maximum specific growth rate, β_i is a dimensionless constant, I is the light intensity, and I_{opt} is the optimum light intensity for photosynthesis at the temperature T, with $\mu_{max}(T)$, $\beta_i(T)$ e $I_{opt}(T)$ either as constants or in the form:

$$\gamma(T) = \gamma_m \left(\frac{T}{T_{opt}} w^u \right)^{\alpha}, w = \frac{T - T_0}{T_{opt} - T_0}, u = \frac{T_0 - T_{opt}}{T_{opt}} \quad (83)$$

Although coupled models might better represent the combined impact of the temperature and radiation intensity, when compared to uncoupled models, the limiting step of photosynthesis may not always be temperature-dependent [9]. In addition, the large number of parameters necessary to fit the experimental data leads to practical problems associated with overfitting, where the apparent accuracy of the prediction is due to the fitting to random noise and not an underlying trend [9].

Muñoz and Bernard created a model combining the effects of light, temperature, and the rarely addressed effect of oxygen concentration [142]. The authors' LOT model uses a Haldane model (Equation 24) for the effect of light and a modified Hinshelwood's model (Equation (60) for the effect of temperature, which includes the effect of oxidative stress. Because this model is hard to calibrate due to its sensitivity, the CTMI (Equation (59) was first calibrated using real data, and then the Hinshelwood model was calibrated using the "virtual" dataset created by the CTMI model. The authors reported a very good fit to the data, with the effect of oxygen being found to greatly affect microalgae growth.

Nikolaou et al. produced a model based on mass balance equations for the biomass, nutrient (inorganic nitrogen) and nutrient quota [143]. The effect of the nutrient on the growth rate is modeled using Droop's model, while the effect of light on growth is modeled by determining the content of chlorophyll in the cell, as well as using PSU theory. In this way, the authors' model can model photosynthesis in both a short time scale (using PSUs) and a long timescale (using the chlorophyll content). The authors reported encouraging results when applying their model to literature data for *Skeletonema costatum* and *Dunaliella tertiolecta*.

3 Modeling Existing Cultivations on Pilot-scale Tubular Reactors

In collaboration with A4F, the data from ten cultivations of *Nannochloropsis* sp., performed at its Lisbon Experimental Unit in Portugal over the years 2015 to 2020, were modeled using semi-empirical models from the literature.

3.1 Materials and Methods

3.1.1 Bioreactor Configurations and Assays

Cultivations were done in three different bioreactor configurations, named U1, U2, and M1. The U1 and U2 reactors were unilayer horizontal tubular photobioreactors (UHT-PBR), with the U1 reactor having 8 lines of tubes and the U2 reactor with 16 lines of tubes; they were exposed directly to sunlight. The M1 reactor was a multilayer horizontal tubular photobioreactor (MHT-PBR) with 24 lines of tubes stacked in two columns of 12 lines of tubes each; it was placed inside a greenhouse and thus was not exposed directly to sunlight. A photograph of the three reactor types can be found in Figure 9.

(**a**)

(**b**)

(**c**)

Figure 9. Photographs of the reactors used in this article. (a) U1 reactor; (b) U2 reactor; (c) M1 reactor.

All reactors had a cooling system that was activated whenever the internal temperature reached more than 30 °C to maintain that temperature or lower; this was achieved using a serpentine immersed in the air exchange chamber. *Nannochloropsis* sp. was cultivated using A4F artificial saltwater industrial medium (modified ESAW [9] with salinity ranging from 30 to 35 g/L and containing nitrogen, phosphorus, and other essential micronutrients). The reactors were run in a batch regime, with nutrients added as needed. Partial harvesting of the reactor contents (renovations) was done occasionally over the course of each assay. Only solar irradiance and non-limiting nutrient conditions were used for all assays. For all cultures, the pH was maintained at 8.0 through on-demand injection of pure CO_2. The viability of the cultures and absence of contamination were checked via microscopic observation of samples of the reactor medium.

There are ten assays, named arbitrarily with the reactor type they were cultivated in and a number (for example, U1-1, U2-2, and M1-3). They were divided into two groups with five elements

each: the assays used to fit the models (the training assays), and the assays used to test the models (the validation assays).

Each assay was assigned to the training or validation group based on the following criteria:

- Having the same number of assays in each group.
- Having a balance of the number of multilayer and unilayer assays in each group.

The codes given for each of the assays, along with their duration, the number of data points collected in each, and whether they are a training assay or a validation assay, are presented in Table 5. In total, there were 251 data points that were distributed between the training (150 data points) and validation (101 data points) datasets.

Table 5. Assay codes used and duration of each assay.

Assay Code	Duration (Days)	Number of Data Points	Assay Type
M1-1	41	15	Validation
M1-2	95	38	Training
M1-3	19	17	Validation
M1-4	117	38	Training
U1-1	113	44	Training
U1-2	33	16	Training
U1-3	82	25	Validation
U2-1	113	42	Validation
U2-2	20	14	Training
U2-3	33	17	Validation

3.1.2 Measurements and Process Data

All reactors had the same parameter measurements and process data available: total culture volume (measured every day); harvest frequency and proportion, usually between 7 and 14 days and between 20 and 80% of the culture volume; dry cell weight, measured through optical density taken approximately twice per week; nitrogen concentration, measured approximately twice per week (using the APHA 2012 Section 4500 NO3-B method [9]); temperature of the reactor, recorded manually thrice per day at 9 am, 12 am, and 5 pm; and pH of the reactor, recorded manually thrice per day at 9 am, 12 am, and 5 pm. All these measurements were done with duplicates. The irradiation values used in the models were measured at the location of the reactors every 15 min by a weather station mounted on the site, allowing the consideration of variations in the weather conditions, such as overcast or cloudy days, which lowered the measured irradiation. Whenever irradiation data were unavailable, for example, due to data corruption, data were obtained from the Photovoltaic Geographical Information System (PVGIS) [10], which has measurements available every hour. The details for the determination of the dry cell weight through the optical density are explained in Appendix A.

3.1.3 Data Processing and Model Construction

For each assay, the laboratory records were combined with data from the on-site weather station or PVGIS to generate an hourly dataset containing the key parameters required for the models. All the models tested were constructed in MS Excel using the data described above. All the models tested shared the same global parameters for all the assays used in that model. The biomass and nutrient concentrations measured at the beginning were used to start the simulation at time 0.

The models were fitted to the ensemble of data in the training set using the Solver add-on by minimizing the sum of squared residuals (*SSR*—see Equation 84) of the dry cell weight by varying the growth model parameters:

$$SSR = \sum_{i=1}^{n} (y_i - y_i')^2 \tag{84}$$

where y_i is the measured dry cell weight, and y_i' is the calculated dry cell weight for that point in time.

Due to the short step used in the integration of the differential equations (1 h), the Euler method was considered adequately precise. The Runge–Kutta method of the 4th order was used to check the accuracy of the numerical integrations, but no appreciable difference was found between the two methods. Euler's method also presents the advantage of being significantly simpler to implement and providing faster optimization procedures.

3.1.3.1 Tested Models

The main part of all models is the growth rate (μ, h^{-1}) equation, which determines how light, nutrients, and the influence of the concentration of biomass affect the growth rate at any given step of the simulation. When a factor other than light was considered, the method used to balance the effects of all these influences was the multiplicative method, as proposed in Equation 54. Other recorded parameters, such as temperature and pH, were also considered, but their inclusion did not show any significant improvement in the models. Therefore, only light, nutrients, and biomass concentrations were considered for the modeling.

The tested light models for this section were of Type I-B, that is, it is assumed that the cultures were turbulent and well-mixed culture, meaning all cells are exposed to a certain amount of average incident light I_{av} (W m^{-2} or $mol_{photons}$ m^{-2} s^{-1}) [12], which is a function of the incident light at the surface of the reactor and some attenuation function *f* that depends on the concentration of the

biomass. The simplest and most used light attenuation function is the Beer–Lambert law (Equation 6), which will be used in this section.

Since the average light intensity inside a reactor is difficult to calculate, a simpler approach was taken, where the product of E_a and z is considered to be a single constant, which is termed α, or a Beer-Lambert-like constant (m g^{-1}). E_a is dependent on the specific species being considered, but it is considered a constant since the same species was used in all assays. Considering the photobioreactor tubes all have the same diameter and are oriented along the same cardinal directions, z is considered a constant that does not vary with the reactor type; z should vary with the position of the sun in the sky, which varies with the time of day and the day of the year, but it is assumed for these simple models that z is also a constant. Therefore, α is also a constant that will be a model parameter in all modeling approaches. It is assumed that all cells in the reactor are exposed to the same value as I_{eff}, that is, the culture is well-mixed enough to prevent stratification of the reactor volume, creating light and dark regions.

The final equation for the effect of light attenuation in the reactor is Equation 85.

$$I_{cell} = I_{av} = I_{eff} = I_0 \cdot exp(-\alpha X) \tag{85}$$

All models assume 1st order growth, that is:

$$\frac{dX}{dt} = \mu X - \delta^D \frac{V_{recirc} X}{V} \tag{86}$$

where V is the volume (m^3), V_{recirc} is the recirculated volume (in m^3), and δ^D is the Dirac delta.

Integrating this equation using Euler's method and considering the renovations, Equation 87 is derived.

$$X_{t+1} = X_t + h\mu X_t - \sum_{j}^{\dots} {\delta^K}_{t,j} \frac{V_{recirc} X}{V} \tag{87}$$

where h is the integration step in hours, V_{recirc} is the volume recirculated in the time period j (in m^3), δ^K is the Kronecker delta, t is a discrete variable with all the periods considered in the integration (in hours), and j is a discrete variable with all the periods where a renovation occurred (in hours).

Four models were considered: Model M, H, E, and D.

Model M uses a Monod-like equation for the effect of incident light (Equation 88).

$$\mu_I = \mu_{max} \frac{I_{eff}}{K_S + I_{eff}} \tag{88}$$

Model E is an exponential model (Equation 24). Since the value of λ in the equation as formulated is not intuitive, by changing the base of the exponent to 2, a new parameter can be introduced, λ_2, which is the value of I for which $\mu = 0.5\ \mu_{\max}$; that is, λ_2 is the value of I for which the growth rate is half the maximum growth rate. It can be thought of as analogous to K_S of the Monod model (although the shape of the curves is different). The final model, including I_{eff}, is shown in Equation 89.

$$\mu_I = \mu_{max}\left(1 - 2^{\left(-\frac{I_{eff}}{\lambda_2}\right)}\right) \tag{89}$$

The parameters adjusted are μ_{max}, λ_2, and α.

Model H has an additional parameter to capture potential light inhibition. It is based on the Haldane model family. It was found that the original Haldane model's parameters are arbitrary and do not represent physical constants, thus making it difficult to derive conclusions about the behavior of the culture. Both reparameterizations of the model by Eilers and Peeters, and Bernad and Rémond were found to be inadequate for fitting, with Eilers and Peeters' version having a potentially negative constant and Bernard and Rémond's model raising numerical problems when used to fit the experimental data. Thus, a new model reparameterization is hereby proposed in Equation 90.

$$\mu_I = \mu_{max}\frac{k}{k + \left(I_{eff} - I_{opt}\right)^2} \tag{90}$$
$$k = 2\gamma I_{eff} I_{opt}$$

with I_{opt} (W m^{-2}) being the value of irradiation for which the growth rate is maximized and γ a dimensionless shape factor. The derivation of this equation can be found in Appendix B. Mathematically, it can be shown that a value of γ equal to 1 reduces this model to that of Lee [73]. The parameters adjusted are μ_{max}, γ, I_{opt}, and α.

Model D introduces the influence of nutrients. It is based on the 2015 work of Nikolaou et al. [30]. This model is based on three differential equations to calculate the substrate (S, g_N m^{-3}), biomass concentration (X, g_C m^{-3}), and the carbon-specific nitrogen quota (Q, g_N g_C^{-1}).

Because of the different reactor layouts, the equations used are simplifications of the ones presented in the original paper. Since harvesting occurs in discrete intervals, there is no dilution term. Likewise, endogenous respiration was not considered in these models. Therefore, the differential equation for the biomass is identical to the one presented in Equation 6, and the remaining equations are simplified to the ones presented in Equation 91.

$$\begin{cases} \dfrac{dX}{dt} = \mu X \\ \dfrac{dS}{dt} = -\rho X \\ \dfrac{dQ}{dt} = \rho - \mu Q \end{cases} \tag{91}$$

where ρ is the nutrient uptake rate ($g_N\ g_C^{-1}\ h^{-1}$).

The growth rate was simplified when compared with the work of Nikolaou et al. It is a combination of the well-established Droop model [144] with a Monod-like influence for light, as shown in Model M:

$$\mu_I = \mu_{max} \frac{I_{eff}}{K_I + I_{eff}} \left(1 - \frac{Q_{min}}{Q}\right) \tag{92}$$

where Q_{min} is the minimum nitrogen quota that still allows for growth ($g_N\ g_C^{-1}$).

The nutrient uptake rate is the same as that used by Nikolaou et al. [30]:

$$\rho = \rho_{max} \frac{S}{K_{sub} + S} \left(1 - \frac{Q}{Q_I}\right) \tag{93}$$

where ρ_{max} ($g_N\ g_C^{-1}\ s^{-1}$) is the maximal nutrient uptake rate, K_{sub} ($g_N\ m^{-3}$) is the half-saturation constant for the nutrient, and Q_I ($g_N\ g_C^{-1}$) is the limit of the nitrogen uptake.

The fitting parameters are μ_{max}, K_I, Q_{min}, ρ_{max}, K_{sub}, Q_I, and α.

3.2 Comparison Metrics

To objectively compare the ability of the models to describe the experimental data, two objective metrics are used: the root mean squared error (RMSE) and the Akaike information criterion (AIC).

The RMSE is a regression evaluation method that considers the sum of squares and the number of data points, as well as the number of estimated parameters. The lower the RMSE, the better the fitting. The RMSE ($kg\ m^{-3}$) is calculated using Equation 94:

$$RMSE = \sqrt{\frac{\sum SSR}{n}} \tag{94}$$

where SSR is defined in Equation 84 and n is the total number of data points. The RMSE was calculated for both the training and validation datasets.

The calculation of the AIC follows the method presented by Burnham and Anderson [32]. The best model using this criterion is the one with the lowest value. Because the only important metric

to compare AICs is using their differences, the values calculated are given as ΔAIC (differences in AIC) using Equation 95:

$$\Delta AIC = 2k + n \cdot ln(\sigma^2) \tag{95}$$

where *k* is the number of parameters of the model, and σ^2 is the variance, which is calculated using Equation 96.

$$\sigma^2 = RMSE^2 \tag{96}$$

3.2.1 Bootstrapping

To obtain information about the precision with which the parameters are estimated, bootstrapping was used to calculate the average and standard deviation of each parameter in each model. The method used is the one described in [33].

The new objective function is defined as a weighted least-squares approach, as shown in Equation 97:

$$SSR = \sum_{i=1}^{n} w_i (y_i - f(y_i))^2 \tag{97}$$

where w_i is the weight assigned to each data point. For each data point in the training set, a weight of 0, 1, or 2 was randomly assigned, with a uniform distribution. The objective is to replace one-third of the data points from the original dataset with duplicates of points from the same dataset, thus preserving the total number of data points and the statistical characteristics of the error distribution in these points. The weight was multiplied by the squared error value for that data point, and the Solver add-on in MS Excel was run to minimize the modified error value. The Solver add-on was initialized with the parameter values equal to the original fitting (that is, with all the weights set to 1). This process was repeated 250 times for each model, using macros to allow the estimation of 250 values for the fitting parameters, which could then be statistically analyzed, and the average and standard deviations were computed.

3.3 Results & Discussion

3.3.1 Model Parameter Analysis

The parameters obtained for each model are as follows:

- **Model M:** $\mu_{max} = 0.041\ h^{-1}$; $K_S = 13.3\ MJ\ m^{-2}\ day^{-1}$; and $\alpha = 1.645\ m^3\ kg^{-1}$;
- **Model H:** $\mu_{max} = 0.032\ h^{-1}$; $I_{opt} = 41.4\ MJ\ m^{-2}\ day^{-1}$; $\gamma = 1.070$; and $\alpha = 1.337\ m^3\ kg^{-1}$;
- **Model E:** $\mu_{max} = 0.033\ h^{-1}$; $\lambda_2 = 9.933\ MJ\ m^{-2}\ day^{-1}$; and $\alpha = 1.515\ m^3\ kg^{-1}$;
- **Model D:** $\mu_{max} = 0.082\ h^{-1}$; $K_S = 63.3\ MJ\ m^{-2}\ day^{-1}$; $\alpha = 1.003\ m^3\ kg^{-1}$; $Q_{min} = 0.0025\ g_N\ g_C^{-1}$; $Q_{max} = 8 \times 10^{-6}\ g_N\ g_C^{-1}\ h^{-1}$; $K_{sub} = 0\ g_N\ g_C^{-1}$; and $Q_l = 3.98\ g_N\ g_C^{-1}$.

For Model H, the value of γ being approximately 1 implies that it is possible to simplify the model to that of Lee and eliminate one variable from the model without resulting in a significant loss of accuracy.

The values K_S from Model M and λ_2 from Model E are small and very close, which implies the culture achieved its maximum growth rate at low values of effective irradiation.

3.3.1.1 Maximum Growth Rate

Boussiba et al. reported a maximum growth rate of 0.030 h^{-1} for *Nannochloropsis salina* [8]. Van Wagenen et al. reported a maximum specific growth rate of 0.054 h^{-1} for this species, with the relationship between growth and light intensity adjusting well to a Monod-type equation [14]. Huesemann et al. also reported the same 0.054 h^{-1} value for *Nannochloropsis salina* using an unspecified growth model [34].

The specific growth rates for Models M, H, and E fall within the range given in the literature. However, the maximum growth rate for Model D is significantly above the other models. This could be explained by the method used to weigh the contributions of the different limiting factors for growth (namely, the irradiation intensity and the effect of nutrients), which multiplied both factors together. This means that their positive or negative effects are compounded. The actual maximum achieved growth rate, as produced by Model D, is between 0.0321 and 0.0505 h^{-1}, which is in line with the literature values.

3.3.1.2 Half-Saturation Constant for Light

Van Wagenen et al. reported a K_S of 37 µmol $m^{-2}\ s^{-1}$ [14] for *Nannochloropsis salina*. However, this value is not directly comparable to the K_S values calculated for the models presented in this work because the units are in moles of photons and not energy. It is, however, possible to convert

between the two values by considering the distribution of the wavelengths of light in the spectrum of sunlight. These calculations are explained in Appendix C. The calculated conversion factor is 0.2160 J μmol^{-1}. Using this value, the converted values for K_S are as follows:

- Model M: 61.6 $\mu mol\ m^{-2}\ s^{-1}$;
- Model D: 293 $\mu mol\ m^{-2}\ s^{-1}$.

As can be seen by these results, the K_S values obtained in the models are higher than the K_S reported for this species, and this value is higher for Model D than for Model M. A higher value of K_S means the culture's growth rate is lower for smaller irradiation values. The discrepancy between the values of K_S for Models M and D is due to the higher value of μ_{max} in Model D, which at low values of irradiation can account for the difference in the higher value of K_S. The difference in species might also account for a small discrepancy in the values of K_S.

3.3.1.3 Beer–Lambert-Like Constant

A Beer–Lambert-like constant was added to all models to account for the effect of light absorption in the cultures at higher concentrations. A value of 0 would imply no effect (the value of the exponential term would be 1); the higher this value, the more the effect of light attenuation inside the reactor. All models (except Model D) had this constant around 1.5 $m^3\ kg^{-1}$, which implies there is, in fact, attenuation of light inside the reactor, with this effect being more significant for higher concentrations of biomass.

3.3.2 Model Fitting Analysis

The results of the fittings of the four models being considered can be found in Figure 10. The values of the RMSE of each model and assay can be found in Table 6.

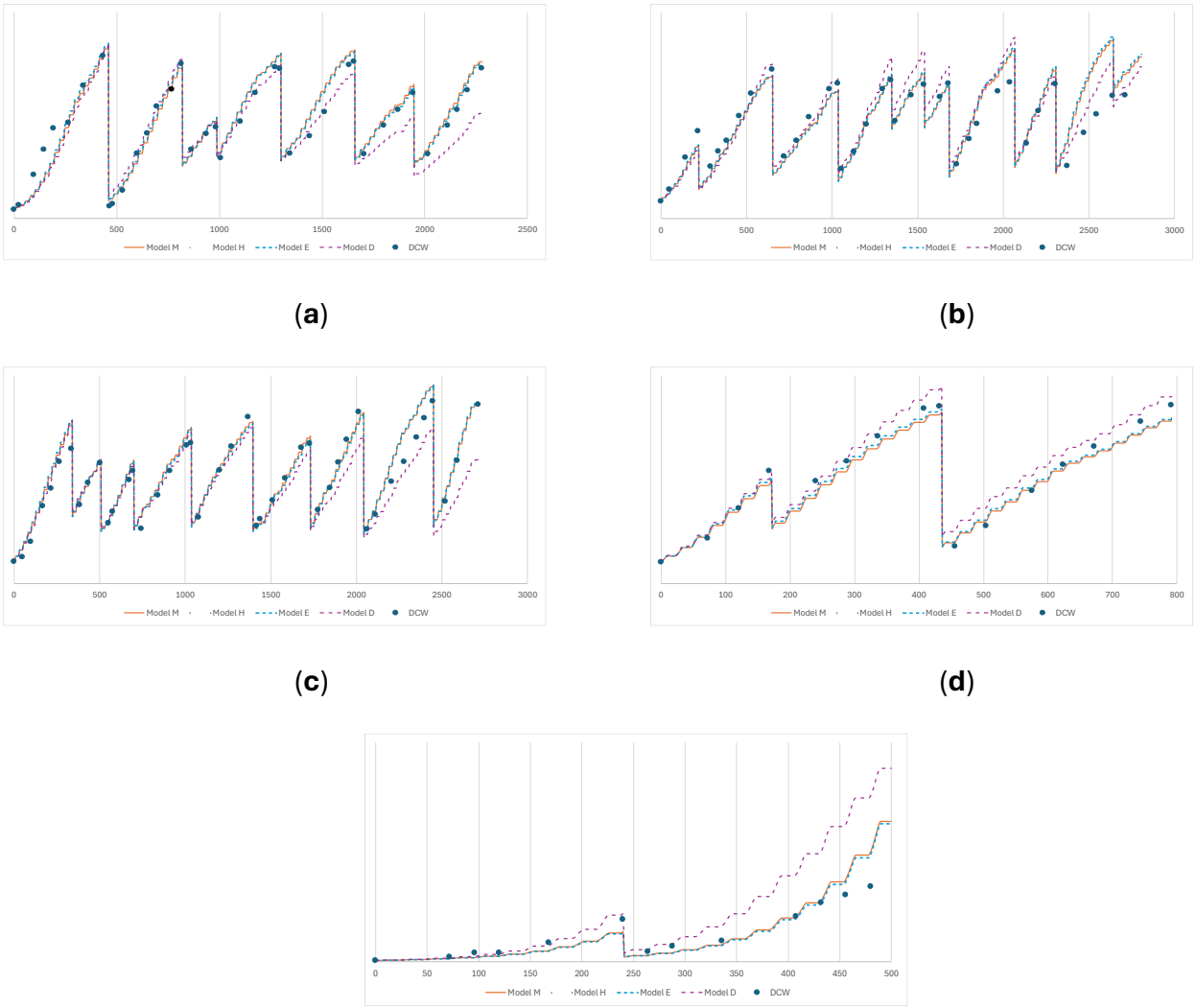

Figure 10. Results of the fitting of the models to the five training assays. The dots are the measured dry cell weights for each assay. The dashed lines are the fitted models. The *x*-axis is the time since inoculation (in hours); the *y*-axis is the biomass concentration (in kg m^{-3}). (a) M1-2; (b) M1-4; (c) U1-1; (d) U1-2; and (e) U2-2.

Table 6. RMSEs resulting from the fitting of the five training assays, along with the global R^2.

Assay	Model M	Model H	Model E	Model D
M1-2	0.070	0.079	0.102	0.170
M1-4	0.107	0.091	0.082	0.217
U1-1	0.104	0.106	0.098	0.161
U1-2	0.121	0.080	0.097	0.120
U2-2	0.073	0.048	0.054	0.130
Global	0.098	0.090	0.093	0.173

Overall, the fitting of Models M, H, and E to the five training assays is very similar and a good match for the experimental data, with Model H having the best performance. This result implies that there is, in fact, an effect of light inhibition for higher irradiance values (above I_{opt} = 41.4 MJ m^{-2} day^{-1}). Model D shows a much higher RMSE, which arises from the poor fitting observed in most assays.

The results of applying the models with the parameters previously obtained to validation assays can be found in Figure 11. A summary of the RMSE of each validation assay can be found in Table 4.

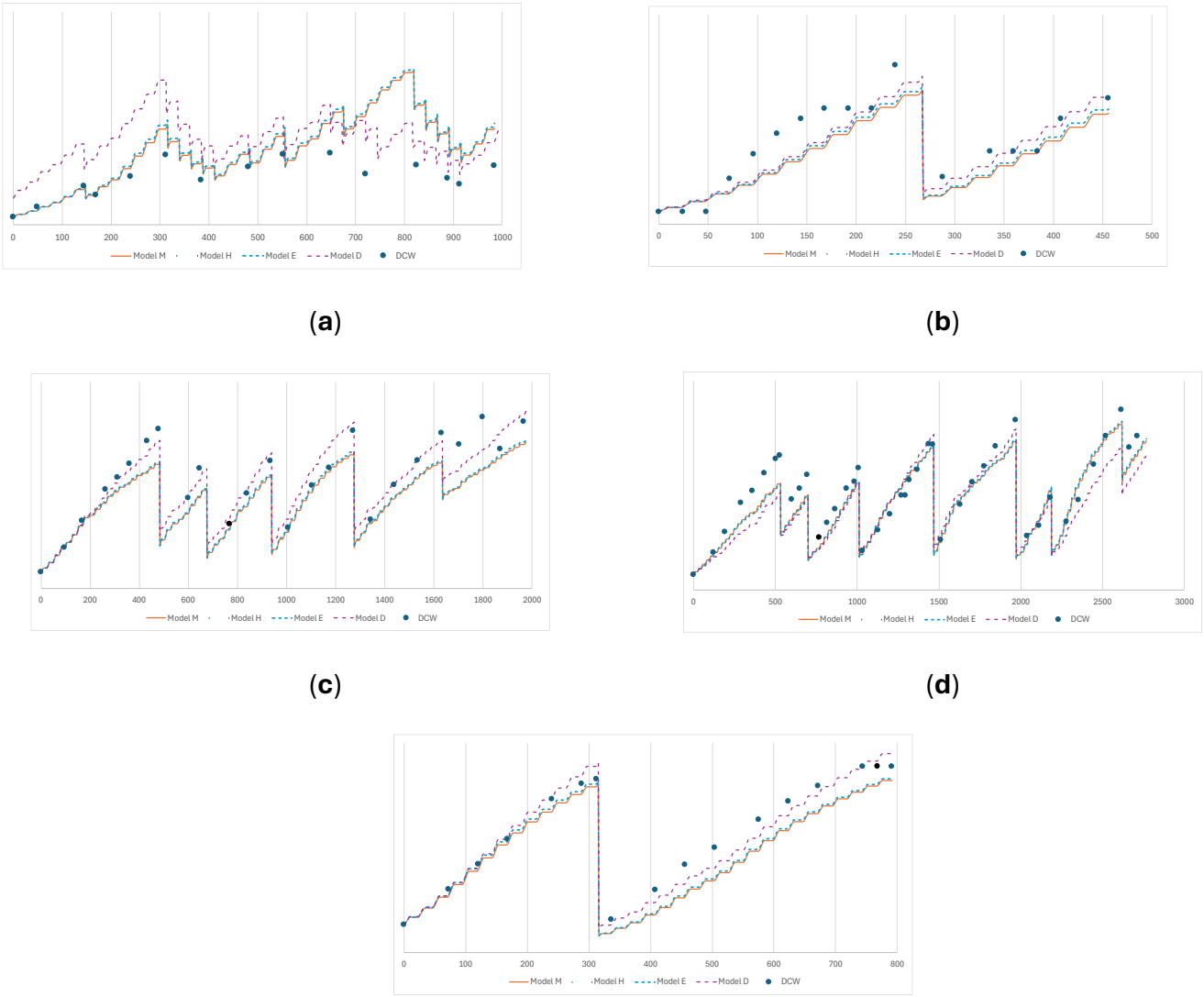

Figure 11. Results of the fitting of the models to the five validation assays. The dots are the measured dry cell weights for each assay. The dashed lines are the fitted models. The *x*-axis is the time since inoculation (in hours); the *y*-axis is the biomass concentration (in g L^{-1}). (a) M1-1; (b) M1-3; (c) U1-3; (d) U2-1; and (e) U2-3.

Table 7. RMSEs resulting from the fitting of the five validation assays.

Assay	Model M	Model H	Model E	Model D
M1-1	0.295	0.240	0.380	0.951
M1-3	0.360	0.407	0.273	0.236
U1-3	0.428	0.383	0.405	0.235
U2-1	0.206	0.220	0.211	0.292
U2-3	0.245	0.206	0.227	0.131
Global	0.309	0.296	0.302	0.413

In general, like with the training assays, Model H once again performed the best, with the lowest RMSE, and Model D had the highest RMSE, mainly due to the poor fitting to the M1-1 assay.

From these results, all models seem, in general, capable of explaining both the training and validation assays. Model H is overall the best at modeling both the training and validation assays.

3.3.3 Calculation of the Akaike Information Criterion (AIC)

The calculated values for ΔAIC, including all assays, were as follows:

- Model M: −694;
- Model H: −717;
- Model E: −707;
- Model D: −505.

Thus, according to the AIC, the best model of the four tested is, once again, Model H because it has the lowest ΔAIC, confirming the results that were obtained from the analysis of the RMSE.

3.3.4 Comparative Analysis of the Models

As shown in the previous sections, the four presented models showed good performance when fitted with the given dataset. However, it is also necessary to take a more holistic approach and interpret the validity of the application of the models.

In terms of biological interpretability, all models were chosen based on pre-existing, well-tested models in the literature. The parameters of each model can be understood in terms of established physical and biological phenomena, like light inhibition, light attenuation inside the reactor, and nutrient limitation. Model H was a reparametrized version of the existing Haldane models to better showcase parameters that could otherwise be difficult to interpret.

The models presented are also generalizable, being applied to three different reactor configurations with no discernible differences between them. That said, only one species was considered for this article, which limits its direct applicability to other species.

Models M, H, and E are robust, as they are not sensitive to large variations in the input conditions. They can withstand a wide range of input conditions and still perform as one would expect. Model D appears to be less robust, especially when the effect of nutrients is considered.

The models are also capable of explaining new data, as shown by the low RMSE values of the validation assays.

Finally, simpler models were shown to be as effective, if not more effective, at fitting the data, as Models M, H, and E (simpler models) performed better than Model D, and Models M and E (simpler models with just three parameters) were nearly as effective as Model H (which has four parameters).

3.3.5 Bootstrapping Statistics

For each model tested, bootstrapping was applied to all fitting parameters to obtain information on the uncertainty involved in the different model parameters. Below are the averages and medians for each model variable, as well as the respective standard deviations and the credible interval for each parameter (Tables 8–11). Since the number of measurements was high, the 95% credible interval was taken as follows:

$$Credible\ Interval = \pm 2 \cdot \sigma \tag{98}$$

where σ is the standard deviation. The corresponding histograms for each variable are also presented for each model.

3.3.5.1 Bootstrapping Data for Model M

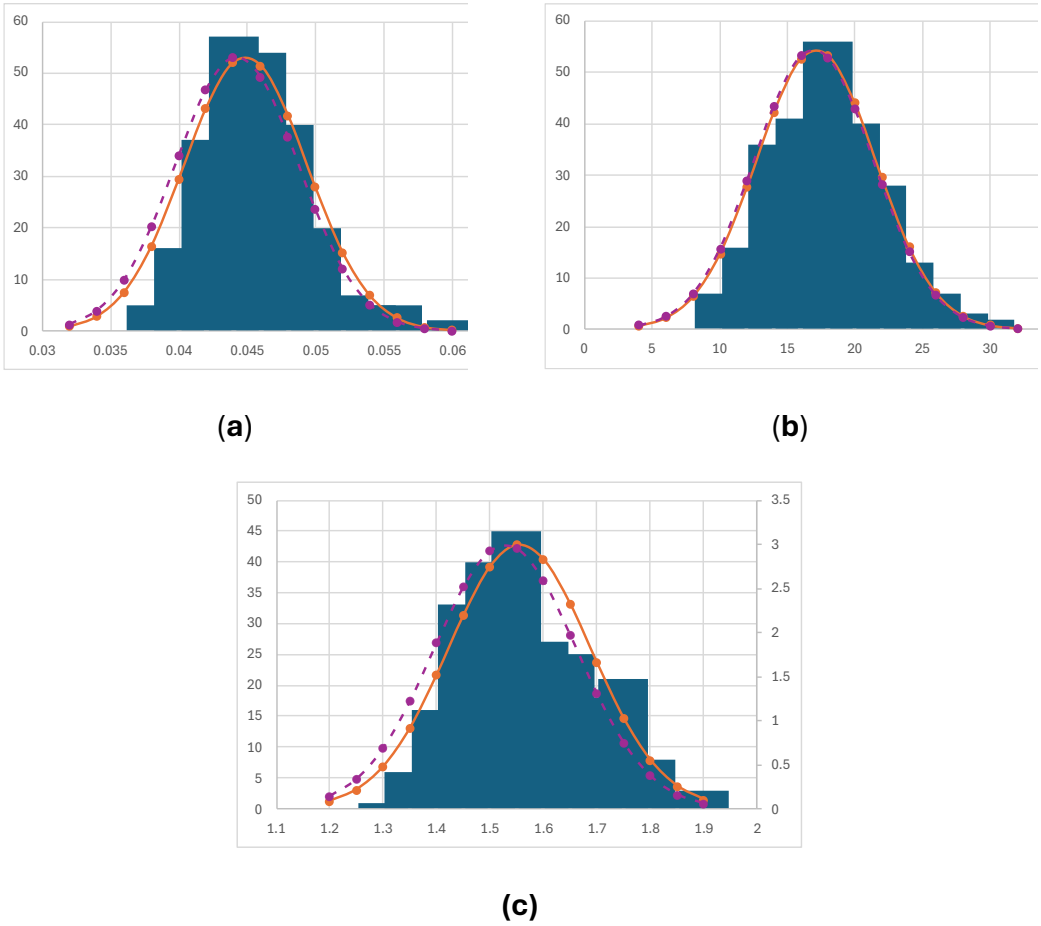

Figure 12. Histograms and the normal distribution for all the fitting parameters of Model M. The dashed lines correspond to the normal distribution when the median is taken as the mean value in the normal distribution. (a) μ_{max} (b) K_S (c) α.

Table 8. Mean, median, standard deviation, credible interval, and the value obtained from the fitting with the full dataset for every parameter of Model M.

Parameter	Mean	Median	St. Dev.	Credible Interval	Full Dataset Fitting
μ_{max} (h^{-1})	0.045	0.044	0.005	±0.010	0.041
K_S (MJ m^{-2} day^{-1})	17.13	16.95	4.404	±8.808	13.27
α (m^3 kg^{-1})	1.555	1.528	0.133	±0.266	1.645

3.3.5.2 Bootstrapping Data for Model H

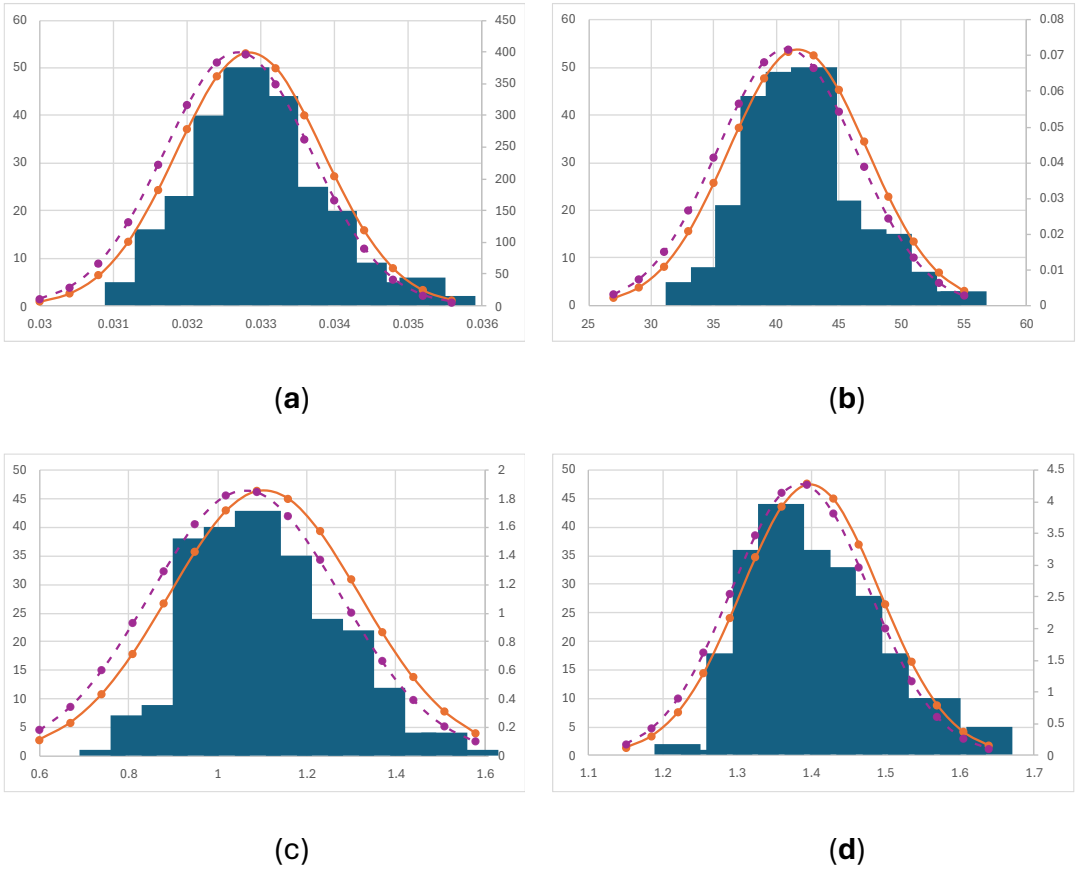

Figure 13. Histograms and the normal distribution for all the fitting parameters of Model H. The dashed lines correspond to the normal distribution when the median is taken as the mean value in the normal distribution. (a) μ_{max} (b) K_s (c) γ (d) α.

Table 9. Mean, median, standard deviation, credible interval, and the value obtained from the fitting with the full dataset for every parameter of Model H.

Parameter	Mean	Median	St. Dev.	Credible Interval	Full Dataset Fitting
μ_{max} (h^{-1})	0.033	0.033	0.001	±0.001	0.032
I_{opt} (MJ m^{-2} day^{-1})	41.74	40.84	5.549	±11.10	41.40
γ	1.106	1.063	0.214	±0.428	1.070
α (m^3 kg^{-1})	1.399	1.385	0.093	±0.186	1.337

3.3.5.3 Bootstrapping Data for Model E

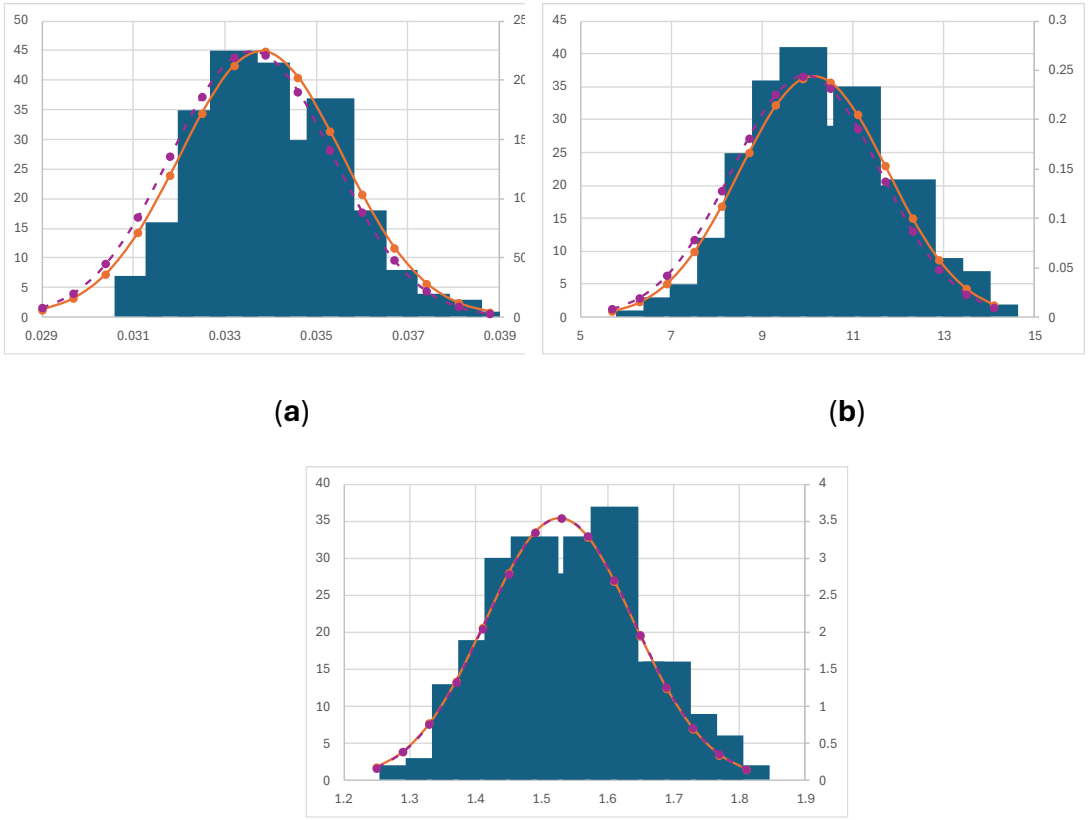

Figure 14. Histograms and the normal distribution for all the fitting parameters of Model M. The dashed lines correspond to the normal distribution when the median is taken as the mean value in the normal distribution. (a) μ_{max} (b) λ (c) α.

Table 10. Mean, median, standard deviation, credible interval, and the value obtained from the fitting with the full dataset for every parameter of Model E.

Parameter	Mean	Median	St. Dev.	Credible Interval	Full Dataset Fitting
μ_{max} (h^{-1})	0.034	0.034	0.002	± 0.004	0.033
λ_2 (MJ m^{-2} day^{-1})	10.13	9.957	1.631	± 3.262	9.933
α (m^3 kg^{-1})	1.527	1.528	0.113	± 0.226	1.515

3.3.5.4 Bootstrapping Data for Model D

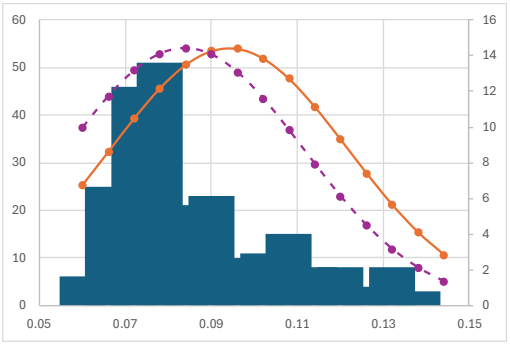

(a)

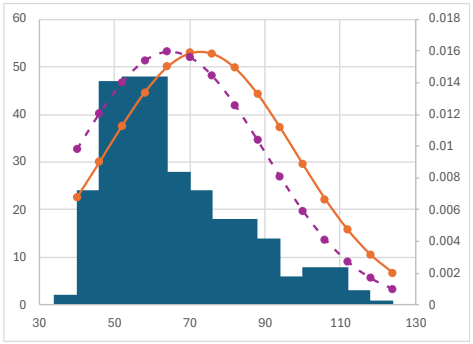

(b)

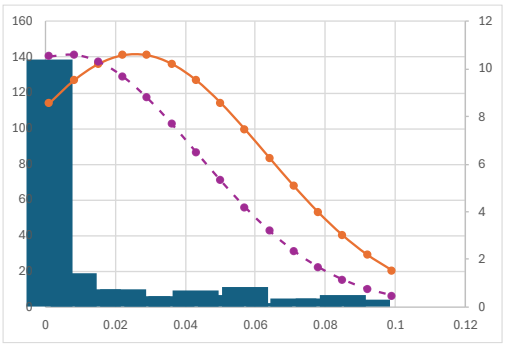

(c)

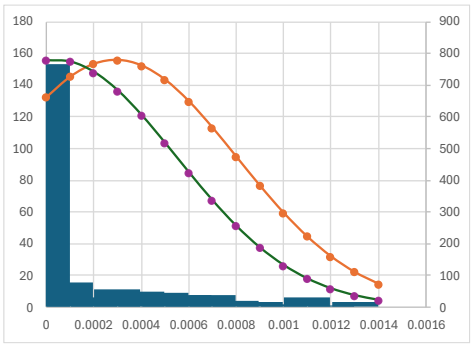

(d)

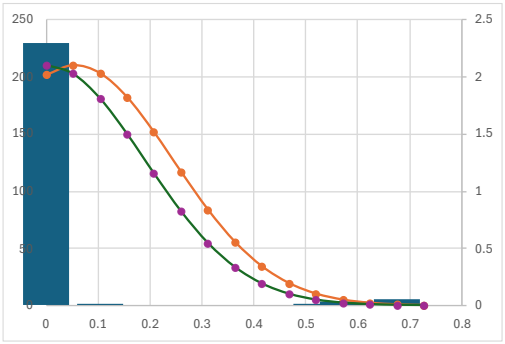

(e)

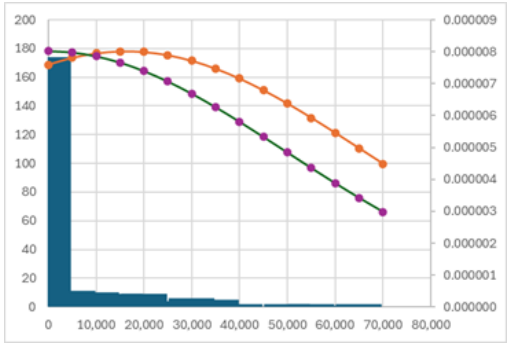

(f)

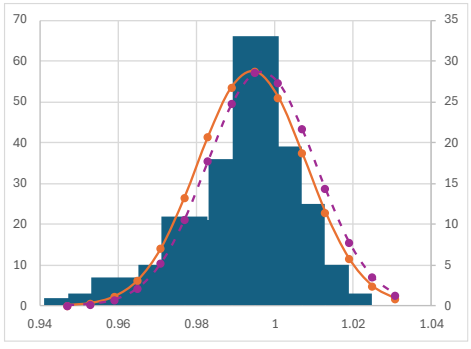

(g)

Figure 15. Histograms and the normal distribution for all the fitting parameters of Model H. The dashed lines correspond to the normal distribution when the median is taken as the mean value in the normal distribution. (a) μ_{max} (b) K_I (c) Q_{min} (d) Q_{max} (e) K_{sub} (f) Q_I (g) α.

Table 11. Mean, median, standard deviation, credible interval, and the value obtained from the fitting with the full dataset for every parameter of Model D.

Parameter	Mean	Median	St. Dev.	Credible Interval	Full Dataset Fitting
μ_{max} (h^{-1})	0.094	0.084	0.028	±0.056	0.082
K_S (MJ m^{-2} day^{-1})	72.86	64.74	25.02	±50.04	63.30
Q_{min} (g_N g_C^{-1})	0.026	0.006	0.037	±0.074	0.0025
ρ_{max} (g_N g_C^{-1} h^{-1})	2.907×10^{-4}	3.614×10^{-5}	5.117×10^{-4}	$\pm 1.023 \times 10^{-3}$	8.061×10^{-6}
K_{sub} (g_N g_C^{-1})	0.055	0.000	0.189	±0.378	0.000
Q_I (g_N g_C^{-1})	16334	14.84	49772	±99544	3.982
α (m^3 kg^{-1})	0.994	0.997	0.014	±0.028	1.003

3.3.5.5 Bootstrapping Discussion

The obtained distributions for the bootstrapped data for Models M, H, and E show that the obtained mean values for each variable are in good agreement with the values obtained with the neutral weighting of the errors for each data point (that is, all errors with a weight of 1). This is confirmed by the fact that the parameters calculated with neutral weighting usually fall well within the credible intervals obtained via bootstrapping.

The frequency distribution is often not symmetrical, which is due to the non-linear nature of the models tested. For the same reason, several of the parameters from Model D (namely Q_{min}, Q_{max}, K_S, and Q_I) show a very skewed distribution with many large outliers. This is again due to the non-linear nature of the systems, but also to the fact that this model does not seem to be able to provide an adequate description of the biological processes. In fact, for this model, several parameters have very wide confidence intervals. For example, the parameter K_S for Model D is estimated as 72.86 ± 50.04 MJ m^{-2} day^{-1}, which is a very large value when compared to K_S estimated by Model M, which is 17.73 ± 8.808 MJ m^{-2} day^{-1}. This reinforces the idea that the model incorporating the evolution of nutrients needs a much wider revision.

4 Model for Light Distribution Inside a Tubular Reactor

In this chapter, a model for the light distribution inside a photobioreactor will be derived and tested. The motivation for this model stems from the sparse availability of the modeling of light distribution inside tubular photobioreactors when compared to other geometries. The light distribution is of critical importance for modeling photobioreactors since, as light gradients form inside the reactor, the growth rate of the microorganism can be severely impacted, especially by very dense cultures. Unlike other types of photobioreactor, however, these light gradients occur in two dimensions due to the shape of the reactor tube (a cylinder), which increases the complexity of the calculation of these gradients.

As explained in Section 2.3.1.4, Fernandéz et al. [108] proposed a model to determine the path length inside a tubular reactor (hereby called the Fernández model), which had severe limitations, namely the necessity of utilizing iterations to determine a critical angle and the inability to apply the model to other reactor rotations. Laifa et al. [145] constructed a more sophisticated model to calculate path length inside a tubular reactor, including the effects of reflection and scattering, as explained in Section 2.3.1.5. However, the authors did not explicitly share the method used to determine the light path length inside the reactor. Furthermore, the reactor orientation was fixed (North-South), which also makes it difficult to apply to other reactor orientations.

Faced with the limitations of the models available in the literature, the model derived in this chapter aims to be more generic, yet more accurate than the models existing in the literature. Using a modified version of the model, the light attenuation at a given point on the outside of the reactor was determined. This value was then compared to measurements taken on real outdoor tubular reactors in operation using simple, custom-built apparatus with off-the-shelf light sensors.

4.1 Model Assumptions

This model uses the following assumptions:

- The reactor is abstracted to a single infinitely long tube.
- The reactor has turbulent flow, which means each individual algae cell travels randomly across all radial positions.
- The reactor is mounted on a flat plane with no obstructions to the solar rays.
- The behavior of one tube of the reactor can be extrapolated to the behavior of the entire reactor.

These assumptions result in the approximation that a thin circular slice of the reactor, perpendicular to the reactor axis, can be extrapolated to determine the behavior of the entire reactor. Since the properties of one of these slices are the same as the entire reactor, determining the behavior of light inside the cross-section allows the estimation of the light distribution of the entire reactor, which allows for the calculation of the average irradiation or the local growth rate inside the reactor.

The attenuation of light through a non-transparent medium can be determined using various equations, but the most common simplification is the Lambert-Beer law, which is found in Equation 99.

$$I_z = I_0 exp(-E_a X z) \tag{99}$$

E_a is a property of the specific microalgae used, the broth, and the wavelength of light; for this model, this value is considered to be constant and not dependent on the wavelength. However, the value of α may vary depending on factors such as concentration, temperature, physical characteristics of the microalgae (such as color or physical size, which can change over the course of a culture), and other components of the medium, among others. The biomass concentration, X, meanwhile, is an easily, if laboriously, measurable macroscopic quantity. Therefore, in this equation, the most crucial component and the hardest to determine is the path length, z. Determining this value will be the focus of this article.

By knowing the path length, the average irradiation in the thin slice of the reactor can be determined by integrating over the entire circle, dividing by its area. This is expressed in Equation 100.

$$I_{av} = I_0 \frac{\int_0^R \int_0^{2\pi} P_{rad} \cdot exp(-E_a X z(P_{rad}, P_{ang}))\, dP_{ang} dP_{rad}}{\int_0^R \int_0^{2\pi} P_{rad}\, dP_{ang} dP_{rad}} \tag{100}$$

where R is the radius of the reactor, and P_{rad} and P_{ang} are the polar coordinates of a point P(P_{rad}, P_{ang}) inside the reactor cross-section.

Alternatively, utilizing the same approach, it is possible to calculate the growth rate for every point inside the reactor, using any growth equation that is required, thus taking into account the local light level and then integrating to obtain the global growth rate.

For example, considering a Monod-like equation for the growth rate as found in Equation 101.

$$\mu_{local} = \mu_{max} \frac{I_{local}}{K_S + I_{local}} \tag{101}$$

where μ_{local} is the local growth rate (h^{-1}), μ_{max} is the maximum growth rate (h^{-1}), I_{local} is the local irradiation ($W\ m^{-2}$), and K_S is the Monod constant ($W\ m^{-2}$). Integrating Equation 101 over the entire cross-section results in Equation 102.

$$\begin{aligned} \mu_{global} &= \frac{\int_0^R \int_0^{2\pi} P_{ang} \cdot \mu_{max} \frac{I_{local}}{K_S + I_{local}} dP_{ang} dP_{rad}}{\int_0^R \int_0^{2\pi} P_{ang}\, dP_{ang} dP_{rad}} \leftrightarrow \\ \mu_{global} &= \mu_{max} \frac{\int_0^R \int_0^{2\pi} r \cdot \frac{I_0 exp(-E_a Xz(P_{rad}, P_{ang}))}{K_S + I_0 exp(-E_a Xz(P_{rad}, P_{ang}))} dP_{ang} dP_{rad}}{\int_0^R \int_0^{2\pi} r\, dd P_{ang} dP_{rad}} \end{aligned} \tag{102}$$

The proposed model considers the Sun's position in sky, by first calculating the two angles that define the sun's position on the celestial sphere (zenith (θ) and azimuth (ϕ)), then calculating the length of the path from a point inside a cross-section of the reactor cylinder with radius R_c to its surface. Using the path length, the Lambert-Beer law can be applied to determine the available fraction of incident irradiation for each point inside this cross-section.

4.2 Calculation of the Position of the Sun

The Sun's position in the sky is defined by two angles: the zenith (θ), which is the angle between the vertical direction and the Sun's position; and the azimuth angle (ϕ), which is the angle measured, clockwise, from the north direction. Both the zenith angle and the azimuth angle depend only on the day of the year, the time of day, the latitude (η) and the longitude (λ) of the location. Although both angles can vary over the course of years, this variation is negligible and will be ignored for this model. The involved angles can be found in Figure 16.

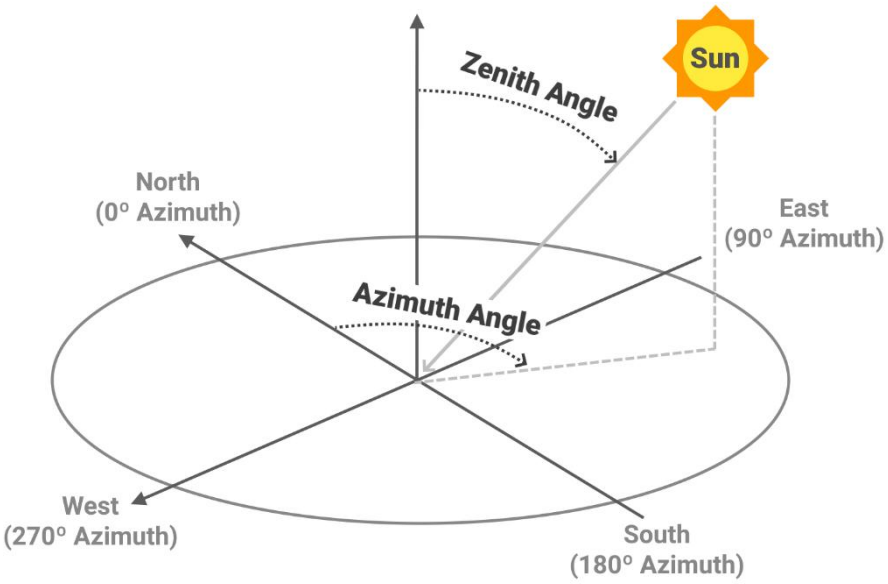

Figure 16: Solar zenith and azimuth angles [146].

On Appendix A, the values of the zenith and azimuth are determined using equations given by NOAA (National Oceanic and Atmospheric Administration of the USA) [147].

After calculating both the zenith angle and the azimuth angle, it is then possible to convert the Sun's coordinates from spherical to cartesian. This requires having a value for the distance of the Sun from the origin (S_{rad}). Technically this value should be the distance of the Sun to the Earth, which is 152 million kilometers, but for the model to be effective, S_{rad} merely needs to be much larger than the radius of the tubular reactor, R_c, so that the sun's rays are approximately parallel to any point inside the reactor. The value used in this model was 100 meters.

To convert from spherical to cartesian coordinates, Equation 103 is used.

$$S(S_x, S_y, S_z) = (S_{rad} \sin\theta \cos\varphi\,, S_{rad} \sin\theta \sin\varphi\,, S_{rad} \cos\theta) \qquad (103)$$

4.3 Calculation of the Path Length for a Given Point

The reactor is approximated by a single infinite cylinder centered on (0,0,0) in which the longitudinal y-axis is oriented along the East-West direction. This means that the reactor is by default (with no rotation) oriented East-West, with East being the negative direction and West the positive direction. The x-axis is North-South, with North being the positive direction. The equation of the reactor tube with radius R_c is thus:

$$R_c{}^2 = x^2 + z^2 \qquad (104)$$

Inside this cylinder, a circular cross-section for y=0 is defined. A point P is defined inside this cross-section with the following cartesian coordinates:

$$P(Px, Py, Pz) = (P_{rad} \cdot sin\ P_{ang}, 0, P_{rad} \cdot cos\ P_{ang}) \quad (105)$$

with P_{rad} as the radial position (equal to or smaller than R_c) and P_{ang} as the angular coordinate of the point around the cross-section. These two values will be used as input for the calculations.

Since the glass cylinder is filled with water, there are two changes in media as the sun rays travel from the air to point P: between the air and the tube glass, and between the glass and the broth. Therefore, the effects of Snell's law (refraction) and Fresnel's law (reflection) apply. To take into account both effects, the incidence angle β needs to be determined, which is the angle between the solar rays and the cylinder normal. The cylinder normal N_C is the vector connecting the point of intersection T and its projection onto the y-axis.

Diagrams of the reactor are shown in Figure 17.

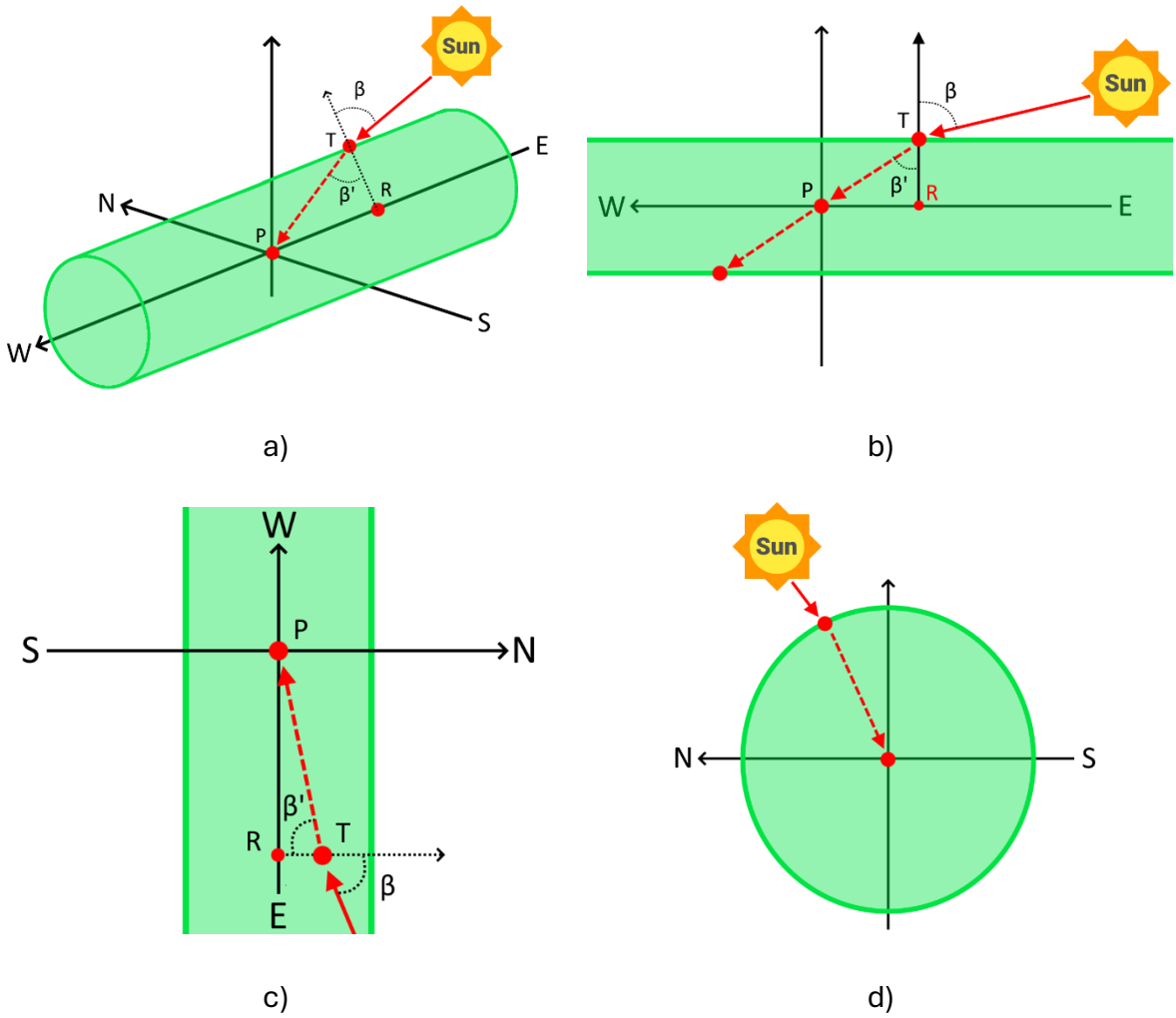

Figure 17: Diagrams of the reactor tube and the relevant points and angles. a) Angled view b) Side view c) top-down view d) West-facing view. P is the point inside the reactor whose path length needs to be determined. T is the point of intersection between the sun ray and the cylinder. R is the projection of point T onto the y-axis. β is the penetration angle of the sun rays, and β' is the refraction angle as determined via Snell's law. Angles and the position of the sun are not to scale.

β' is trivial to calculate for a planar surface, applying Snell's law directly.

$$sin\,\beta' = sin\,\beta\,\frac{n_1}{n_2} \tag{106}$$

with n_1 and n_2 being the refraction indexes for the two media involved in the refraction.

To calculate the fraction of light that is reflected (R_0), Fresnel's sine and tangent laws (shown in Equation 106) are used.

$$R_0 = \frac{1}{2}\left(\frac{sin(\beta-\beta')^2}{sin(\beta+\beta')^2} + \frac{tan(\beta-\beta')^2}{tan(\beta+\beta')^2}\right) \tag{107}$$

However, for the real case of a tubular reactor, determining the value of β is more difficult to apply for two reasons.

The first is that there are two media transitions between the sun rays and point P (air to glass, and glass to water). As a simplification, and because the refraction indexes of water and borosilicate glass are similar (1.3325 and 1.3995, respectively) [148], only one application of Snell's law will be considered, with n_1 being approximately 1, which is that of air [148].

The second reason is that to apply Snell's law it is necessary to calculate the angle of penetration of the sun rays in relation to the normal of the curved surface of the reactor. Not only is this calculation laborious due to the geometry, but it would require iterations to determine the location of point T and the path of the sun ray after being refracted. This calculation is shown in Appendix D.

Therefore, as a simplification, the incidence angle is assumed to be equal to the zenith, that is:

$$sin\,\beta' = sin\,\theta\,\frac{n_1}{n_2} \tag{108}$$

Therefore, the apparent position of the sun as seen from point P, $S^*=(S_x^*, S_y^*, S_z^*)$, is given by Equation 109.

$$S^*(S_x^*, S_y^*, S_z^*) = (S_{rad}\sin\beta'\cos\varphi\,, S_{rad}\sin\beta'\sin\varphi\,, S_{rad}\cos\beta') \tag{109}$$

In three dimensions, a line between points S* and P can be defined as:

$$S^*P = (S_x^* + t\cdot(P_x - S_x^*), S_y^* + t\cdot(P_y - S_y^*), S_z^* + t\cdot(P_z - S_z^*)) \tag{110}$$

with t is the parametric variable.

To determine the length of the path inside the reactor, it is necessary to first determine the coordinates of the two points in the S*P line that intercept the cylinder's surface. This can be done by solving the cylinder equation with the coordinates of the S*P line. This results in Equation 111, which is a quadratic equation.

$$R_c{}^2 = (S_x^* + t \cdot (P_x - S_x^*))^2 + (S_z^* + t \cdot (P_z - S_z^*))^2 \quad (111)$$

Solving for *t* results in two solutions, represented in Equation 112.

$$t = \frac{-S_x^*\bar{X} - S_z^*\bar{Z} \pm \sqrt{(S_x^*\bar{X} + S_z^*\bar{Z})^2 - (\bar{X}^2 + \bar{Z}^2)(S_x^{*2} + S_z^{*2} - R_c{}^2)}}{\bar{X}^2 + \bar{Z}^2}$$
$$\bar{X} = P_x - S_x^* \quad (112)$$
$$\bar{Z} = P_z - S_z^*$$

The two solutions represent the two points where the cylinder is intercepted by the line SP. To obtain these two points, one must simply replace the obtained values of *t* in the equation of the SP line. The point closest to the sun, where the sun rays penetrate the reactor, is the correct solution. This point (T) is the one with the positive value of *z*.

Finally, the length of the path the light travels can be calculated using Equation 113, which gives the distance between points P and T in three dimensions.

$$\mathrm{z} = \mathrm{d}(\mathrm{P},\mathrm{T}) = \sqrt{(P_x - T_x)^2 + (P_y - T_y)^2 + (P_z - T_z)^2} \quad (113)$$

4.3.1 Theoretical Analysis of the Model

Below are presented several theoretical analyses of the model results. The latitude and longitude used in these analyses were those of Lisbon, Portugal (38.7223ºN, -9.1393W). The reactors all had a radius of 0.0325 m. The implementation of the model, including the necessary integration steps, was done in C#.

4.3.1.1 Attenuation Inside a Reactor Over the Course of a Day

As an example, Figure 18 shows the path length of a point in the center of the reactor (that is, P_{rad}=0 and P_{ang}=0) over the course of a day, for key dates of the year (Spring Equinox – Day 82; Summer Solstice – Day 172; Fall Equinox – Day 266; Winter Solstice – Day 355).

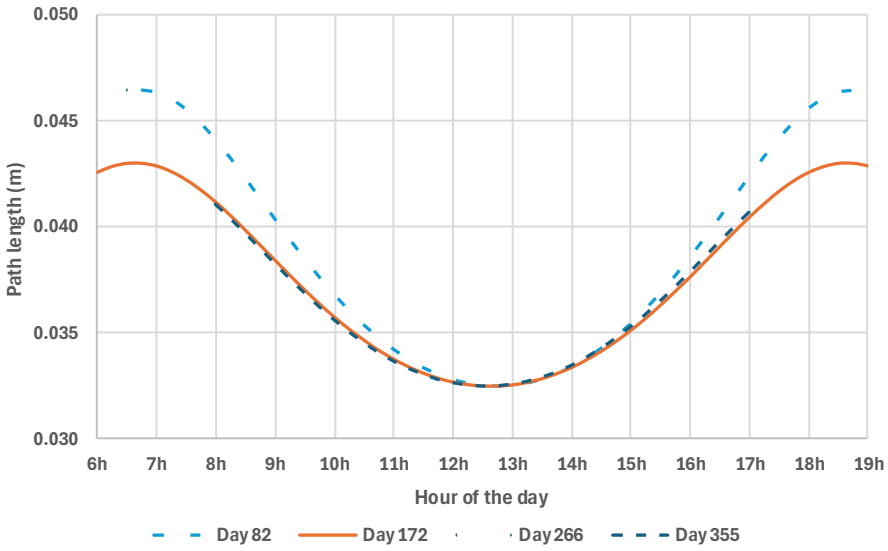

Figure 18: Path length for the center of a reactor oriented East-West over the course of a day, for key dates of the year (Spring Equinox – Day 82; Summer Solstice – Day 172; Fall Equinox – Day 266; Winter Solstice – Day 355). Path lengths corresponding to time periods when the sun was below the horizon are not shown.

As can be seen in Figure 18, the path length of this point varies considerably depending on the day of the year, especially comparing the solstices and the equinoxes. The first observation is that the path lengths for the Winter Solstice and the Fall Equinox are extremely similar to the ones in the complementary date (Summer Solstice and Spring Equinox). This is because the declination of the sun on days of the year separated by half a year has the same absolute value but opposite signs, which causes the zenith and azimuth to be correlated, and so the path length at this specific point of the reactor has nearly the same value. The differences are mostly due to the different values of the equation of time for these different dates.

The other observation is a characteristic “bump” in the early morning and evening, more noticeable during the Summer Solstice. This occurs when the azimuth is aligned with the reactor axis (so East in the morning and West in the evening). At these two moments in the day, the path length is maximized because the sun rays have to travel further inside the reactor to reach the center.

During the summer solstice only, the sun is high enough in the sky to still be above the horizon even after the azimuth aligns with the east-west axis. This causes the period before and after the alignment to have a shorter path length. This is due to the sun rays entering the reactor not from above, but from the north side of the reactor, which reduces the path length.

Finally, during solar noon (around 12:30 UTC), the sun is aligned with the x-axis (North-South), causing the sun rays to enter the reactor on the plane of the cross-section. Since point P is in the

center of the reactor in this example, the path z is always going to be the reactor radius, independently of the zenith. This also corresponds to the minimum value of z for this point.

Figure 19 shows the average fraction of light (I_{av}/I_0) for a reactor oriented East-West for the same key dates of the year. The values do not take into account the lower sunlight intensity during sunrise and sunset due to absorption by the atmosphere, which will also be addressed later.

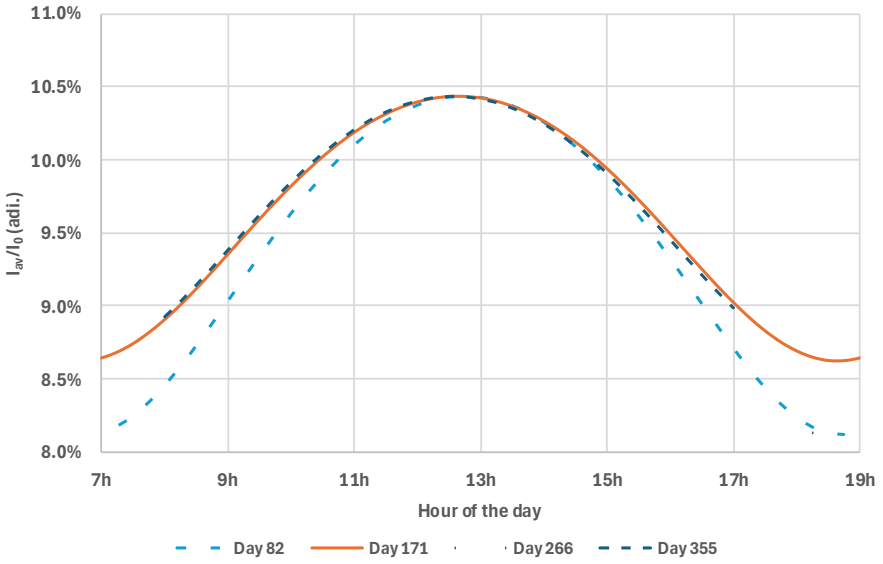

Figure 19: I_{av}/I_0 for a reactor oriented East-West over the course of a day, for key dates of the year (Spring Equinox – Day 82; Summer Solstice – Day 171; Fall Equinox – Day 266; Winter Solstice – Day 355). E_a=50 m^2 kg^{-1}, X=0.5 g m^{-3}. I_{av}/I_0 corresponding to time periods when the sun is below the horizon are not shown. The latitude and longitude of the location were 38.722º and -9.1393º. All times are UTC+0, thus not taking into account Daylight Savings Time.

It shows a similar picture to that of Figure 18, except "reversed" over the y-axis. This is because light attenuation is determined by the integration of the Beer-Lambert law over the entire reactor, which depends on the path length of every point inside the reactor. The fact that the graphs are so similar is notable, however, since it shows that the effect of the sign switch of the declination over a six-month period is still observable even when integrating over the entire reactor. This means that, counter-intuitively, the light attenuation inside an East-West reactor is the same for summer and winter.

4.3.1.2 Effect of the Rotation of the Reactor

Assuming the reactor is perfectly parallel to the ground, the rotation of the reactor is equivalent to rotating the position of the sun in the sky, that is, to adding a certain angle to the Sun's azimuth as calculated by Equation A7. By default, the reactor is in the East-West direction (0°). Adding 90° to the Sun's azimuth is equivalent to rotating the reactor 90°, which is the North-South direction. Adding 45° is equivalent to rotating the reactor to a NE-SW orientation. Shifts beyond 90°

are possible, but these are functionally equivalent to shifts of less than 90° because of the symmetry of the reactor. For example, a 180° rotation merely flips the reactor around, with the only difference from the 0° orientation being the side of the reactor the sun's rays enter.

Using this methodology, the fraction of light inside the reactor was plotted over the course of a day, for the same key days of the year as Figure 19 and for key reactor rotations (45° and 90°). The two graphs can be found in Figure 20.

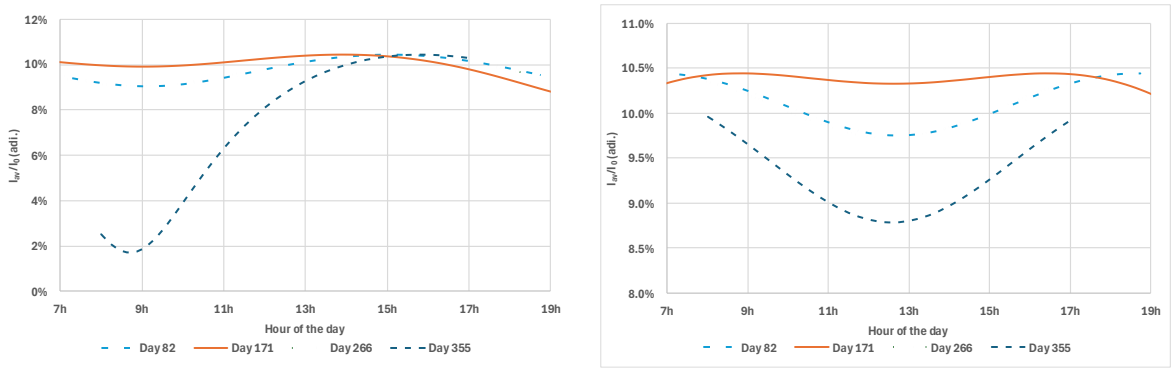

(a) (b)

Figure 20: I_{av}/I_0 for reactors oriented Northeast-Southwest (a) and North-South (b) over the course of a day, for key dates of the year (Spring Equinox – Day 82; Summer Solstice – Day 171; Fall Equinox – Day 266; Winter Solstice – Day 355). E_a=50 m^2 kg^{-1}, X= 0.5 g m^{-3}. I_{av}/I_0 corresponding to time periods when the sun is below the horizon are not shown. The latitude and longitude of the location were 38.722º and -9.1393º. All times are UTC+0, thus not taking into account Daylight Saving Time.

As can be observed in Figure 20a, the maximum value of I_{av}/I_0 is shifted later in the day when compared with Figure 19, peaking at around 15:00 UTC. This is because at solar noon (12:30 UTC), the reactor angle causes the path length inside the reactor to be greater, as the sun rays enter at an oblique angle. Likewise, the minimum of all graphs is shifted to slightly later in the day (around 9:00 UTC) when compared to the values shown for Figure 19 because that corresponds to the time of day when the sun's azimuth is aligned with the reactor axis. Although not shown, the reactor being rotated by -45° causes all graphs to mirror along the solar noon (so the maximum would occur in the morning, while the minimum would occur during the evening). The attenuation for the two solstices is also not the same for this rotation, which makes this peculiarity exclusive to the East-West rotation.

When the reactor is rotated 90°, as expected, there is greater attenuation during solar noon than during sunrise and sunset, which is more noticeable during the Winter solstice. This is because during solar noon, the sun's azimuth is oriented along the length of the reactor, which means the sunrays must travel further inside the reactor; during sunset and sunrise, the sun is positioned on the left or right of the reactor, thus the sunrays must travel a shorter distance inside

the reactor. The effect of lower zenith during the mornings/evenings (causing path lengths to be longer) and the effect of the sun being oriented along the reactor axis during solar noon (causing path lengths in the morning/evenings to be shorter) almost balance out during the summer solstice, with a nearly constant value of attenuation over the entire day.

Finally, it can be observed that there is, in general, more light attenuation when the reactor is oriented to EW, but that the attenuation is greater during the peak hours of solar insolation in the NS orientation. Finally, it is notable that no matter what the orientation, the peak available light is always around 10%, which suggests that the effect of reactor orientation is more important during the morning and evening hours.

4.3.1.3 Ideal Reactor Orientation

The ideal reactor orientation depends on multiple factors. In general, it could be said to be the one where the most amount of light is available to the reactor, that is, with the least amount of light attenuation inside the reactor, on average. Note, however, that the optimum will also depend on the microalgae species being grown in the reactor, being subject to light inhibition effects or not. In the case of light inhibition effects, an orientation that lowers the amount of light during the hours of the day when the sunlight intensity is higher, smoothing out the light intensity profile could be ideal. In the following analysis, it will be assumed that the microalgae species do not suffer from light inhibition.

The ideal reactor orientation depends not only on the amount of attenuation, but also on when in the day it occurs. In general, mornings and evenings have less available sunlight because the sun is lower in the sky, and thus more sunlight is absorbed in the atmosphere. To take into account this effect, data from the Photovoltaic Geographical Information System (PVGIS) from 2005 to 2023 for this location were combined with the model results shown in Figure 19 and 20. The maximum registered direct irradiation for every hour of every date between those two dates was identified, which allows the minimization of the effect of cloud coverage, which could affect the calculations.

Figure 21 contains the value of I_{av} for a reactor-oriented NS, NE-SW, and EW for key days of the year, using the data from PVGIS. Table 12 contains the daily averages of I_{av} for each of these days and orientations.

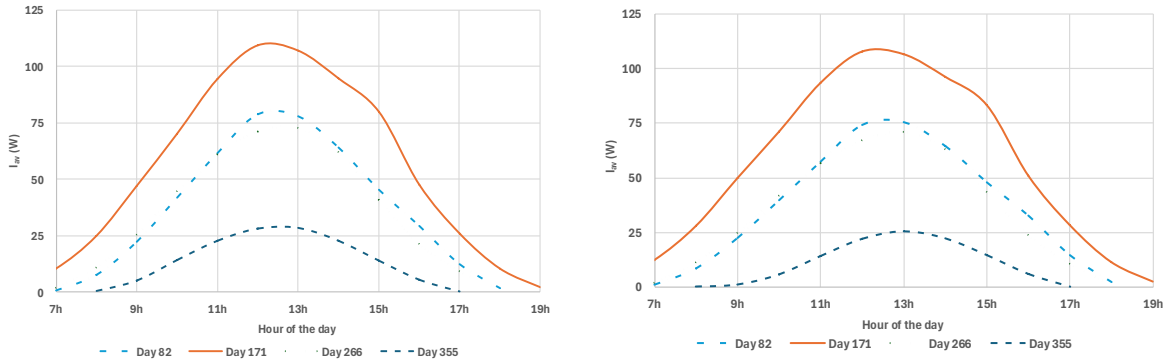

(a)

(b)

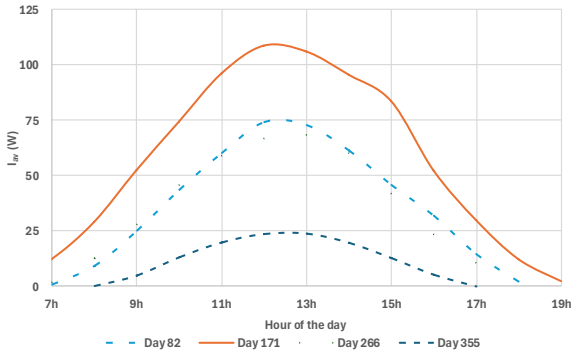

(c)

Figure 21: I_{av} for reactors East-West (a), Northeast-Southwest (b) and North-South (c) over the course of a day, for key dates of the year (Spring Equinox – Day 82; Summer Solstice – Day 171; Fall Equinox – Day 266; Winter Solstice – Day 355). E_a=50 m^2 kg^{-1}, X=0.5 g m^{-3}. The latitude and longitude of the location were 38.722º and -9.1393º. All times are UTC+0, thus not taking into account Daylight Saving Time.

Table 12: Average I_{av} (W m^{-2}) for different reactor orientations and for key dates of the year (Spring Equinox – Day 82; Summer Solstice – Day 171; Fall Equinox – Day 266; Winter Solstice – Day 355) and the yearly average. E_a =50 m^2 kg^{-1}, X=0.5 g m^{-3}. The latitude and longitude of the location were 38.722º and -9.1393º.

Day	East-West	Northeast-Southwest	North-South
Spring Equinox	52.06	52.26	52.73
Summer Solstice	62.62	64.55	66.11
Fall Equinox	49.39	49.60	50.00
Winter Solstice	31.35	29.57	28.12
Yearly Average	51.52	51.91	52.35

It can be seen in Figure 21 and Table 12 that, during the equinoxes, the amount of light in the reactor is virtually the same across all orientations. However, the more the reactor is oriented NS, the greater the average I_{av} on the summer solstice, with the inverse being observed during the winter solstice. This is because in the NS orientation, the light attenuation is nearly constant over the course of the summer solstice, which increases the amount of light available in the reactor during the morning/evening. The difference between the EW and NS orientations is around 10%.

In EW orientation, however, the winter solstice has the same attenuation profile as the summer solstice, which increases the available light when compared to the NS orientation, which has a significant dip during noon, when the sun is stronger.

Therefore, it is reasonable to conclude that the ideal reactor orientation for most scenarios in this location is NS, as in general it is more favorable to grow microalgae during the summer when there is more direct sunlight available. However, if a certain species necessitates colder temperatures and/or lower irradiation values, an East-West orientation might be preferable.

4.4 Materials & Methods

To test the validity of the model presented, an experimental setup using pilot-scale reactors was devised. This experiment involved using light sensors to measure the illumination when exposed directly to sunlight and in different positions around a working photobioreactor. In this manner, the attenuation of light on these points could be calculated and compared to the amount as predicted by the model.

For this experiment, a set of 4 BH1750 luxmeters was connected to an Arduino ESP8266 microcontroller. A C language program was written to interact with these light sensors using publicly available libraries. The sensors measured the illumination thrice in quick succession (a few milliseconds) every 30 seconds, and these three values were then averaged to obtain a measurement for each timestamp. The sensors were calibrated using a portable UNI-T model UT383S luxmeter under various light conditions (sunlight, both direct and shaded, and various artificial lamps). These calibrations are found in Appendix E.

The light sensors were attached to the outer surface of a clean, operational outdoor pilot-scale photobioreactor in 4 positions, henceforth dubbed A through D. These are shown in a diagram in Figure 22.

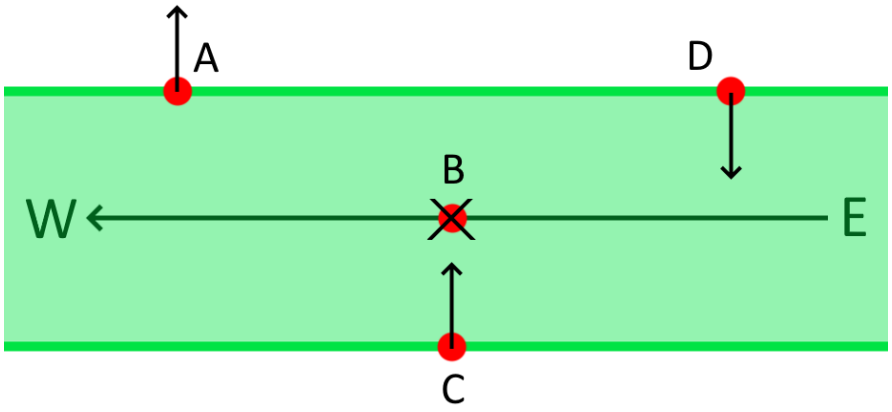

Figure 22: Positions of the four sensors used in the experiment (side view). Sensor B is facing inward towards the viewer.

The sensor in position A was placed faced up and measured the global horizontal irradiation. Position C measured the irradiation on the bottom of the reactor. Position B measured the irradiation on the north side of the reactor, while Position D measured the diffuse radiation inside the reactor. The data for sensors B and D were not utilized in this article.

Photographs of the experimental set-up are found in Figure 23.

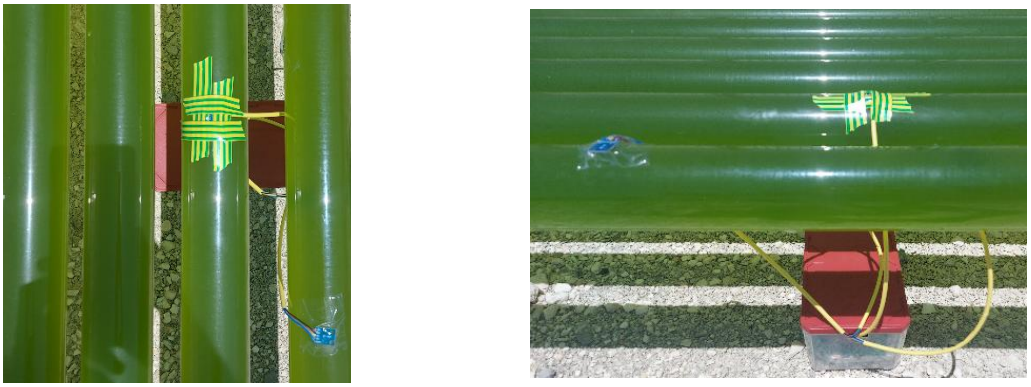

(a) (b)

Figure 23: Photographs of the experimental setup. (a) top view (b) side view. The sensor placed on top of the reactor on the left tube in (a) is Sensor A (facing up). The sensor placed on the right tube in (a) is Sensor D (facing down). Sensor B was placed 90 degrees facing inwards on the right tube. Sensor C was placed facing up on the right tube (not visible). The plastic box contained the Arduino microcomputer and other electrical components used to record and process the data.

There were LED lights permanently affixed under the reactor, but in a section far away from the sensors, and therefore their effects on the sensors are negligible.

The sensors were run continuously in two different assays, dubbed the July assay and the August assay.

The July assay ran from 2024/7/4 at 15:00 through to 2024/7/8 at 10:00, lasting 91 hours. The average standard deviation for each measurement was 0.13% for Sensor A and 2.85% for Sensor C.

The August assay ran from 2024/8/21 at 18:00 through to 2024/7/25 at 20:00, lasting 98 hours. The species used in this assay accumulated starch. This assay had two sensors in position C (dubbed C_1 and C_2).

4.4.1 Determining the Irradiation Measured by Each Sensor

The presented model has been used to calculate the average irradiation on a cross-section of a cylindrical reactor. However, by skipping the integration step, it is possible to calculate instead the local irradiation at any point inside the reactor.

As the sensors are outside, on the surface of the reactor, it is assumed that the measured values on the surface are the same as the values measured just inside the cylinder (that is, there is no media transition between the sensor and the glass surface). However, because the model returns the point attenuation considering a direct line of sight to the sun, while the sensors have a small physical area, the number of photons (and therefore the irradiation) hitting the sensor changes depending on the angle of the sensor in relation to the incident light beam. To calibrate for this effect, the direct irradiation measured by every sensor is determined before any attenuation calculation is done.

Since Sensor A and C were parallel to the ground, the measured irradiation is independent of the azimuth, while it is proportional to the cosine of the incidence angle. In this model, the incidence angle is assumed to be equal to the zenith. This is shown in Figure 24 for a sensor placed on the bottom of the reactor.

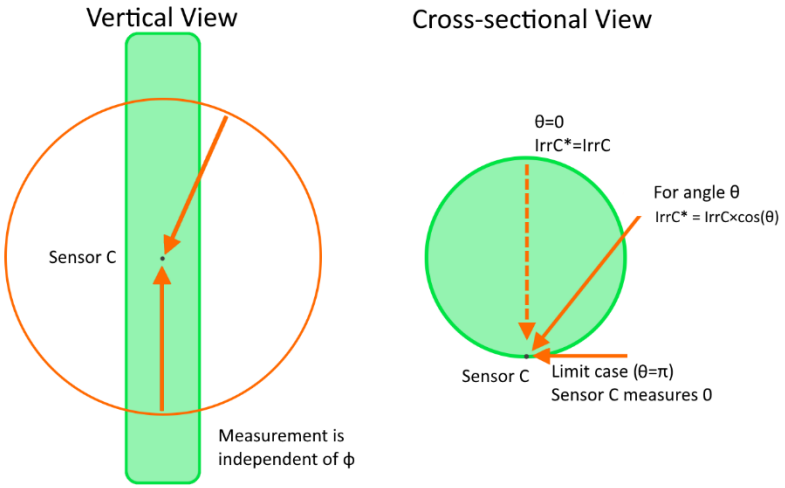

Figure 24: Diagram of the geometric considerations of the light reaching Sensor C, placed on the bottom of the reactor facing up.

The observed irradiation on sensor A is given by

$$I_A = I_{dir}{}^{*} + I_{diff} \tag{114}$$

where I_{dir}* is the direct radiation from the sun as observed by the sensor (considering the geometric effect described in Figure 24), and I_{diff} is the diffuse radiation from the sky and reflections off of objects. I_{diff} can be estimated from horizontal global radiation (what I_A measures) via various correlations using the clear sky index (K_t), which is the ratio between global horizontal radiation and the extraterrestrial radiation (in the absence of atmosphere). However, for the purposes of this validation experiment, days with clear skies were chosen, and from these, only those moments with clear sky conditions were used. According to [149], a clear sky day has a K_t of 0.8, which corresponds to a ratio of direct and diffuse radiation (B) of 0.222; that is, I_{diff} contributes 22.2% of the global horizontal radiation.

This is expressed in Equation 115.

$$\mathrm{I_A} = \mathrm{I_{dir}}\cos\theta + \mathrm{I_{diff}} \leftrightarrow \mathrm{I_A} = \mathrm{I_{dir}}\cos\theta + \mathrm{BI_A} \leftrightarrow \mathrm{I_{dir}} = \frac{\mathrm{I_A}(1-\mathrm{B})}{\cos\theta} \tag{115}$$

where I_{dir} is the irradiation coming directly from the sun rays.

Using the same method, the equation for I_{diff} can be deduced depending on the value of I_{dir}.

$$I_{diff} = BI_A \leftrightarrow I_{diff} = B\left(I_{dir}\cos\theta + I_{diff}\right) \leftrightarrow I_{diff}(1-B) = BI_{dir}\cos\theta \leftrightarrow$$
$$\leftrightarrow I_{diff} = \frac{B\cos\theta}{1-B} I_{dir} \tag{116}$$

The irradiation observed by sensor C (I_C) has two components: I_{dirC}, which is the light coming directly from the sun, and I_{diffC}, which is the diffuse light coming from every direction in the sky.

I_{dirC} is affected by three distinct factors: the refraction of light inside the reactor (estimated via Snell's law), the reflection of light on the reactor's surface (estimated via Fresnell's laws, which in turn uses the refraction angle calculated via Snell's law), and the attenuation of light inside the reactor (estimated via Beer-Lambert's law). All these effects are expressed in Equation 117.

$$\begin{gathered} I_{dir_C} = {I_{dir_C}}^* \cdot (1 - R_0) \cdot exp(-\alpha X z) \\ \leftrightarrow I_{dir_C} = I_{dir} \cos\beta' \cdot (1 - R_0) \cdot exp(-\alpha X z) \end{gathered} \tag{117}$$

$I_{diffC,}$ however, is much more difficult to calculate because these same factors must be considered for every point in the sky. For this reason, it will be assumed that I_{diffC} is proportional to I_{diff}, with the constant of proportionality being a new variable (ζ) which combines the effects of Snell's law and Fresnel's law (see Appendix F). This is expressed in Equation 118.

$$I_{diff_C} = \zeta \cdot exp\left(-\alpha X z_{diff}\right) \cdot I_{diff} = \frac{\zeta B \cos\theta}{1 - B} I_{dir} \cdot exp(-\alpha X \cdot 2R_C) \tag{118}$$

The combined equation for I_C is shown in Equation 119.

$$\begin{gathered} I_C = I_{dir_C} + I_{diff_C} \leftrightarrow \\ \leftrightarrow I_C = I_{dir} \cos\beta' \cdot (1 - R_0) \cdot exp(-\alpha X z) + \frac{\zeta \cos\theta\, B}{1 - B} I_{dir} exp(-\alpha X) \leftrightarrow \\ \leftrightarrow I_C = I_{dir} \left[\cos\beta' (1 - R_0) \cdot exp(-\alpha X z) + \frac{\zeta \cos\theta\, B}{1 - B} exp(-\alpha X \cdot 2R_C)\right] \end{gathered} \tag{119}$$

4.4.2 Estimation of Biomass Concentration

The value of the biomass, X, was measured using an optical density (OD) correlation for the July assay (2 points) and via dry cell weight for the August assay (4 points).

Using the measured points, simple growth models were applied: an exponential model for the July assay and a Monod model for the August assay.

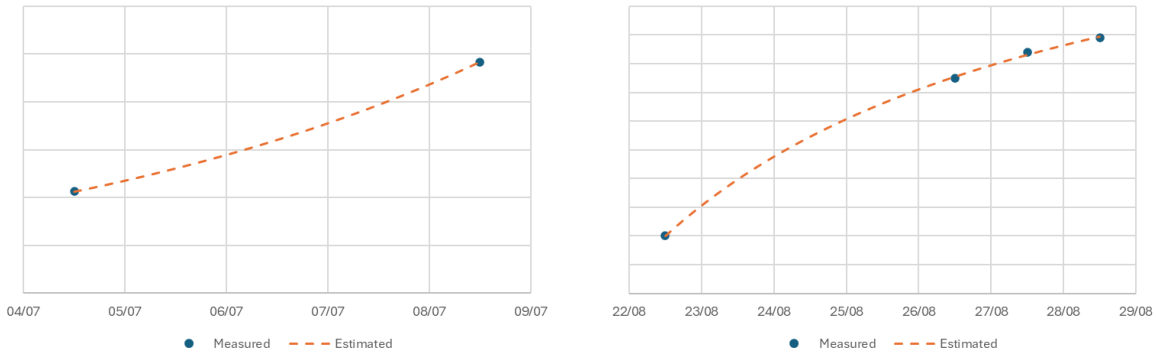

(a) (b)

Figure 25: Estimated biomass concentrations for the July assay (a) and the August assay (b).

4.4.3 Adaptation of the Fernández Model

To verify the model and compare it with the existing literature, the path length was also calculated via the Fernández model [108]. The following are the adaptations and simplifications made to the model.

The path length z is given by Equation 120.

$$z = \frac{R\ sin\ \varepsilon - r_i\ sin\ \rho}{cos\ \theta} \tag{120}$$

where ε is the penetration angle of the sun ray, r_i is the radius of a point in polar coordinates, ρ is the angle of a point in polar coordinates, and θ is the zenith angle.

As only the direct path from one defined point is of interest, the location of Sensor C, r_i is equal to the radius of the reactor, and ρ is the angle of Sensor C in relation to the origin in the coordinates of the reactor (3π/2 rad or 270 degrees).

The penetration angle ε is calculated via Equation 121.

$$tan\ \gamma = \frac{r_i\ cos\ \rho - R\ cos\ \varepsilon}{R\ sin\ \varepsilon - r_i\ sin\ \rho} \tag{121}$$

where γ is the projection of θ on the plane parallel to the solar plane, which is calculated via Equation 122.

$$tan\ \gamma = tan\ \theta\ sin\ \omega \tag{122}$$

where ω is the solar hour angle.

For most points in the circle Equation 27 requires iteration to determine the value of ε. However, since Sensor C is assumed to be outside the reactor, r_i is equal to R_c. Therefore, Equation 121 simplifies to Equation 123 (using the sum-to-product trigonometric identities).

$$tan\,\gamma = \frac{R\,(cos\,\rho - cos\,\varepsilon)}{R\;(sin\,\varepsilon - sin\,\rho)} \leftrightarrow tan\,\gamma = \frac{cos\,\rho - cos\,\varepsilon}{sin\,\varepsilon - sin\,\rho} \leftrightarrow$$

$$tan\,\gamma = \frac{-2\,sin\left(\frac{\rho+\varepsilon}{2}\right)sin\left(\frac{\rho-\varepsilon}{2}\right)}{2\,sin\left(\frac{\rho-\varepsilon}{2}\right)cos\left(\frac{\rho+\varepsilon}{2}\right)} \leftrightarrow tan\,\gamma = -tan\left(\frac{\rho+\varepsilon}{2}\right) \qquad (123)$$

$$\leftrightarrow \frac{\rho+\varepsilon}{2} = tan^{-1}(-\,tan\,\gamma) \leftrightarrow \varepsilon = -2\,tan^{-1}(tan\,\gamma) - \rho$$

Combining Equation 123 with Equation 122, the final equation for the value of ε is obtained.

$$\varepsilon = -2\,tan^{-1}(tan\,\theta\,sin\,\omega) - \rho \qquad (124)$$

4.5 Results & Discussion

Figure 26 shows the raw values of illuminance measured by sensors A and C on both experiments.

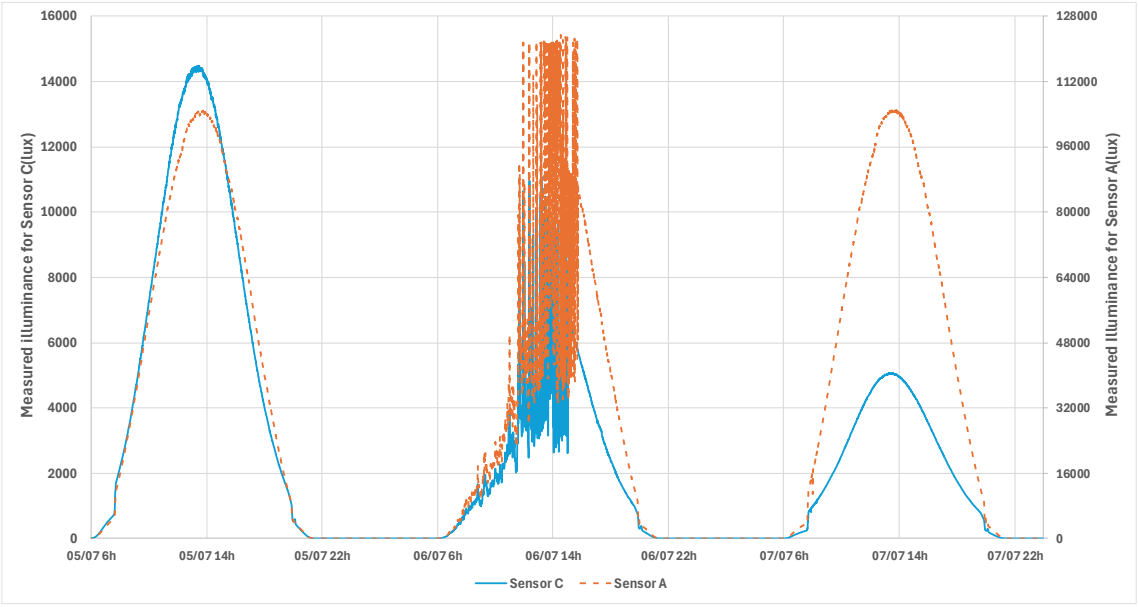

(a)

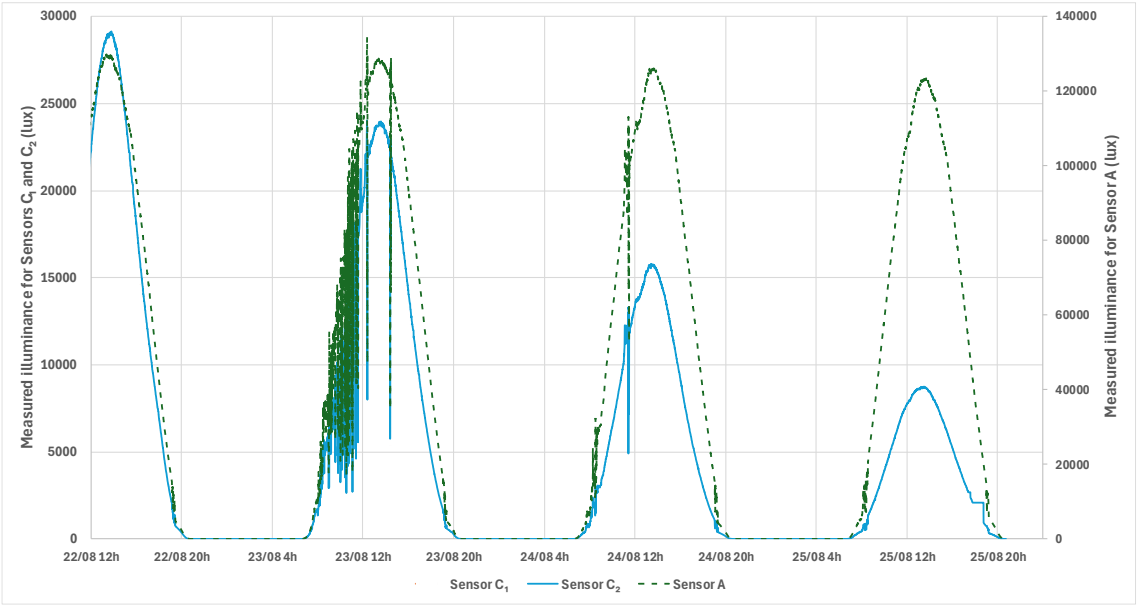

(b)

Figure 26: Calibrated illuminance measured by each sensor (A and C) on each experiment: (a) July assay and (b) August assay). Sensor A is read on the right vertical axis.

On Figure 26 (more visible on a)), the exact moment when the sensors are exposed to direct sunlight during sunrise and later during sunset can be seen as a “jump” in the illuminance. As an example, on July 5th, these values are at 7:42h and 19:52h. These occur later and earlier than the

theoretical values for sunrise and sunset for this day (6:17h and 21:04h) [150] due to objects (including trees) surrounding the reactor and possibly also to the structure of the sensor itself. The solar noon (the point where the illumination is the highest) as measured by Sensor A is consistently the same for every day in both assays, at around 13:44h, which is almost precisely the theoretical solar noon value (13:41h). However, the maximum values for sensor C on all days on both assays is consistently earlier than the solar noon. As an example, on July 5th it occurs at 13:18h, and for August 25th, it happens at around 13:26h.

On some days (chiefly July 6th and August 25th), high clouds were observed throughout the day, blocking out the sun, which affected the measurements of all sensors. For this reason, these measurements are subject to significant fluctuations and become inadequate to be used for the calibration of the model.

Figure 27 shows the predicted and measured values for Sensor C, calculated via Equation 119. E_a and ζ were the only free parameters, and were calculated using minimum squares based exclusively on the data for the first day of each assay. The values for E_a and ζ were 61.40 $m^2\,g^{-1}$ and 2.44 for the July assay, and 125.18 $m^2\,g^{-1}$ and 0 for the August assay, respectively.

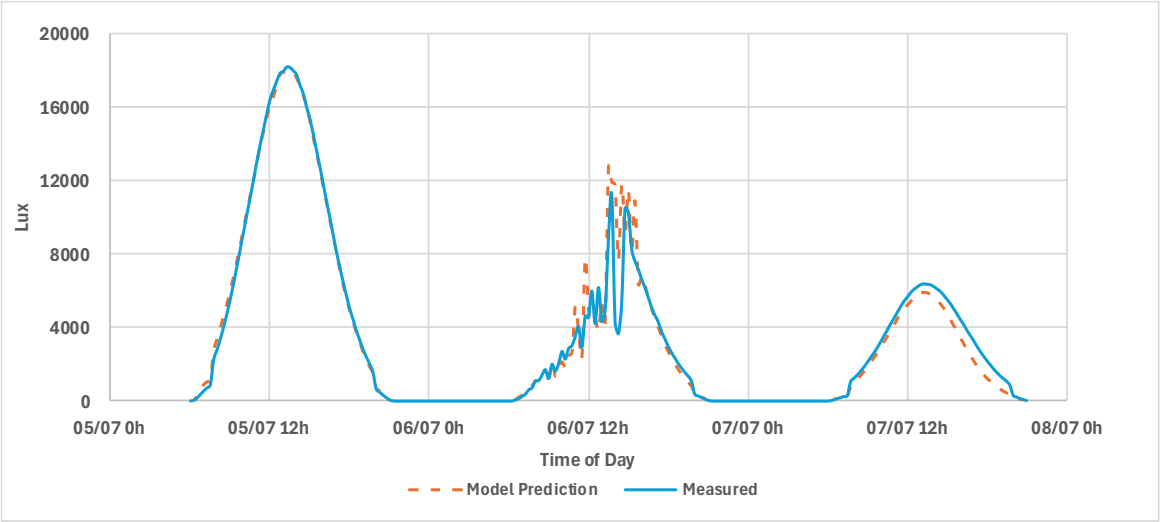

(a)

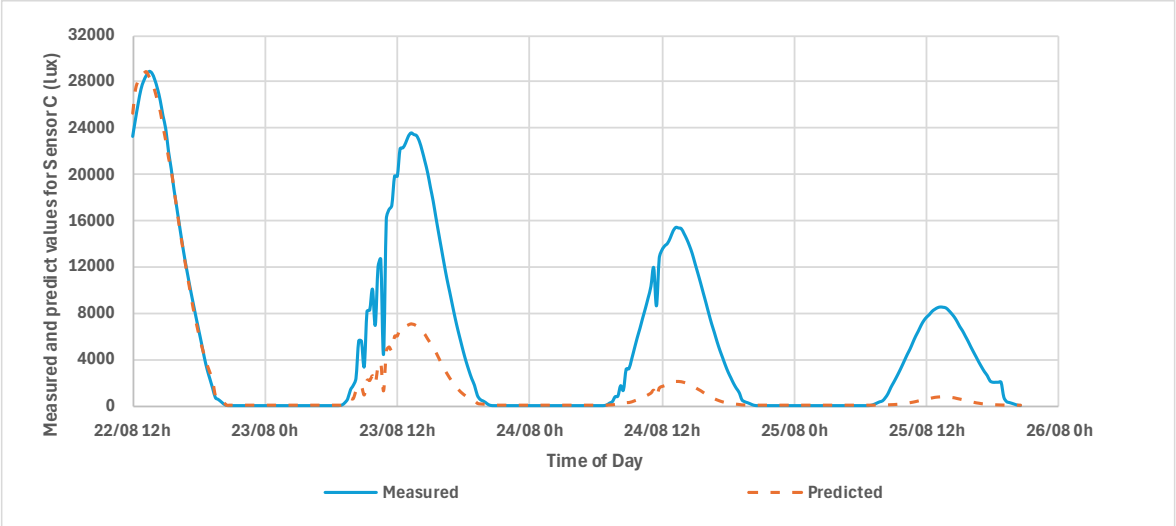

(b)

Figure 27: Measured and predicted values for Sensor C for both assays. a) July assay b) August assay. The values of α and ζ were adjusted to best fit the data of the first day of each assay.

Using MS Excel's RSQ function, it is possible to obtain the Pearson correlation coefficient between the experimental data and the theoretical data. The values for each assay were 96.6 % and 64.9 %, respectively.

As can be seen from the July assay, the predicted and measured values for Sensor C line up remarkably well, even for the days not used to calibrate the value of α and ζ. This suggests that Equation 119 is valid for the prediction of the value observed by Sensor C and, thus, that the model proposed in this work can accurately capture the effects of light attenuation inside the reactor. Even more notable is the fact that the shift in the maximum solar insolation detected by Sensor C is also captured by the model intrinsically, which further corroborates the validity of Equation 119.

It is important to note that on July 7th, there is a slight discrepancy between the graphs during the latter half of the day, which could be due to several factors, namely a change in the color or composition of the microalgae, which can cause the value of α to change.

On the other hand, the predicted values for the August assay do not match the measured values for any day after the first day (used to adjust the two parameters). This is likely because the change in composition of the microalgae (as it accumulates starch) is what drives the increase in dry cell weight, rather than an increase in the number of particles, as is assumed by the Lambert-Beer law. The value of ζ is also adjusted to 0, which suggests that diffuse light does not affect the values measured by Sensor C.

A much better adjustment to the latter days can be obtained by using them exclusively for the adjustment. This is shown in Figure 28. The determined value for E_a was 66.35 $m^2\,g^{-1}$, with a R^2 of 86.0% for all 4 days, and 96.7% for the latter 3 days.

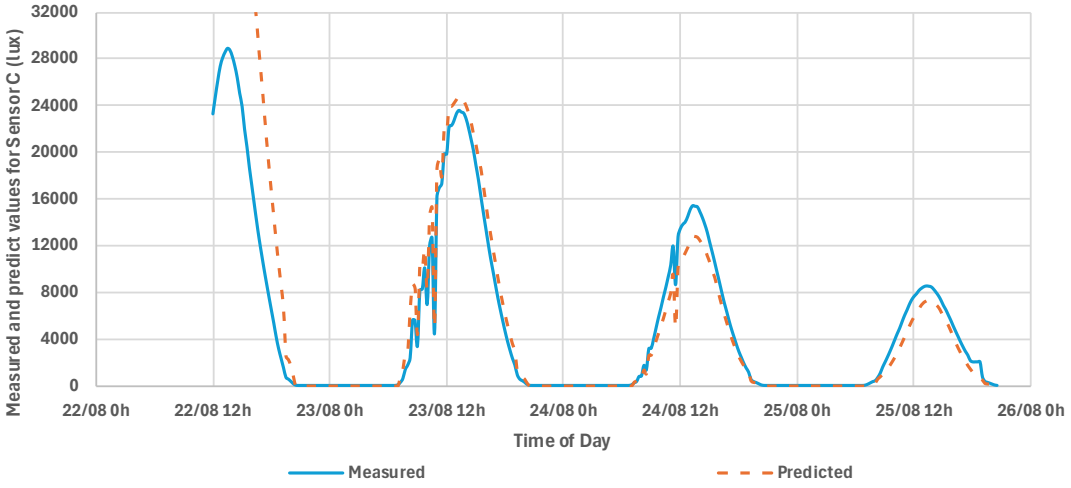

Figure 28: Measured and predicted values for Sensor C for the August assay, using just the latter three days for the adjustment. The value of α was adjusted to best fit the data of the latter three days. The value of ζ was the same as the one used to adjust Figure 27.

To better show the validity of the model in comparison with the available models in the literature, the Fernández model was applied using Equation 119, changing only the value of the path length z and adjusting the value of α using mean squared error, as per the model developed in this paper. The results are found in Figure 29. The value obtained for the Pearson correlation coefficient was 0.2%.

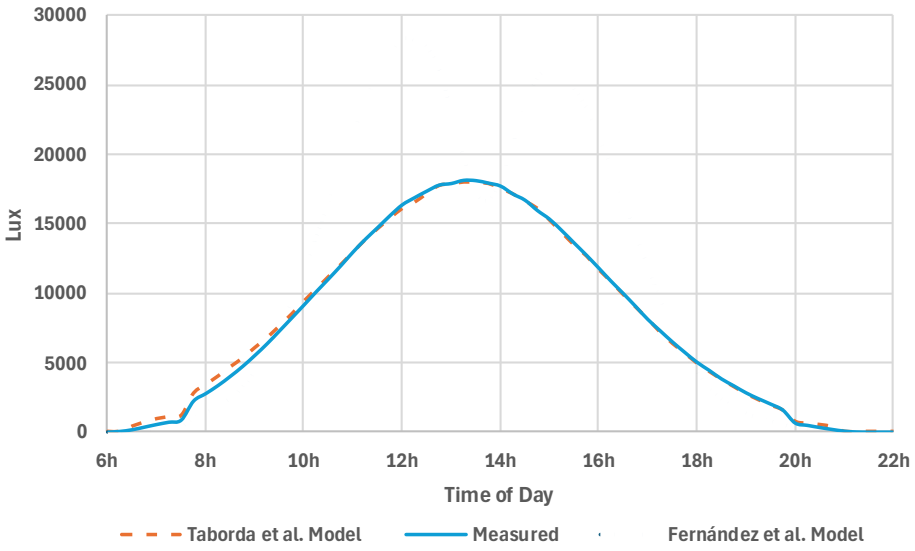

Figure 29: Comparison of the data obtained from Sensor C for July 5th, the predicted value using the model presented in this work, and the value predicted using Fernández' model.

As can be seen in Figure 29, Fernández' model results in a different graph shape, which was not detected by Sensor C, which suggests either the model assumptions or its derivation do not represent the reality occurring in the reactors. This could be due to the Fernández' model assuming the reactor is oriented North-South instead of East-West, which could explain the lower predicted value for Sensor C. This is because, as explained previously, a reactor oriented North-South has the longest path length oriented during the solar maximum.

5 Conclusions

This work sets out to bridge two significant gaps in the modeling of microalgae cultivations: the application of pre-existing models on pilot-scale cultivations, and the construction of a simple and universal model capable of predicting the attenuation of light in an outdoor tubular reactor.

To solve the first gap, four different semi-empirical growth models from the literature were applied to a dataset of ten assays of *Nannochloropsis* sp. with the objective of obtaining a model that would allow the description of the full set of experiments with a single set of kinetic parameters. The development of these models was carried out using a set of training assays to fit the model and a set of validation assays to test the validity of the model.

The results obtained show that a single growth model can be applied to all the different configurations that were tested with adequate predicting capabilities, as shown by the results in the validation set. The fact that well-established models in the literature were applied successfully, and that the results are supported by the validation assays, supports the validity of applying these models to pilot-scale cultivations.

Although most models performed well, overall, it was concluded that the best model among the ones tested is Model H, while Model D, which considers nutrient concentration, performed the worst of all the models. This implies that modeling these systems with the effect of nutrients not only is not needed to explain most of the growth, under the conditions that were used in these cultivations, but can even be a hindrance. Another possibility is that, since nutrients were given in excess, the influence of their effect on growth was minimal.

The necessity of the application of a Lambert-Beer-like term to the incident irradiation to obtain meaningful adjustments to the experimental data is an indication that self-shading cannot be disregarded in moderately dense cultures, and that simple Type I models alone are not able to accurately predict the outcomes of the cultivation.

To solve the second gap, a new model considering light attenuation inside a tubular photobioreactor was derived, and its accuracy was evaluated with an on-field experiment using luximeters. The equation for the light attenuation of a sensor placed on the bottom of a reactor could be used to accurately predict the experimental values measured, which, by proxy, lends support to the validity of the model in general. Furthermore, existing models in the literature do not match the experimental results and are difficult to adapt to the specific reactor conditions of the experiment. The use of this model could provide more accurate values for the average irradiation in

tubular reactors and thus a more accurate prediction of biomass concentration inside those reactors. Furthermore, this model can also be used to optimize reactor assembly itself *a priori*, with reactor orientation and size being two of the input parameters of the model that can be adjusted.

The positive results from this work open the door for the application of Type II models in production reactors, which was until now difficult or impossible with existing literature models. Such models could allow for more accurate reactor modeling, optimization and control, which allows for the lowering of costs and increased efficiency of their operation.

References

[1] M. A. Borowitzka, "Biology of Microalgae," in *Microalgae in health and disease prevention*, Academic Press, 2018, pp. 23-72.

[2] A. Richmond, Handbook of microalgal culture: biotechnology and applied phycology., John Wiley & Sons, 2008.

[3] S. Feng and C. Posten, Microalgae Biotechnology, Springer International Publishing Switzerland, 2016.

[4] F. S. Sing, A. Isdepsky, M. A. Borowitzka and D. M. Lewis, "Pilot-scale continuous recycling of growth medium for the mass culture of a halotolerant Tetraselmis sp. in raceway ponds under increasing salinity: a novel protocol for commercial microalgal biomass production.," *Bioresource technology,* vol. 161, pp. 47-54, 2014.

[5] W. Farooq, W. I. Suh, M. S. Park and J.-W. Yang, "Water use and its recycling in microalgae cultivation for biofuel application," *Bioresource Technology,* vol. 184, pp. 73-81, 2015.

[6] J. A. Lara-Gil, C. Senés-Guerrero and A. Pacheco, "Cement flue gas as a potential source of nutrients during CO2 mitigation by microalgae.," *Algal research,* vol. 17, pp. 285-292, 2016.

[7] W. Y. Cheah, P. L. Show, J.-S. Chang, T. C. Ling and J. C. Juan, "Biosequestration of atmospheric CO2 and flue gas-containing CO2 by microalgae.," *Bioresource technology,* vol. 184, pp. 190-201, 2015.

[8] M. Marsullo, A. Mian, A. V. Ensinas, G. Manente, A. Lazzaretto and F. Marechal, "Dynamic modeling of the microalgae cultivation phase for energy production in open raceway ponds and flat panel photobioreactors," *Frontiers in Energy Research,* vol. 3, 2015.

[9] Q. Béchet, A. Shilton and B. Guieysse, "Modelling the effects of light and temperature on algae growth: Stat of the art and critical cassessment for productivity prediction during outdoor cultivation," *Biotechnology Advances,* 2013.

[10] S. Wahidin, A. Idris, S. Raehanah and M. Shaleh, "The influence of light intensity and photoperiod on the growth and lipid content of microalgae Nannochloropsis sp.," *Bioresource Technology,* vol. 129, pp. 7-11, 2013.

[11] I. Krzemińska, B. Pawlik-Skowrońska, M. Trzcińska and J. Tys, "Influence of photoperiods on the growth rate and biomass," *Bioprocess and Biosystems Engineering,* vol. 37, p. 735–741, 2014.

[12] P. Slegers, "Design scenarios for flat panel photobioreactors," *Applied Energy,* no. 88, pp. 3342-3353, 2010.

[13] European Commission, "PHOTOVOLTAIC GEOGRAPHICAL INFORMATION SYSTEM," [Online]. Available: https://re.jrc.ec.europa.eu/pvg_tools/en/#api_5.2. [Accessed 22 2 2024].

[14] C. Holdmann, U. Schmid-Staiger and T. Hirth, "Outdoor microalgae cultivation at different biomass concentrations — Assessment of different daily and seasonal light scenarios by modeling," *Algal Research,* vol. 38, p. 101405, 2019.

[15] M. A. Borowitzka and J. Beardall, "Algal physiology and large-scale outdoor cultures of microalgae," in *The Physiology of Microalgae*, J. A. Raven, Ed., Dordrecht, Springer, 2016, pp. 601-652.

[16] R. F. Weiss, "Weiss, R_F. "Carbon dioxide in water and seawater: the solubility of a non-ideal gas." Marine chemistry 2.3 (1974): 203-215.," *Marine chemistry,* vol. 2, no. 3, pp. 203-215, 1974.

[17] Engineering ToolBox, "Solubility of Gases in Water vs. Temperature," 2008. [Online]. Available: https://www.engineeringtoolbox.com/gases-solubility-water-d_1148.html. [Accessed 12 2 2025].

[18] H. J. Choi and S. M. Lee, "Effect of temperature, light intensity and pH on the growth rate of Chlorella vulgaris.," *Journal of Korean Society of Environmental Engineers,* vol. 33, no. 7, pp. 511-515, 2011.

[19] J. Marchetti, G. Bougaran, L. Le Dean, C. Megrier, E. Lukomska, R. Kaas, E. Olivo, R. Baron, R. Robert and J.-P. Cadoret, "Optimizing conditions for the continuous culture

of Isochrysis affinis galbana relevant to commercial hatcheries.," *Aquaculture,* vol. 326, p. Cadoret, 2012.

[20] M. L. Bartley, W. J. Boeing, D. Dani, B. N. Dungan and T. Schaub, "Optimization of environmental parameters for Nannochloropsis salina growth and lipid content using the response surface method and invading organisms.," *Journal of applied phycology,* vol. 28, pp. 15-24, 2016.

[21] K. H. Ogbonda, R. E. Aminigo and G. O. Abu, "Influence of temperature and pH on biomass production and protein biosynthesis in a putative Spirulina sp.," *Bioresource technology,* vol. 98, no. 11, pp. 2207-2211, 2007.

[22] Y. H. Ahmadabad, T. A. Liaghat, T. Sohrabi and A. Pourbabaei, "Effect of different salinity, temperature and pH levels on the growth of Dunaliella Salina Algae isolated from Lake Urmia.," *Journal of Fisheries ,* vol. 74, no. 4, pp. 557-573, 2021.

[23] B. J. Boruff, N. R. Moheimani and M. A. Borowitzka, "Identifying locations for large-scale microalgae cultivation in Western Australia: A GIS approach," *Applied Energy,* vol. 149, pp. 379-391, 2015.

[24] J. González-Hernández, J. L. Guzmán, J. C. M. Úbeda and F. G. Acién, "A graphical simulation tool to estimate microalgae production capacity around the world," *Algal Research,* vol. 83, p. 103665, 2024.

[25] F. Acién, E. Molina, A. Reis, G. Torzillo, G. Zittelli, C. Sepúlveda and J. Masojídek, "Photobioreactors for the production of microalgae," *Microalgae-Based Biofuels and Bioproducts.,* 2017.

[26] M. Płaczek, A. Patyna and S. Witczak, "Technical evaluation of photobioreactors for microalgae cultivation.," in *E3S web of conferences.*, vol. 19, EDP Sciences, 2017, p. 02032.

[27] J. Legrand, A. Artub and . J. Pruvosta, "A review on photobioreactor design and modelling for microalgae production," *Reaction Chemistry & Engineering,* 2021.

[28] S. C. Singh, "Basics of light emitting diodes, characterizations and applications.," in *Handbook of Light Emitting and Schottky Diode Research*, Science, 2009.

[29] D. Poelman, J. E. Van Haecke and P. . F. Smet, "Advances in Sulfide Phosphors for Displays and Lighting," *Journal of Materials Science: Materials in Electronics,* vol. 20, no. 1, pp. 134-138, 2009.

[30] A. French and E. Taylor, An Introduction to Quantum Physics, London: Van Nostrand Reinhold, 1978.

[31] ASTM International, "Standard Tables for Reference Solar Spectral Irradiances: Direct Normal and Hemispherical on 37° Tilted Surface," 14 7 2020. [Online]. Available: https://www.astm.org/g0173-03r12.html. [Accessed 30 1 2022].

[32] B. Assis Pessi, E. Pruvost, A. Talec, A. Sciandra and O. Bernard, "Does temperature shift justify microalgae production under greenhouse?," *Algal Research,* vol. 61, p. 102579, 2021.

[33] P. Hassika, , P. Berbigier and J. M. Bonnefond, "Measurement and modelling of the photosynthetically active radiation transmitted in a canopy of maritime pine," *Annales des sciences forestières,* vol. 54, no. 8, pp. 715-730, 1997.

[34] R. W. Thimijan and R. D. Heins, "Photometric, Radiometric, and Quantum Light Units of Measure: A Review of Procedures for Interconversion," *HortScience,* vol. 18, no. 6, pp. 818-822, 1983.

[35] Quentin Béchet, Andy Shilton, Benoit Guieysse, "Modelling the effects of light and temperature on algae growth: Stat of the art and critical cassessment for productivity prediction during outdoor cultivation," *Biotechnology Advances,* 2013.

[36] Darvehei, Pooya, Parisa A. Bahri, and Navid R. Moheimani., "Model development for the growth of microalgae: A review.," *Renewable and Sustainable Energy Reviews ,* vol. 97, pp. 233-258, 2018.

[37] J. A. Raven, J. E. Kübler and J. Beardall, "Put out the light, and then put out the light.," *Journal of the Marine Biological Association of the United Kingdom,* vol. 80, no. 1, pp. 1-25, 2000.

[38] P. A. Crill, "The photosynthesis-light curve: A simple analog model," *Journal of Theoretical Biology,* vol. 64, no. 3, pp. 503-516, 1977.

[39] F. C. Rubio, F. G. Camacho, J. F. Sevilla, Y. Chisti, and E. M. Grima, "A mechanistic model of photosynthesis in microalgae," *Biotechnology and bioengineering,* vol. 81, no. 4, pp. 459-473, 2003.

[40] S. B. Powles, "Photoinhibition of photosynthesis induced by visible light.," *Annual review of plant physiology,* vol. 35, no. 1, pp. 15-44, 1984.

[41] O. Bernard, F. Mairet and B. Chachuat,, "Modelling of microalgae culture systems with applications to control and optimization," *Microalgae Biotechnology,* pp. 59-87, 2015.

[42] S. Aiba, "Growth kinetics of photosynthetic microorganisms.," in *Microbial reactions*, Berlin, Heidelberg, Springer, 1982, pp. 85-156.

[43] . P. S. Schulze, . L. A. Barreira,, H. G. Pereira, , . J. A. Perales, and ,. J. C. Varela, "Light emitting diodes (LEDs) applied to microalgal production," *Trends in biotechnology,* vol. 32, no. 9, pp. 422-430, 2014.

[44] T. Coward, C. Fuentes-Grünewald, A. Silkina, . D. L. Oatley-Radcliffe, G. Llewellyn and R. W. Lovitt, "Utilising light-emitting diodes of specific narrow wavelengths for the optimization and co-production of multiple high-value compounds in Porphyridium purpureum," *Bioresource Technology,* no. 221, pp. 607-615, 2016.

[45] C. L. Teo, M. Atta, A. Bukhari, M. Taisir, A. . M. Yusuf and A. Idris, "Enhancing growth and lipid production of marine microalgae for biodiesel production via the use of different LED wavelengths," *Bioresource Technology,* no. 162, pp. 38-44, 2014.

[46] H. M. Amaro, F. Pagels, I. l. C. Azevedo, J. Azevedo, I. S. Pinto, F. X. Malcata and A. C. Guedes, "Light-emitting diodes—a plus on microalgae biomass and high-value metabolite production," *Journal of Applied Phycology,* 2020.

[47] A. Vadiveloo, N. R. Moheimani, J. J. Cosgrove, P. A. Bahri and D. Parlevliet, "Effect of different light spectra on the growth and productivity of acclimated Nannochloropsis sp.(Eustigmatophyceae)," *Algal research,* vol. 8, pp. 121-127, 2015.

[48] R. Mohammadjavad, N. R. Moheimani and D. Parlevliet, "Red luminescent solar concentrators to enhance Scenedesmus sp. biomass productivity.," *Algal Research,* vol. 45, p. 101771, 2020.

[49] A. Saccardo, F. Bezzo and E. Sforza, "Microalgae growth in ultra-thin steady-state continuous photobioreactors: assessing self-shading effects," *Frontiers in Bioengineering and Biotechnology,* vol. 10, p. 977429, 2022.

[50] J. Grobbelaar, "The influence of light/dark cycles in mixed algal cultures on their productivity.," *Bioresour Technol,* vol. 38, pp. 189-94, 1991.

[51] H.-P. Luo and M. H. Al-Dahhan, "Analyzing and modeling of photobioreactors by combining first principles of physiology and hydrodynamics.," *Biotechnology and bioengineering,* vol. 85, no. 4, pp. 382-393, 2004.

[52] J. U. Grobbelaar, L. Nedbal and V. Tichý, "Influence of high frequency light/dark fluctuations on photosynthetic characteristics of microalgae photoacclimated to different light intensities and implications for mass algal cultivation.," *Journal of applied phycology,* vol. 8, no. 4, pp. 335-343, 1996.

[53] J. U. Grobbelaar, "Turbulence in mass algal cultures and the role of light/dark fluctuations.," *Journal of Applied Phycology,* vol. 6, pp. 331-335, 1994.

[54] L. Resman, M. B. Zrimec, V. Žitko, B. Lazar, R. Reinhardt, A. Cerar and R. Mihelič, "Microalgae Production on Biogas Digestate in Sub-Alpine Region of Europe—Development of Simple Management Decision Support Tool," *sustainability,* vol. 15, p. 16948, 2023.

[55] H. Ermis, Ü. Güven-Gülha, T. Çakır and M. Altınbaş, "Microalgae growth and diversity in anaerobic digestate compared to synthetic medi," *Biofuel Research Journal,* vol. 33, pp. 1551-1561, 2022.

[56] A. K. Vuppaladadiyam, . P. Prinsen,, . A. Raheem, . R. Luque, and M. Zhao, , "Microalgae cultivation and metabolites production: a comprehensive review," *Biofuels, Bioproducts and Biorefining,* vol. 2, no. 12, pp. 304-324, 2018.

[57] . N. A. Nimer, M. D. Iglesias-Rodriguez and M. J. Merrett, "Bicarbonate utilization by marine phytoplankton species," *Journal of Phycology,* vol. 33, no. 4, pp. 625-631., 1997.

[58] P. Darvehei, P. A. Bahri and N. R. Moheimani, "Model development for the growth of microalgae: A review.," *Renewable and Sustainable Energy Reviews,* vol. 97, pp. 233-258, 2018.

[59] M. A. Borowitzka, "Algal Physiology and Large-Scale Outdoor Cultures of Microalgae," in *The Physiology of Microalgae*, M. A. Borowitzka, J. A. Raven and J. Beardall, Eds., Springer Cham, 2016, pp. 601-654.

[60] A. Kazbar, G. Cogne, B. Urbain, H. Marec, B. Le-Gouic, J. Tallec, H. Takache, A. Ismail and J. Pruvost, "Effect of dissolved oxygen concentration on microalgal culture in photobioreactors.," *Algal Research,* vol. 39, p. 101432, 2019.

[61] S. Gao, S. Edmundson and M. Huesemann, "Oxygen stress mitigation for microalgal biomass productivity improvement in outdoor raceway ponds," *Algal Research,* vol. 68, p. 102901, 2022.

[62] Q. Béchet, A. Shilton and B. Guieysse, "Modelling the effects of light and temperature on algae growth: Stat of the art and critical cassessment for productivity prediction during outdoor cultivation," *Biotechnology Advances,* 2013.

[63] B. Carli, "Basics about radiative transfer," 2007. [Online]. Available: https://earth.esa.int/dragon/D2_L2_Carli.pdf. [Accessed 2 3 2022].

[64] . J.-F. Cornet, C. G. Dussap, J.-B. Gros and . C. Binois, "A simplified monodimensional approach for modeling coupling between radiant light transfer and growth kinetics in photobioreactors.," *Chemical Engineering Science,* vol. 50, no. 9, pp. 1489-1500, 1995.

[65] L. Pottier, ,. J. Pruvost, ,. J. Deremetz and J. Legr, "A fully predictive model for one-dimensional light attenuation by Chlamydomonas reinhardtii in a torus photobioreactor.," *Biotechnology and Bioengineering,,* vol. 91, no. 5, pp. 569-582, 2005.

[66] J. F. Cornet and C.-G. Dussap, "A Simple and reliable formula for assessment of maximum volumetric productivities in photobioreactors," *Biocatalysts and Bioreactor Design,* 2009.

[67] Y. S. Yun and J. M. Park, "Kinetic modeling of the light-dependent photosynthetic activity of the green microalga Chlorella vulgaris," *Biotechnol Bioeng,* vol. 83(3), pp. 202-11, 2003.

[68] T. Katsuda, T. Arimoto, K. Igarashi, M. Azuma, J. Kato, S. Takakuwa and H. Ooshima, "Light intensity distribution in the externally illuminated cylindrical photo-bioreactor and its application to hydrogen production by Rhodobacter capsulatus.," *Biochemical engineering journal,* vol. 5, no. 2, pp. 157-164, 2000.

[69] A. Viruela, S. Aparicio, Á. Roble, L. B. Falomir, J. Serralta, A. Seco and J. Ferrera, "Kinetic modeling of autotrophic microalgae mainline processes for sewage treatment in phosphorus-replete and -deplete culture conditions," *Science of the Total Environment,* vol. 797, pp. 149-165, 2021.

[70] ,. I. A. Fernández, . F. G. Fernández, J. J. Magán, J. L. Guzmán and M. Berenguel, "Dynamic model of microalgal production in tubular photobioreactors.," *Bioresource technology,* vol. 126, pp. 172-181, 2012.

[71] F. G. Acién Fernández, F. García Camacho, J. A. Sánchez Pérez and . J. M. Fern, "A Model for Light Distribution and Average Solar Irradiance Inside Outdoor Tubular Photobioreactors for the Microalgal Mass Culture," *Biotechnology and Bioengineering,* vol. 55, no. 5, pp. 701-714, 1997.

[72] H. Tamiya, ,. Hase, K. Shibata, , ,. Mituya and . T. .Iwamura, "Kinetics of growth of Chlorella, with special reference to its dependence on quantity of available light and on temperature.," in *Algal culture from laboratory to pilot plant*, Washington D.C., Carnegie Institution of Washington, 1953, pp. 204-32.

[73] H. Y. Lee, L. E. Erickson and S. S. Yang, "Kinetics and bioenergetics of light-limited photoautotrophic growth of Spirulina platensis.," *Biotechnology and Bioengineering,* vol. 29, no. 7, pp. 832-843, 1987.

[74] A. Franz, F. Lehr, C. Posten and G. Schaub, "Modeling microalgae cultivation productivities in different geographic locations–estimation method for idealized photobioreactors.," *Biotechnology Journal,* vol. 7, no. 4, pp. 546-557, 2012.

[75] E. M. Grima, M. F. Sevilla and J. Sánchez, "A study on simultaneous photolimitation and photoinhibition in dense microalgal cultures taking into account incident and averaged irradiances.," *Journal of Biotechnology,* vol. 45, no. 1, pp. 59-69, 1996.

[76] E. A. Laws and M. S. Chalup, "A test of the assumptions and predictions of recent microalgal growth models with the marine phytoplankter Pavlova lutheri.," *Limnology and Oceanography,* vol. 35, no. 3, pp. 583-596, 1990.

[77] Y.-C. Jeon, C.-W. Cho and Y.-S. Yun, "Measurement of microalgal photosynthetic activity depending on light intensity and quality.," *Biochemical Engineering Journal,* vol. 27, no. 2, pp. 127-131, 2005.

[78] S. L. Emil , "Photosynthesis in relation to light and carbon dioxide.," *Proceedings of the National Academy of Sciences of the United States of America,* vol. 22, no. 8, p. 504, 1936.

[79] F. F. Blackman, "Optima and Limiting Factors," *Annals of Botany,* vol. 19, no. 74, pp. 281-295, 1905.

[80] T. F. Bannister, "Quantitative description of steady state, nutrient-saturated algal growth, including adaptation.," *Limnology and Oceanography,* vol. 24, no. 1, pp. 76-96, 1979.

[81] E. Molina Grima, S. Pérez, J. Garcia Camacho, . J. S. García and D. A. López, "n-3 PUFA productivity in chemostat cultures of microalgae," *Applied Microbiology and Biotechnology,* vol. 38, no. 5, pp. 599-605, 1993.

[82] A. K. Pegallapati and N. Nirmalakhandan, "Modeling algal growth in bubble columns under sparging with CO2-enriched air.," *Bioresource Technology,* vol. 124, pp. 137-145, 2012.

[83] . I. A. Fernández, F. G. Guzmán, M. Berenguel and J. L. Mendoza, "Dynamic model of an industrial raceway reactor for microalgae production.," *Algal Research,* vol. 17, pp. 67-78, 2016.

[84] A. E. Rabe, and . R. J. Benoit., "Mean light intensity—a useful concept in correlating growth rates of dense cultures of microalgae.," *Biotechnology and Bioengineering,* vol. 4, no. 4, pp. 377-390, 1962.

[85] S. ,. Meseck, J. . H. Alix and G. H. Wikfors, "Photoperiod and light intensity effects on growth and utilization of nutrients by the aquaculture feed microalga, Tetraselmis chui (PLY429).," *Aquaculture,* vol. 246, no. 1-4, pp. 393-404, 2005.

[86] . B. ,. Chalker, "Modeling light saturation curves for photosynthesis: an exponential function.," *Journal of Theoretical Biology,* vol. 84, no. 2, pp. 205-215, 1980.

[87] T. A. Costache, . F. G. Acien Fernandez, M. M. Morales, J. M. Fernández-Sevilla, I. Stamatin and E. Molina,, "Comprehensive model of microalgae photosynthesis rate as a function of culture conditions in photobioreactors.," *Applied microbiology and biotechnology,* vol. 97, no. 17, pp. 7627-7637, 2013.

[88] R. O. Megard, , . D. W. Tonkyn and W. H. Senft, "Kinetics of oxygenic photosynthesis in planktonic algae.," *Journal of Plankton Research,* vol. 6, no. 2, pp. 325-337, 1984.

[89] S. Fouchard, J. Pruvost, B. Degrenne, M. Titica and J. Legrand, "Kinetic modeling of light limitation and sulfur deprivation effects in the induction of hydrogen production with Chlamydomonas reinhardtii: Part I. Model development and parameter identification.," *Biotechnology and bioengineering,* vol. 102, no. 1, pp. 232-245, 2009.

[90] J. Pruvost, L. Pottier and J. Legrand, "Numerical investigation of hydrodynamic and mixing conditions in a torus photobioreactor.," *Chemical Engineering Science,* vol. 61, no. 14, pp. 4476-4489, 2006.

[91] D. Ippoliti, C. Gómez, M. d. M. Morales-Amaral, R. Pistocchi, J. M. Fernández-Sevilla and F. G. Acién, "Modeling of photosynthesis and respiration rate for Isochrysis galbana (T-Iso) and its influence on the production of this strain.," *Bioresource Technology,* vol. 203, pp. 71-79, 2016.

[92] A. Concas, M. Pisu and C. Giacomo, "A novel mathematical model to simulate the size-structured growth of microalgae strains dividing by multiple fission.," *Chemical Engineering Journal,* vol. 287, pp. 252-268, 2016.

[93] M. Mirzaie, M. Kalbasi, B. Ghobadian and S. M. Mousavi., "Kinetic modeling of mixotrophic growth of Chlorella vulgaris as a new feedstock for biolubricant.," *Journal of Applied Phycology,* vol. 28, no. 5, pp. 2707-2717, 2016.

[94] J. C. H. Peeters and P. Eilers, "The relationship between light intensity and photosynthesis—a simple mathematical model.," *Hydrobiological Bulletin,* vol. 12, no. 2, pp. 134-136, 1978.

[95] A. Dauta, J. Devaux, F. Piquemal and L. Boumnich, "Growth rate of four freshwater algae in relation to light and temperature.," *Hydrobiologia,* vol. 207, no. 1, pp. 221-226, 1990.

[96] O. Bernard and B. Rémond, "Validation of a simple model accounting for light and temperature effect on microalgal growth.," *Bioresource Technology,* vol. 123, pp. 520-527, 2012.

[97] . J. M. Sandnes, T. Källqvist, T, D. Wenner and H. R. Gislerød, "Combined influence of light and temperature on growth rates of Nannochloropsis oceanica: linking cellular responses to large-scale biomass production," *Journal of Applied Phycology,* vol. 17, pp. 515-525, 2005.

[98] J. H. Steele, "Environmental control of photosynthesis in the sea.," *Limnology and Oceanography,* vol. 7, no. 2, pp. 137-150, 1962.

[99] D. Baquerisse, S. Nouals, A. Isambert, P. F. d. Santos and G. Durand, "Modelling of a continuous pilot photobioreactor for microalgae production.," *Progress in Industrial Microbiology,* vol. 35, pp. 335-342, 1999.

[100] Luo, H. P., & Al-Dahhan, M. H., "Analyzing and modeling of photobioreactors by combining first principles of physiology and hydrodynamics," *Biotechnology and bioengineering,* vol. 85(4), pp. 382-393, 2004.

[101] J. Monod, "The growth of bacterial cultures.," *Annual review of microbiology,* vol. 3, no. 1, pp. 371-394, 1949.

[102] J. Haldane, Enzymes, London: Longmans Green, 1930.

[103] J. F. Andrews, "A mathematical model for the continuous culture of microorganisms utilizing inhibitory substrates.," *Biotechnology and bioengineering,* vol. 10, no. 6, pp. 707-723, 1968.

[104] P. H. C. Eilers and J. C. H. Peeters, "A model for the relationship between light intensity and the rate of photosynthesis in phytoplankton," *Ecological modelling,* vol. 42, no. 3-4, pp. 199-215, 1988.

[105] H. J. Rehm, G. Reed, . A. Puhler and ,. P. Stadler, Biotechnology Second, Completely Revised Edition, 1995.

[106] E. Krichen, ,. Rapaport, and E. Le Floc'h, Er, "A new kinetics model to predict the growth of micro-algae subjected to fluctuating availability of light," *Algal Research,* vol. 58, p. 102362, 2021.

[107] D. Demory, C. Combe, P. Hartmann, A. Talec, E. Pruvost, R. Hamouda, F. Souillé, P.-O. Lamare, M.-O. Bristeau, J. Sainte-Marie, S. Rabouille, F. Mairet, A. Sciandra and O. Bernard, "How do microalgae perceive light in a high-rate pond? Towards more realistic Lagrangian experiments," *Royal Society Open Science,* vol. 5, p. 180523, 2018.

[108] F. G. Acién Fernández, F. García Camacho, J. A. Sánchez Pérez, J. M. Fernández Sevilla and E. Molina Grima, "A Model for Light Distribution and Average Solar Irradiance Inside Outdoor Tubular Photobioreactors for the Microalgal Mass Culture," *Biotechnology and bioengineering,* vol. 55, no. 5, pp. 701-714, 1997.

[109] F. García-Camacho, A. Sánchez-Mirón, E. Molina-Grima, F. Camacho-Rubio and J. C. Merchuck, "A mechanistic model of photosynthesis in microalgae including photoacclimation dynamics," *Journal of Theoretical Biology,* vol. 304, pp. 1-15, 2012.

[110] R. Laifa, J. Morchain, L. Barna and P. Guiraud, "A numerical framework to predict the performances of a tubular photobioreactor from operating and sunlight conditions," *Algal Research,* vol. 60, p. 102550, 2021.

[111] A. Solimeno, R. Samsó, E. Uggett, B. Sialve, J.-P. Steyer, A. Gabarró and J. Garcia, "New mechanistic model to simulate microalgae growth," *Algal Research,* vol. 12, pp. 350-358, 2015.

[112] J. W. Haefner, Modeling biological systems: principles and applications., New York: Springer Science & Business Media, 2005.

[113] L. Eunyoung , M. Jalalizadeh and Q. Zhang, "Growth kinetic models for microalgae cultivation: A review," *Algal Research,* vol. 12, p. 497–512, 2015.

[114] L. Rosso, . J. R. Lobry and J.-P. Flandrois, "An unexpected correlation between cardinal temperatures of microbial growth highlighted by a new model.," *Journal of Theoretical Biology,* vol. 162, no. 4, pp. 447-463, 1993.

[115] J. R. Lobry, L. Rosso and J. P. Flandrois, , "A FORTRAN subroutine for the determination of parameter confidence limits in non-linear models," *Binary,* vol. 3, pp. 86-93, 1991.

[116] D. A. Ratkowsky, J. Olley, T. A. McMeekin and A. Ball, "Relationship between temperature and growth rate of bacterial cultures.," *Journal of bacteriology,* vol. 149, no. 1, pp. 1-5, 1982.

[117] D. A. Ratkowsky, , . R. . K. Lowry, . T. A. McMeekin, A. N. Stokes and R. Chandler, , "Model for bacterial culture growth rate throughout the entire biokinetic temperature range.," *Journal of bacteriology,* vol. 154, no. 3, pp. 1222-1226, 1983.

[118] J. A. Roels, Energetics and kinetics in biotechnology., Elsevier biomedical press, 1983.

[119] H. Haario, L. Kalachev and M. Laine, "Reduced models of algae growth.," *Bulletin of mathematical biology,* vol. 71, no. 7, pp. 1626-1648, 2009.

[120] L. Xin, H. Hong-Ying, G. Ke and S. Ying-Xue., "Effects of different nitrogen and phosphorus concentrations on the growth, nutrient uptake, and lipid accumulation of a freshwater microalga Scenedesmus sp.," *Bioresource technology,* vol. 101, no. 14, pp. 5494-5500, 2010.

[121] A. Concas, P. Massimo and G. Cao, "Novel simulation model of the solar collector of BIOCOIL photobioreactors for CO2 sequestration with microalgae.," *Chemical Engineering Journal,* vol. 157, no. 2, pp. 297-303, 2010.

[122] L. Travieso, D. O. Hall, K. K. Rao, . F. .Benıtez and R. Borja, "A helical tubular photobioreactor producing Spirulina in a semicontinuous mode.," *International Biodeterioration & Biodegradation,* vol. 47, pp. 151-155, 2001.

[123] F. C. D. Nicéia, A. L. d. Chagas, R. Rech and N. R. Marcílio, "Kinetic modeling of Dunaliella tertiolecta growth under different nitrogen concentrations.," *Chemical Engineering & Technology,* vol. 39, no. 9, pp. 1716-1722, 2016.

[124] M. Chen, M. Fan, R. Liu, X. Wang, X. Yuan and H. Zhu, "The dynamics of temperature and light on the growth of phytoplankton.," *Journal of Theoretical Biology,* vol. 385, pp. 8-19, 2015.

[125] X.-W. Zhang, F. Chen and J. R. Michael, "Kinetic models for heterotrophic growth of Chlamydomonas reinhardtii in batch and fed-batch cultures.," *Process Biochemistry,* vol. 35, no. 3-4, pp. 385-289, 1999.

[126] S. Kasiri, A. Ulrich and V. Prasad, "Kinetic modeling and optimization of carbon dioxide using microalgae cultivated in oil-sands process water," *Chemical Engineering Science,* vol. 137, p. 697–711, 2015.

[127] D. E. Burmaster, "The unsteady continuous culture of phosphate-limited Monochrysis lutheri Droop: experimental and theoretical analysis.," *Journal of experimental marine Biology and Ecology,* vol. 39, no. 2, pp. 167-186, 1979.

[128] A. Packer, Y. Li, T. Andersen, Q. Hu, Y. Kuang and M. Sommerfeld, "Growth and neutral lipid synthesis in green microalgae: a mathematical model.," *Bioresource technology,* vol. 102, no. 1, pp. 111-117, 2011.

[129] H. L. Maclntyre, T. M. Kana and R. J. Geider, "A dynamic regulatory model of phytoplanktonic acclimation to light, nutrients, and temperature.," *Limnology and Oceanography,* vol. 43, no. 4, pp. 679-694, 1998.

[130] J. Caperon and J. Meyer, "Nitrogen-limited growth of marine phytoplankton—I. Changes in population characteristics with steady-state growth rate.," in *Deep Sea Research and Oceanographic Abstracts*, Elsevier, 1972, pp. 601-618.

[131] G. Bougaran, O. Bernard and A. Sciandra, "Modeling continuous cultures of microalgae colimited by nitrogen and phosphorus.," *Journal of theoretical biology,* vol. 265, no. 3, pp. 443-454, 2010.

[132] J. C. Goldman, W. J. Oswald and D. Jenkins, "The kinetics of inorganic carbon limited algal growth," *Journal (Water Pollution Control Federation),* pp. 554-574, 1974.

[133] E. Lee and Q. Zhang, "Integrated co-limitation kinetic model for microalgae growth in anaerobically digested municipal sludge centrate," *Algal research,* no. 18, pp. 15-24, 2016.

[134] R. Filali, . S. Tebbani,, D. Dumur,, A. Isambert, . D. Pareau, and F. Lopes, "Growth modeling of the green microalga Chlorella vulgaris in an air-lift photobioreactor," *IFAC Proceedings Volumes,* vol. 44, no. 1, pp. 10603-10608, 2011.

[135] . J. E. Bailey and D. F. Ollis, Biochemical engineering fundamentals, McGraw-Hill, 2018.

[136] I. C. Tang, , M. R. Okos and S. T. Yang,, "Effects of pH and acetic acid on homoacetic fermentation of lactate by Clostridium formicoaceticum," *Biotechnology and bioengineering,* vol. 8, no. 34, pp. 1063-1074, 1989.

[137] . E. B. Pérez, I. C. Pina and L. P. Rodríguez, "Kinetic model for growth of Phaeodactylum tricornutum in intensive culture photobioreactor," *Biochemical Engineering Journal,,* vol. 40, no. 3, pp. 520-525, 2008.

[138] . S. K. Jayaraman and R. R. Rhinehart, "Modeling and optimization of algae growth," *Industrial & Engineering Chemistry Research,* vol. 54, no. 33, pp. 8063-8071, 2015.

[139] S. Miyachi, S. Izawa and H. Tamiya, "Effect of oxygen on the capacity of carbon dioxide-fixation by green algae," *The Journal of Biochemistry,* vol. 42, no. 3, pp. 221-244, 1955.

[140] A. M. Jamal Alikhani, "Assessment of the endogenous respiration rate and the observed biomass yield for methanol-fed denitrifying bacteria under anoxic and aerobic conditions," *Water Science & Technolog,* vol. 75, no. 1, 2017.

[141] D. Dermoun, D. Chaumont, T. M. Thebault and A. Dauta, "Modelling of growth of Porphyridium cruentum in connection with two interdependent factors: light and temperature.," *Bioresour Technol,* vol. 42, pp. 113-7, 1992.

[142] I. L. Muñoz and O. Bernard, "Modeling the Influence of Temperature, Light Intensity and Oxygen Concentration on Microalgal Growth Rate," *Processes,* vol. 9, no. 3, p. 496, 2021.

[143] A. Nikolaou, P. Hartmann, A. Sciand, B. Chachuat and O. Bernard, "Dynamic coupling of photoacclimation and photoinhibition in a model of microalgae growth," *Journal of Theoretical Biology,* vol. 390, pp. 61-72, 2016.

[144] M. R. Droop, "Vitamin B12 and marine ecology. IV. The kinetics of uptake, growth and inhibition in Monochrysis lutheri.," *Journal of the Marine Biological Association of the United Kingdom,* vol. 48, no. 3, pp. 689-733, 1968.

[145] R. Laifa, J. Morchain, L. Barna and P. Guiraud, "A numerical framework to predict the performances of a tubular photobioreactor from operating and sunlight conditions," *Algal Research,* vol. 60, p. 102550, 2021.

[146] Zhang, Y., Wijeratne, L. O., Talebi, S., & Lary, D. J. , "Machine learning for light sensor calibration.," *Sensors,* vol. 21, no. 18, p. 6259, 2021.

[147] National Oceanic and Atmospheric Administration (NOAA), "General Solar Position Calculations," [Online]. Available: https://gml.noaa.gov/grad/solcalc/solareqns.PDF. [Accessed 3 10 2023].

[148] "RefractiveIndex.info," [Online]. Available: https://refractiveindex.info. [Accessed 20 5 2025].

[149] M. Collares-Pereira and A. Rabl, "The average distribution of solar radiation-correlations between diffuse and hemispherical and between daily and hourly insolation values," *Solar energy,* vol. 22, no. 2, pp. 155-164, 1978.

[150] Time and Date AS, "Time and Date," [Online]. Available: https://www.timeanddate.com/sun/portugal/lisbon. [Accessed 15 1 2025].

[151] B. Carli, "Basics about radiative transfer," [Online]. Available: https://earth.esa.int/dragon/D2_L2_Carli.pdf. [Accessed 2 3 2022].

Appendix A

The dry cell weight (DCW) of the assays was measured indirectly using a correlation with the optical density (OD) of the culture. This correlation for *Nannochloropsis sp.* measured at 750 nm is found in Figure A1.

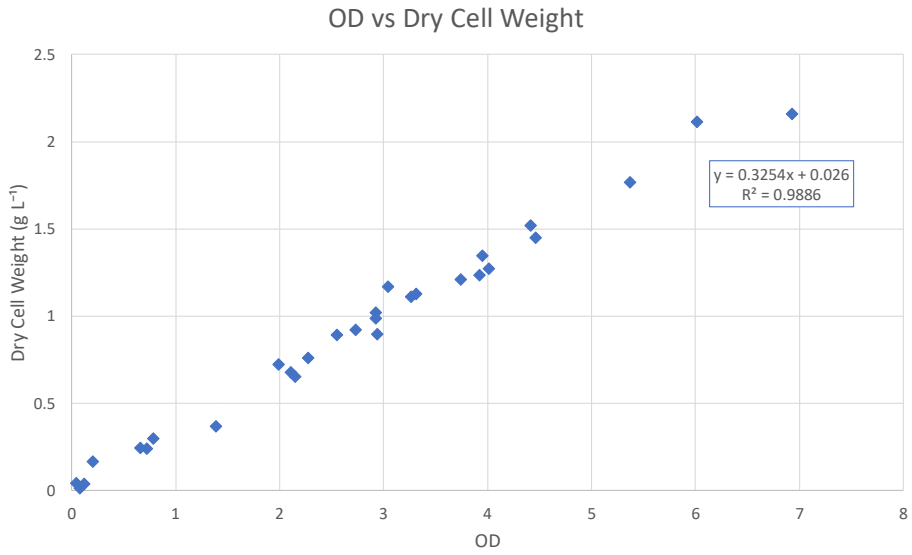

Figure A1. Correlation between measured OD and the dry cell weight for *Nannochloropsis* sp. The adjusted parameters were a slope of 0.3254 ± 0.0067 g L^{-1} and an intercept of 0.026 ± 0.022 g L^{-1}.

The DCW measured to construct this correlation was done using the following protocol. First, three microfiber filters (with a 0.7 µm pore size) are dried and weighed using a moisture balance, with their combined weight being registered (m_i). A certain volume of culture is filtered through each microfiber filter using a vacuum filter, with the filtered volume V being registered. The three filters are then dried and weighed together in the moisture scale (m_f). The dry cell weight (DCW) is given by Equation A1:

$$DCW = \frac{m_f - m_i}{V} \qquad \text{(A1)}$$

Appendix B

Starting from Eilers and Peeters' formula,

$$\mu = \mu_{max}(1+\beta)\frac{2x_I}{x_I^2 + 2\beta x_I + 1} \tag{B1}$$

Replacing 1 + β with a new variable γ, and the variable x_i with I/Iopt:

$$\mu = \mu_{max}\gamma\frac{2\frac{I}{I_{opt}}}{\left(\frac{I}{I_{opt}}\right)^2 + 2(\gamma-1)\frac{I}{I_{opt}} + 1} \leftrightarrow \frac{2\mu_{max}\gamma I}{\frac{I}{I_{opt}}^2 + 2I(\gamma-1) + I_{opt}} \leftrightarrow$$

$$\leftrightarrow \frac{2\mu_{max}\gamma I \cdot I_{opt}}{I^2 + 2\gamma I \cdot I_{opt} - 2I \cdot I_{opt} + I_{opt}^2} \leftrightarrow \frac{2\mu_{max}\gamma I \cdot I_{opt}}{2\gamma I \cdot I_{opt} + \left(I - I_{opt}\right)^2} \leftrightarrow \tag{B2}$$

$$\leftrightarrow \frac{\mu_{max} \cdot k}{k + \left(I - I_{opt}\right)^2}, k = 2\gamma I \cdot I_{opt}$$

Appendix C

The solar zenith angle is given by Equation C1.

$$cos\,\theta = sin\,\eta\ sin\,\delta + cos\,\eta\,cos\,\delta\,cos\,\omega_h \tag{C1}$$

where η represents the latitude, δ the declination of the Sun and ω_h the solar hour angle (all in radians).

The declination of the Sun can be estimated using the Equation C2 (in radians):

$$\begin{aligned}\delta = 0.006918 &- 0.399912cos(FY) + 0.070257sin(FY)\\ &- 0.006758cos(2FY) + 0.000907sin(2FY)\\ &- 0.002697cos(3FY) + 0.00148sin\,(3FY)\end{aligned} \tag{C2}$$

where *FY* is the fractional year (in radians), which can be calculated by:

$$FY = \frac{2\pi}{365}\left(n + \frac{hour - 12}{24}\right) \tag{C3}$$

where *n* is the number of days since the start of the year (January 1st is day 0).

The solar hour angle (ω_h) can be approximated by the following equation (in degrees):

$$\omega_h = \frac{TST}{4} - 180 \tag{C4}$$

where *TST* is the true solar time (in minutes), which can be calculated by Equation A5.

$$TST = mod(hour * 60 + minute + 4\lambda - 60 \cdot TZ + ET, 1440) \tag{C5}$$

where *TZ* is the timezone of the location in relation to the prime meridian, λ is the longitude of the location (in degrees), and *ET* is the equation of time, which is a correction of the difference between apparent solar time and the mean solar time. It can be estimated by Equation C6 (in minutes):

$$\begin{aligned}ET = 229.18 * (&0.000075 + 0.001868cos(FY) - 0.032077sin(FY)\\ &- 0.014615cos(2FY) - 0.040849sin(2FY))\end{aligned} \tag{C6}$$

The solar azimuth angle can be determined by Equation C7.

$$cos\,\varphi = \frac{sin\,\eta\,cos\,\theta - sin\,\delta}{cos\,\eta\,sin\,\theta} \tag{C7}$$

Appendix D

Let T be the point of the surface of the cylinder where the sun ray penetrates, gets refracted, and eventually reaches point P. The angle of penetration β of the sun ray on a cylinder is given by the angle of the sun ray and the cylinder normal at. The sun ray is expressed by the TS line. The cylinder normal N_c is the line that connects T and the projection of this point onto the cylinder axis (point R).

Since T is on the surface, T=($R_c \cos(\gamma)$,T_y, $R_c \sin(\gamma)$), where γ is the angle of T. On the default cylinder orientation, with cylinder axis being the y axis, $R_y=T_y$ and $R_x=R_z=0$, as shown on Figure 17.

The parametric equation for RT is given by:

$$N_C = RT = R + t_1(T - R)$$

$$RT = (0, T_y, 0) + t_{DR}(T_x - 0, T_y - T_y, T_z - 0) \quad \text{(D1)}$$

$$RT = (0, T_y, 0) + t_{DR}(T_x, 0, T_z)$$

The parametric equation for TS is given by:

$$TS = T + t_1(S - T)$$

$$TS = (T_x, T_y, T_z) + t_{DR}(S_x - T_x, S_y - T_y, S_z - T_z) \quad \text{(D2)}$$

Since by definition $S_x \gg T_x$, $S_y \gg T_y$, $S_z \gg T_z$, TS can be approximated by:

$$TS \approx (T_x, T_y, T_z) + t_{DR}(S_x, S_y, S_z) \quad \text{(D3)}$$

Equation A3 shows the equation for the angle between TS and TR.

$$\cos\beta = \frac{\overrightarrow{TS} \cdot \overrightarrow{TR}}{\|TS\| \times \|TR\|} = \frac{S_x T_x + S_y T_y + S_z T_z}{\sqrt{{S_x}^2 + {S_y}^2 + {S_z}^2} \cdot \|TR\|} \quad \text{(D4)}$$

Since by definition $\sqrt{{S_x}^2 + {S_y}^2 + {S_z}^2} = S_{rad}$, and since Point T is on the surface of the cylinder, $||TR||=R_c$, the equation simplifies to:

$$\cos\beta = \frac{S_x T_x + S_z T_z}{S_{rad} \cdot R_c} \quad \text{(D5)}$$

Using the definition of T and S on Equation D5, the equation can be simplified to:

$$cos\,\beta = \frac{S_{rad}\sin\theta\cos\varphi\,R_c\sin\gamma + S_{rad}\cos\theta\,R_c\cos\gamma}{S_{rad}\cdot R_c} \leftrightarrow$$

$$cos\,\beta = \frac{S_{rad}R_c(\sin\theta\cos\varphi\sin\gamma + \cos\theta\cos\gamma)}{S_{rad}\cdot R_c} \leftrightarrow \quad \text{(D6)}$$

$$cos\,\beta = \sin\theta\cos\varphi\sin\gamma + \cos\theta\cos\gamma$$

The path length *z* is equal to the distance between T and P, that is:

$$z = \sqrt{(P_x - R_C\sin\gamma)^2 + \left(P_y - T_y\right)^2 + (P_z - R_C\cos\gamma)^2} \leftrightarrow$$

$$z = \sqrt{(P_x - R_C\sin\gamma)^2 + {T_y}^2 + (P_z - R_C\cos\gamma)^2} \leftrightarrow \quad \text{(D7)}$$

The angle after refraction, *β'*, is the angle between the vectors TP and TR, that is:

$$\cos\beta' = \frac{\overrightarrow{TP}\cdot\overrightarrow{TR}}{\|TP\|\times\|TR\|} = \frac{\overrightarrow{TP}\cdot\overrightarrow{TR}}{z\cdot R_C} \quad \text{(D8)}$$

The parametric equation for TP is given by Equation D9.

$$\overrightarrow{TP} = T + t_1(P - T)$$

$$\overrightarrow{TP} = (T_x, T_y, T_z) + t_{DR}(P_x - T_x, P_y - T_y, P_z - T_z) \quad \text{(D9)}$$

$$\overrightarrow{TP} = (T_x, T_y, T_z) + t_{DR}(P_x - T_x, -T_y, P_z - T_z)$$

The parametric equation for TR is given by Equation D10.

$$\overrightarrow{TP} = T + t_1(R - T)$$

$$\overrightarrow{TP} = (T_x, T_y, T_z) + t_{DR}(R_x - T_x, T_y - T_y, R_z - T_z) \quad \text{(D10)}$$

$$\overrightarrow{TP} = (T_x, T_y, T_z) + t_{DR}(-T_x, 0, -T_z)$$

Substituting the parametric equations of TP and TR in Equation D8 gives:

$$\cos\beta' = \frac{-T_x(P_x - T_x) - T_y\cdot 0 - T_z(P_z - T_z)}{z\cdot R_C} \leftrightarrow$$

$$\leftrightarrow \cos\beta' = \frac{-R_c\sin\gamma\,(P_x - R_c\sin\gamma) - R_c\cos\gamma\,(P_z - R_c\cos\gamma)}{z\cdot R_C} \leftrightarrow \quad \text{(D11)}$$

$$\leftrightarrow \cos\beta' = \frac{-\sin\gamma\,P_x + {R_c}^2\sin^2\gamma - \cos\gamma\,P_z + {R_c}^2\cos^2\gamma}{z} \leftrightarrow$$

$$\leftrightarrow \cos\beta' = \frac{-\sin\gamma\, P_x - \cos\gamma\, P_z + {R_c}^2\,(\cos^2\gamma + \sin^2\gamma)}{z} \leftrightarrow$$

$$\leftrightarrow \cos\beta' = \frac{{R_c}^2 - \sin\gamma\, P_x - \cos\gamma\, P_z}{z}$$

Finally, the refraction must happen on the plane SPR containing P, R and S. The equation of a plane in 3D cartesian coordinates.

$$\begin{gathered} a(x - x_0) + b(y - y_0) + c(z - z_0) = 0 \leftrightarrow \\ \leftrightarrow ax + by + cz = ax_0 + by_0 + cz_0 \end{gathered} \tag{D12}$$

where N=(a,b,c) is the normal vector for the plane, and x_0,y_0,z_0 being a point in the plane. Using R as this point, x_0 and z_0 being equal to 0. The normal vector can be calculated via the cross product of two vectors in the plane. Using RS and RP:

$$\begin{gathered} \vec{N} = \overrightarrow{RS} \times \overrightarrow{RP} \leftrightarrow \\ \vec{N} = (S_x - T_x, S_y - T_y, S_z - T_z) \times (P_x - T_x, P_y - T_y, P_z - T_z) \leftrightarrow \\ \vec{N} = (S_x, S_y - T_y, S_z) \times (P_x, -T_y, P_z) \leftrightarrow \\ \vec{N} = \left[\left(S_y - T_y\right)P_z - T_y S_z, S_x P_z - S_z P_x, -T_y\, S_x - P_x\left(S_y - T_y\right)\right] \end{gathered} \tag{D13}$$

The final equation for the plane of refraction SRP is therefore:

$$\begin{gathered} \left(\left(S_y - T_y\right)P_z - T_y S_z\right)x + \ (S_x P_z - S_z P_x)y - \left(T_y\, S_x + P_x\left(S_y - T_y\right)\right)z \\ = \ (S_x P_z - S_z P_x)T_y \end{gathered} \tag{D14}$$

Joining Equations D6, D7, D11, D15, together with Snell's law gives the system of equations necessary to calculate the path length *z*, the angle of penetration *β*, the angle of refraction *β'*, and the polar coordinates of the point of penetration T (*γ* and T_y):

$$\begin{cases} cos\,\beta = \ \sin\theta\cos\varphi\sin\gamma + \cos\theta\cos\gamma \\ \cos\beta' = \dfrac{{R_c}^2 - \sin\gamma\, P_x - \cos\gamma\, P_z}{z} \\ z = \sqrt{(P_x - R_C\sin\gamma)^2 + {T_y}^2 + (P_z - R_C\cos\gamma)^2} \\ \sin\beta' = \sin\beta\,\dfrac{n_1}{n_2} \\ ax + \ by + cz = \ bT_y \end{cases} \tag{D15}$$

$$a = \left(S_y - T_y\right)P_z + T_y S_z$$

$$b = S_x P_z - S_z P_x$$

$$c = -T_y S_x - P_x(S_y - T_y)$$

Appendix E

This appendix contains the raw data used in the calibration of the six sensors used in the experiment. The sensors are numbered sequentially from 1 to 6. Table E1 shows the raw data used in the calibration, while Figure E1 plots this data in a graph in logarithmic scale.

Table E1: Raw data from the sensors used in the experiment and the portable luximeter used in their calibration. All values are in lux.

Luximeter Measurement	S1	S2	S3	S4	S5	S6
0	0	0	0	0		
6	11	12	12	12		
22	10	10	10	10		
32					25	27
150	115	144	175	198		
360	298	297	280	286		
723	498	508	502	529		
620	535	546	534	543		
1223	1012	1033	1051	1027		
1810	1477	1507	1474	1500		
2420	1934	1974	1930	1965		
3030	2384	2434	2380	2425		
3635	2829	2888	2824	2877		
4229	3271	3340	3265	3327		
4817	3707	3785	3700	3771		
5401	4139	4226	4132	4313		
5500					2897	2878
5986	4572	4668	4532	4618		
6971	6372	6456	6207	6277		
8683	7875	7991	7704	7770	5017	4827
12070	10902	11040	10620	10744		
16840	15066	15269	14702	14825		
23580	16054	16217	17178	17771		
64500					45789	44007
79100	63270	64870	60630	62701		
88630	76828	76934	73672	75527		
98900					73328	71483
100000	76828	80692	77711	77284		

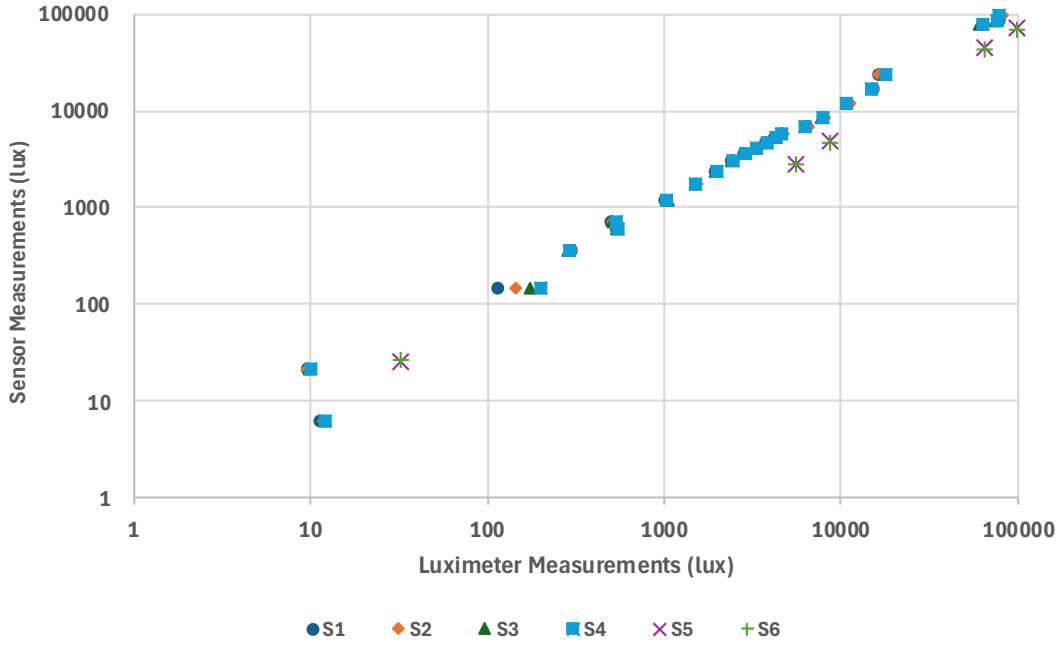

Figure E1: Calibration of the six sensors used in this experiment. The axis are in logarithmic scale.

The values for the sensor calibration were obtained using MS Excel's LINEST function and setting the intercept was set to 0. Table E2 shows the obtained calibration values, the value for the coefficient of determination (R^2), and the position of the sensor on each of the two assays.

Table E2: Calibration for each of the used sensors, the coefficient of determination, and the position of each sensor on each assay.

Sensor	Calibration (lux/lux)	R^2 (%)	Position in July assay	Position in August assay
S1	1.234	99.66	A	-
S2	1.204	99.81	B	-
S3	1.260	99.84	C	C_1
S4	1.241	99.79	D	C_2
S5	1.367	99.92	-	D
S6	1.408	99.89	-	A

Appendix F

I_{diffC} is the diffuse radiation coming from all points in the sky that reach Sensor C, that is, it is the integral of the various effects being considered for the direct radiation (Snell's law, Fresnel's law, geometric considerations of the sensor, and Lambert-Beer's law). These are expressed in Equation D1.

$$I_{diff_C} = I_{diff} \cdot \int cos\,\beta'(\theta,\varphi) \cdot \int (1 - R_0(\theta,\varphi)) \cdot \int exp\big(-\alpha X z_{diff}(R,\beta',\varphi)\big) \qquad \text{(F1)}$$

Of these effects, the integral of Snell's law (expressed by the *θ'* factor), geometric considerations (the cosine applied to Snell's law), and Fresnel's law (R_o) are all constants.

The value of z_{diff} was determined by numerically integrating the path length equation (as determined in Section 4.3) for every point in the sky. The obtained value was approximately $2R_c$. Combining joining all the integrals into one constant ζ and assuming this constant for the value of z_{diff} gives:

$$I_{diff_C} = \zeta exp(-\alpha X \cdot 2R_c) I_{diff} \qquad \text{(F2)}$$